Optical sensors and their applications for probing biological systems

Palanco, Marta Espina; Kneipp, Katrin; Berg-Sørensen, Kirstine; Hélix-Nielsen, Claus

Publication date:
2016

Document Version
Publisher's PDF, also known as Version of record

DTU Physics
Department of Physics

Optical sensors and their applications for probing biological systems

Marta Espina Palanco

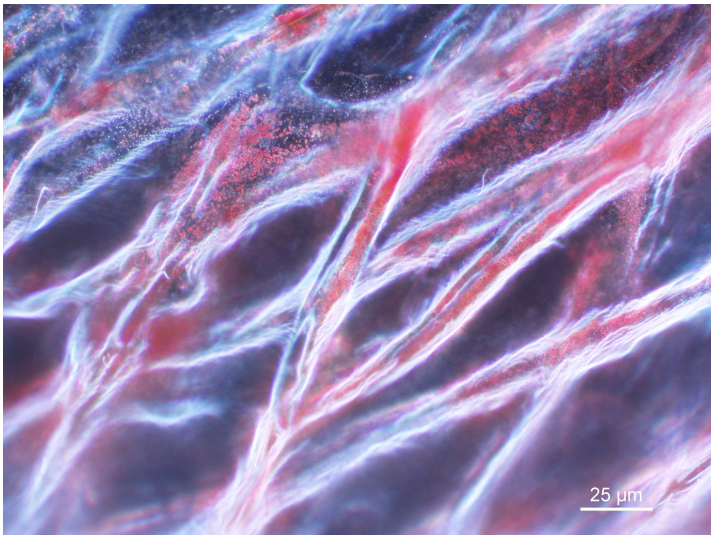

PhD thesis
1 August 2016

Advised by Professor Katrin Kneipp and Associate Professor Kirstine Berg-Sørensen

Cover illustration: Dark field image of silver ions in the extracellular space of an Onion. Image taken by Klaus Bo Mogensen and reproduced from ref[63].

Optical pH sensors and its applications for probing biological targets

Typeset using LaTeX}

http://www.fysik.dtu.dk/microfluidics

Abstract

There is a great interest in exploring and developing new optical sensitive methodologies for probing complex biological systems. In this project we developed non-invasive and sensitive biosensor strategies for studying physiologically relevant chemical and physical properties of plant and mammalian cells. First, we performed Surface Enhanced Raman Spectroscopy (SERS) studies on intact plant materials via using silver plasmonic nanostructures. Our studies showed strong Raman signals which resemble to the presence of typical constituents such as carbohydrates, proteins and lipids of different parts of the fresh tissues. The location of the nanoparticles inside some of the tissues was examined via SERS images, collected from Raman signatures of the constituents of the tissues as well as from Raman signatures of a specific pH-sensitive reporter molecule attached to the nanoparticles. The reporter molecule provided pH values of the extracellular space of the *in-situ* plant material.

The performance of SERS in intact plant tissues included the exploration of different strategies for synthesizing and delivering plasmonic nanostructures into plant tissues via green synthesis of silver nanoparticles with specific plants such as onions and fruit extracts. The formation of spherical and sharp-edged shape silver nanoparticles of around 10 to 300 nm showed the possibility of controlling the morphology of synthesized silver nanoparticles as a function of the plant extract used. Alternatively, the delivery of nanoparticles into the extracellular space of an intact plant tissue was carried out by the incubation of silver salts into the sample. Our results showed the formation of plasmonic nanostructures located at the extracellular space of the sample. This work showed the capability of an intact biological sample to provide a SERS-template where silver nanoparticles can grow, thus providing a new insight into SERS-based sensors for chemically sensing *in-situ* plant constituents.

Optical manipulation techniques have been used to investigate mechanical properties of soft membrane cells, i.e. mammalian cells, proteins and their interactions within a specific cell environment. Curvature and mechanical forces in the membrane play an important role in the activity of the membrane-bound protein. The overall motivation of the second

part of the PhD project was to explore the dependence between the membrane curvature and the activity of membrane proteins. We developed an optical trapping device using a micro-fluidic chip with embedded delivery of laser light. The fluidic system consisted of three inlets joining to form a main channel that led to a single outlet. Cell samples were injected in the central inlet whereas side-inlets were used for hydrodynamic focusing in a stable-laminar flow in the chip. In the middle of the main channel, two optical fibers were placed opposite to one another and perpendicular to the axis of the main channel. Thus when a cell passes through the two opposing optical lasers, it can be trapped and deformed via variations of the light intensity through the optical fibers. Of key importance was the ability to create stable laminar flows at low velocity fields. We therefore optimized the presented device to be able to trap a large number of cells and to exchange the local environment of a trapped cell. The project could provide new insights into the desired biosensor for future membrane-protein cell studies.

Resumé

Der er stor interesse for at undersøge og udvikle nye optisk sensitive metoder til at måle på komplekse, biologiske systemer. I dette Ph.D. projekt er udviklet ikke-invasive og følsomme biosensor strategier til studies at fysiologisk relevante kemiske og fysiske egenskaber af planter og af dyreceller. Første del af projektet har omhandlet *Surface Enhanced Raman Spectroscopy* (SERS) studier af intakt materiale fra planter vha. plasmoniske nanostrukturer i sølv. Vore studier har vist stærke Raman signaler svarende til tilstedeværelsen af typiske bestanddele så som kulhydrater, proteiner og lipider, der stammer fra forskellige dele af friskt plantemateriale. Placering af nanopartikler i materialet blev studeret vha. SERS billeder, opnået dels fra Raman signaturen fra ovennævnte typiske bestanddele, dels fra Raman signaturen fra et pH-følsomt reporter-molekyle fastgjort til nanopartiklerne. Måling på reporter-molekylet tillader bestemmelse af pH værdien af ekstra-cellulære områder i in situ plantemateriale.

I forbindelse med SERS målingerne i intakt plantemateriale har projektet undersøgt forskellige strategier for syntese og indførsel af plasmoniske nanostrukturer i det intakte plantemateriale, herunder såkaldt *grøn* syntese af nanopartikler i sølv i løgplanter og med ekstrakt fra frugter. Dannelsen af sølvpartikler i forskellige faconer, og med størrelse i intervallet mellem 10 og 300 nm, har vist muligheden for at kontrollere sølv-nanopartiklens form via valg af planteekstrakt. Som en alternativ strategi er indførsel af nanopartikler i ekstra-cellulære områder af intakt plantemateriale udført ved inkubation med sølv-holdige salte. Vore resultater viser dannelsen af plasmoniske nanostrukturer i ekstra-cellulære områder af prøven. Hermed er demonstreret at en biologisk prøve kan anvendes som grobund for sølv-nanopartikler til SERS forsøg, hvormed typiske kemiske bestanddele kan detekteres in situ i en plante.

I anden afdeling af projektet er optisk manipulation blevet anvendt til studier af mekaniske egenskaber af celler med blød overflade, dvs. dyreceller, med det formål at kunne nå til en eksperimentel metode til undersøgelse af afhængigheden af membran kurvatur og aktiviteten af et membran-bundet protein. Krumning og mekaniske kræfter i membranen

spiller en vigtig rolle i membran-bundne proteiners virkemåde. Undervejs i projektet er udviklet et optisk fælde system i en mikrofluid chip med indbyggede optiske fibre. Væskesystemet er opbygget med tre indgangskanaler, der samles til en enkelt hoved-kanal. En celle-opløsning blev tilført den midterste indgangskanal mens de to side-kanaler tillader hydrodynamisk fokusering ved en stabil laminar strømning. Vinkelret på hovedkanalen er to optiske fibre placeret modsat hinanden, hvorved to modsat-rettede laserstråler kan sendes ind i væskestrømmen i hovedkanalen. Når en celle passerer de to laserstråler kan den blive fanget og deformeret, kontrolleret af variation i lysintensiteten i de to laserstråler. Stabile laminare strømninger ved lav væskestrømningshastighed er søgt opnået, idet projektet har søgt at optimere en eksperimentel forsøgsprotokol i den mikrofluide chip med optisk tostråle-fælde på en måde, der muliggør måling på mange individuelle celler, og en protokol der muliggør udskiftning af den omgivende væske for en enkelt celle i den optiske fælde. Denne del af projektet kan bidrage til fremtidige undersøgelser af membran-proteiners funktion.

Preface

This dissertation is submitted in partial fulfillment of the requirement for the PhD degree in Physics, at the Technical University of Denmark (DTU). The PhD project was carried out at the Department of Physics from August 2013 to August 2016, within the Cellular Biophysics Group in Fluids section. In the period from August 2013 to February 2015, the project was supervised by Prof. Katrin Kneipp (main supervisor) and Senior Scientist Klaus Bo Mogensen, from February 2015 to April 2015, by Prof. Henrik Bruus (main supervisor) and Senior Scientist Klaus Bo Mogensen and from April 2015 to August 2016, by Assoc. Prof. Kirstine Berg-Sørensen (main supervisor) and Assoc. Prof. Claus Hélix-Nielsen.

I would like to thank the people that accompanied me and supported me during this three years project. First, all my supervisors who made possible this PhD. Specially Katrin Kneipp and Kirstine Berg-Sørensen, who guided me in this period and dedicated intensive time for multiple inspiring discussions. Their committed dedication and constancy pushing and motivating make me enormously grateful. Also, I would like to thank to my co-supervisors, especially Claus Hélix-Nielsen, who always was very supportive in times of losing supervisors.

My strong appreciation also goes to the microfluidic group at Physics Department, for their great support and specially for making me feel welcome in their groups in the two occasions where I had to change the project, organizing multiple brain-storming meetings.

I also owe many thanks to Temo for carefully reading drafts of this thesis, giving valuable feedback and to Sankhya, Julia and Mariona for helping at editing some parts of the thesis.

Last but not least, I would like also to thank my good friends from DTU dancing, their positivism and good sense of humor kept reminding me that giving up was never an option, and my family and close friends for the encouragement and support offered in all my decisions.

Contents

List of Figures

List of Abbreviations

SERS	Surface Enhanced Raman Spectroscopy
NPs	Nanoparticles
pH	Hydrogen ion activity
nm	Nanometer
pMBA	4-Mercaptobenzoic acid
IR	Infrared
cm	Centimeter
BPF	Band pass filter
DM	Dichroic mirror
CCD	Charge-coupled device
UV	Ultraviolet
NIR	Near infrared
Ag	Silver
Au	Gold
SPR	Surface plasmon resonance
bR	Bacteriorhodopsin

List of Symbols

E_n	Electronic energy levels
V_i	Vibrational energy levels
E	Energy
F	Force
I	Intensity
P	Power
k	Spring constant
x	Displacement
m	Mass
h	Plank constant
ν_0	Frequency of light
ν_M	Molecular frequency
v_0	Velocity
c	Speed of light
w	Reciprocal frequency
n	Refractive index
μ	Dipole momentum
α	Polarizability
ϵ	Electrical field
ε	Dielectric constant
q	Vibrational coordinate
q_0	Coordinate amplitude
P_{Stokes}	Stokes Power signals
$P_{Anti-Stokes}$	Anti-Stokes Power signals
E_{Stokes}	Stokes Energy
$E_{Anti-Stokes}$	Anti-Stokes Energy
r	Position
$r_{equilibrium}$	Position at the equilibrium
w_M	Molecular reciprocal frequency
t	Time
N	Number of molecules

σ	Cross section
λ	Wavelength
$Re(\varepsilon)$	Real part of electric permittivity
$Im(\varepsilon)$	Imaginary part of electric permittivity
R	Reflection coefficient
K	Boltzmann constant

Chapter 1

Introduction

1.1 Motivation

In order to describe the biological motivation of this PhD thesis it is necessary to look back 351 years, when the smallest unit of life, a cell, was discovered[1]. Following this discovery, the understanding of the microscopic world became a very interesting field of research and continued growing with the discovery of the first living cells in water[2]. Mathias Jackob Scheleiden suggested for the first time that all plant tissues are composed of cells. Nowadays, it is known that plant cells are composed of a cell wall, a cytoplasmic space and a nucleus each containing several important molecules with a fundamental role in keeping the cell alive. On one hand, primary metabolites such as carbohydrates, lipids and proteins form the major part of the cell and are indispensable for the existence of all plants playing an important role in the growth, development and reproduction of plants. On the other hand, secondary metabolites appear in plants at much lower concentrations, are responsible for the individual characteristics of each species and their role is related with the protection of plants[3].

Plants are one of the most important natural resources in earth, having an essential role for all living beings. Due to their enormous value in many fields, e.g. in ecology, economy and medicine, the study of the properties and functionality of plants has gained great interest with aim of optimizing their use. Very common techniques used to investigate the chemical composition of plants are based on biochemical and biophysical methods, e.g. chromatography[4,5]. Although these techniques are very accurate, they involve destructive analysis of the plant specimen[6]. More recently, optical techniques, such as spectroscopy and imaging techniques, have been used as a non-destructive alternative for studying biological systems as reviewed recently in[7–9]. In particular, Raman techniques have shown its potential for sensing intact plant tissues, thus providing information about chemical constituents as well as their location within the tissues (described further in Chapter 4)

as reviewed in e.g.[10]. However, the presence of auto-fluorescence molecules, typically located in plants, often generates a background in the spectra that can overlap Raman signals thereby limiting its applicability for studying biological material. In this context, surface enhanced Raman scattering (SERS) is a potential alternative to overcome the low signal limitations, in some cases enhancing Raman signals up to 14 orders of magnitude[11]. Nevertheless, the implementation of SERS involves the usage of metallic nanoparticles whose toxicity effects have not yet been studied extensively[12,13]. Some of the toxic effects of silver or gold nanoparticles in living organisms that have previously been shown are related with cellular damage due to an oxidative stress on cells as reviewed recently[13]. However, *in-vitro* studies of the toxicity of silver nanoparticles in rats have shown non inexorable effects after exposure of the nanoparticles[14–16] as well as no carcinogenic or toxic effects to the immune, cardiovascular, nervous and reproductive systems[17]. It is important to consider that the main determinants for toxicity are size, morphology, surface area and exposure time (dosage) and that the effects mentioned typically only arise at high dosage[13].

The functionality of a plant, and in general of any living being, depends not only on its molecular constituents and their location in the cells but also on their interaction, for example membrane-protein mechanical interactions resulting in triggering of intracellular signaling pathways by the selective transport of molecules through the protein[18]. It has been shown that the insertion and binding of proteins into membranes can be strongly influenced by the membrane curvature, which in some cases can affect the protein activity[147]. For example, it has been observed that the mechanical distortion of a specific protein called Bacteriorhodopsin (bR), embedded in lipid membrane occurs due to the alteration of the curvature of the membrane[19]. The distortion of bR was shown to be related with the elasticity of the connected loops between the helices. In a similar way, it has been demonstrated that the activity of another membrane-protein, Aquaporin in yeast cells, is strongly dependent on the topology of the protein[20].

Several methodologies based on spectroscopy, laser technology and plasmonic techniques are being used to investigate membrane protein interactions as reviewed recently[21]. In particular, the performance of Raman spectroscopy for carrying out biophysics studies had shown certain limitations related with time and spatial resolutions[22]. The typical information that Raman spectroscopy provides from a surface of a sample covers a few micrometers, which typically contain thousands of molecules. The capability of SERS to enhance local optical fields might overcome this problem, allowing to study chemical changes in cells in 1 second collection time. For example, SERS has been shown to be a good alternative for monitoring transport of molecules through a membrane cell[23], as well as for performing biophysical and biochemical studies on cells, such as, detection and

identification of neurotransmitters, microorganism and as a read out method for labeling among others[22]. Also, the capability of SERS to for example, chemically characterize bilayers-membrane structure via suspending gold nanorode in the lipid vesicle solutions have been shown[24] as well as to estimate physical parameters such as pH values, in the system[25]. However, the SERS technique still presents certain limitations related with the fact that target molecules need to be attached to the SERS substrates, i.e. silver or gold nanoparticles.

As an alternative to study cell membrane interactions, the immobilization of a single cell might be desirable in order to have a wider window of observation and higher sensitivity. Optical manipulation techniques have shown their capability to optically trap biological micro-objects, and also to optically deform the shape of micro-objects, for example with an optical stretcher device[26]. These techniques might offer the possibility to study membrane-protein responses under physical changes on the lipid membrane curvature, e.g. via inducing certain curvature in the membrane. For these studies, soft biological or biomimetic cells are required, e.g. mammalian cells.

Overall, this PhD thesis documents the implementation of different optical based-sensor techniques to investigate artificial and natural cells. On one hand, plant tissues were investigated via Raman spectroscopy and SERS, corresponding to the first part of this PhD project. This part of the project involved a comprehensive characterization of plasmonic structures, the key element for performing SERS. On the other hand, an optical trapping device was optimized for future cell interaction studies. This work, corresponding to the second part of the PhD project, was largely motivated by prior studies involving membrane-protein interactions in biomimetic systems.

1.2 Spectroscopic techniques

Spectroscopic techniques study the interaction of electromagnetic radiation with atoms, molecules or solids. The interaction of light with matter can involve different optical phenomena such as reflection and dispersion, and/or absorption/emission of the incoming electromagnetic waves, where the light is redirected and/or cause transitions between two energy levels of an atom/molecule respectively[27]. Depending on the energy of the incoming radiation molecules can undergo different energy transitions, i.e. electronic, vibrational or rotational transitions (Figure 1.1)[27].

Typically, vibrational transitions take place in the infrared region of the electromagnetic spectrum ($10^4 cm^{-1} - 10^2 cm^{-1}$), rotational transitions occur in the radiofrequency ($10^2 cm^{-1} - 1 cm^{-1}$) and microwave regions and electronic transitions in the UV or visible region of the spectrum ($10^6 cm^{-1} - 10^4 cm^{-1}$)[27,28].

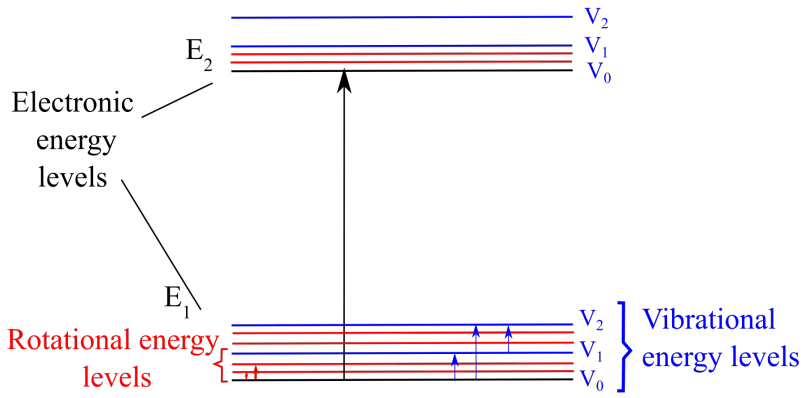

Figure 1.1: Molecular energy transitions. Electronic (black arrows), vibrational (blue arrows) and rotational (red arrows) energy transitions take place within electronic states (E_1 and E_2), within vibrational states (V_0, V_1, V_2) and within rotational states.

As molecules, atoms or ions constantly undergo vibrational, rotational and translational motion, the interaction of light with them can alter these motions, corresponding to the energy of the light. Molecules can manifest changes in vibrational energies due to changes of the positions of the atoms in the molecule with respect to their equilibrium position. Electronic energy changes take place due to a continuous motion of electrons in an atom or bond. In the same way, rotational energies outcome of the rotation of a molecule with respect to its center of gravity. In this way, the change in molecular energy is comprised of the sum of all these possible individual processes:

$$\triangle E = \triangle E_{\text{Electronic}} + \triangle E_{\text{Vibrational}} + \triangle E_{\text{Rotational}} \tag{1.1}$$

with $\triangle E_{Electronic}$, $\triangle E_{Vibrational}$, $\triangle E_{Rotational}$ the energy necessary to undergo an electronic, vibrational and rotational transition respectively.

Molecular vibrations

In order to quantify vibrational energies in a molecule, the system can be simplified to a diatomic molecule composed of two bonded atoms. Thus, the molecular vibration can be modeled as a simple harmonic oscillator, where two atoms are vibrating in the x-direction and the chemical bonds between the atoms work as a spring satisfying Hooke's Law:

$$F(x) = -kx \tag{1.2}$$

where F is the restoring force which is assumed to be along the x-direction, k is the spring

constant and x is the displacement of the two atoms from the equilibrium position, along the x direction. In this way, the two atoms oscillate with a force constant relatively to each other with a frequency ν_M:

$$\nu_M = \frac{1}{2\pi}\sqrt{\frac{k}{m}} \tag{1.3}$$

where m is the reduced mass of the system and ν_M the vibrational frequency of the molecule. With this simple approximation, the vibrational frequency of a molecule can be estimated. For example, considering the stretching vibration of a C-C, C=C and C≡C bond, their typical vibrational frequencies are 450-500 cm^{-1}, 1617-1640 cm^{-1} and 2260-2100 cm^{-1} respectively[29]. As one can see, the stronger is the bond, the higher is the vibrational frequency.

In addition, the energy levels in the modeled harmonic oscillator can be written as:

$$E_n = (n + \frac{1}{2})h\nu \tag{1.4}$$

with n as the quantum number, h as the Plank constant, and ν as the vibrational frequency.

In a harmonic vibrator, the energy levels are equally spaced. Thus, if a photon interacts with a molecule, transition in the energy level of the molecule will only take place when the energy coming from the photon is equal to $\frac{1}{2}h\nu$, $\frac{3}{2}h\nu$ ...etc (equation 1.4). However, a molecule is not a real harmonic oscillator and thus energy levels are not equally spaced[30]. Morse potential is a model that describes the non equally spaced potential energy with other interactions such as effects of bond breaking or anharmonicity of the system. However, for molecules composed of more than two atoms, this approximation may not be applicable. In any case, the behavior of a molecule in the Morse potential can be approximated, inside the potential well, to the behavior of a harmonic oscillator, thus simplifying the problem.

As showed above, molecular vibrations depend on the involved atoms and bond properties. Thus the study of the vibrational frequencies is of high interest. Spectroscopy techniques, such as Raman spectroscopy and/or IR absorption allow to study these chemical and structural properties of individual molecules by identifying the associated unique spectral 'finger prints'. Both techniques are compatible and complementary, implying the possibility of getting the whole vibrational information of a molecule.

1.2.1 Raman spectroscopy

As mentioned earlier, the first part of this project was focused on the performance of Raman spectroscopy. Raman scattering uses scattered light to analyze molecular vibrations in matter, thus obtaining many chemical and structural information of any sample.

Among all the possible phenomena that can occur with light interaction with matter, the dispersion effect is the most common effect used for detection techniques, e.g. Raman spectroscopy. If energy of the incident light is equal to the difference of energy between two allowed energy states of a molecule, photons are absorbed by the molecule. However, the photon-matter collision can also trigger the dispersion of photons independent of their energy. Most of the dispersed photons after interaction have the same frequency as the incident ones. This elastic effect is known as Rayleigh scattering. Moreover, there is always small part of light that is in-elastically scattered (Raman scattering) where energy of the dispersed photons is either higher or lower than the energy of the incident light (Figure 1.2).

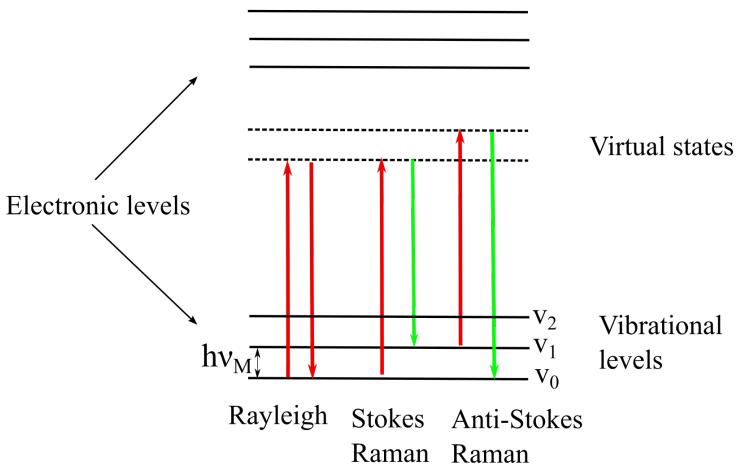

Figure 1.2: Raman effect. Photon-matter collision triggering elastic (red arrows) and inelastic (green arrows) scattering of photons. The excitation of a molecule in its vibrational ground state (Rayleigh and Stokes) or in an excited vibrational state (Anti-Stokes) cause the excitation of the molecule to a virtual state, resulting in the re-emision of photons with equal energy (Rayleigh), lower energy (Stokes) and higher energy (Anti-Stokes) compared with the incident photons.

In an inelastic dispersion, vibrational transitions as well as rotational transitions take place. Considering only vibrational transitions, the interaction of a polarized plane wave of frequency ν_0 with a molecule in an initial vibrational state can cause the transition to an excited vibrational state. If the scattering is inelastic, the frequency of the disperse light will be modified as:

$$\nu_{disperse-light} = \nu_0 \pm \nu_M. \tag{1.5}$$

The Raman effect involves an excitation provoked by the photon as well as remission of the photon from a virtual energy state. This phenomena was discovered by Raman and Mandelstam in 1927[36]. If the excited photons interact with a molecule in its ground state, the energy of the dispersed photons decreases by hν_M, due to the fact that energy is transferred to molecular vibrations (Stokes Raman). Thus, the energy of the dispersed photon is:

$$E_{\text{Stokes}} = h(\nu_0 - \nu_M) \tag{1.6}$$

with ν_0 and ν being the frequency of the incoming and dispersed photons respectively. However, if the excited vibrational energy states of the molecule are over populated, the energy of the dispersed photons increases $h\nu$ (Anti-Stokes Raman),

$$E_{\text{Anti-Stokes}} = h(\nu_0 + \nu_M) \tag{1.7}$$

Classical description of Raman scattering

From the classical point of view, molecular vibrations cause distortion of the electron cloud resulting in small changes in the dipole momentum and in the polarizability of the molecule[37]. Thus, a photon excites the molecule from its basal state to an excited energy state followed by the relaxation of the molecule to a different vibration state upon emitting a photon. The difference of energies between the initial state and the final one, originates a shift in the frequency of the emitted photon with respect to the initial one.

Typically a molecule is Raman active when the molecular vibration changes its polarizability. The interaction of an oscillating electric field with a molecule alters the position of its electron cloud, inducing an electric dipole momentum (μ) in the molecule, which scatters electromagnetic radiation:

$$\mu = \alpha\epsilon = \alpha\epsilon_L cos(\omega_L t) \tag{1.8}$$

where ϵ is the monochromatic electrical plane wave associated with the laser and α is the polarizability tensor. The electric field strength at a given time can be written in terms of a sinusoid function of amplitude ϵ_L and constant frequency ω_L for each component.

The vibrations and rotations in a molecule continuously influence its electronic properties. Thus, α depends strongly on the small displacement of the atoms with respect to the equilibrium ($q = r - r_{equilibrium}$) and on the molecular frequency ω_M. Mathematically, Taylor series expansion can be used to express the polarizability tensor about the equilibrium point:

$$\alpha = \alpha_0 + (\frac{\partial \alpha}{\partial q})_0 q + ... \tag{1.9}$$

with α_0 being the polarizability of the molecule at its equilibrium position and $(\frac{\partial \alpha}{\partial q})_0$ the variation of the polarizability with displacement from the equilibrium position.

Considering that the molecule vibrates with a frequency ω_M, q can be expressed as a harmonic function:

$$q = q_0 cos(\omega_M t) \tag{1.10}$$

with q_0 being the coordinate amplitude, and t the time. Introducing this expression in equation 1.8, it is possible to obtain an expression for μ:

$$\begin{aligned} \mu &= \alpha_0 \epsilon_L cos(\omega_L t) + (\frac{\partial \alpha}{\partial q})_0 q_0 \epsilon_L cos(\omega_L t) cos(\omega_M t) \\ &= \alpha_0 \epsilon_L cos(\omega_L t) + \frac{1}{2}(\frac{\partial \alpha}{\partial q})_0 q_0 \epsilon_L cos((\omega_L + \omega_M)t) \\ &\quad + \frac{1}{2}(\frac{\partial \alpha}{\partial q})_0 q_0 \epsilon_L cos((\omega_L - \omega_M)t) \end{aligned} \tag{1.11}$$

As can be seen in equation 1.11, the dipole momentum of a molecule can oscillate at three different frequencies: at the same frequency of the incident field (Rayleigh (ω_L)), at higher frequencies than the incident field (Stokes ($\omega_L + \omega_M$)) and at lower frequencies than the incident field (Anti-stokes ($\omega_L - \omega_M$)). Notice that the Rayleigh term in the equation is proportional to α_0 while the Stokes and Anti-stokes terms are proportional to $\frac{\partial \alpha}{\partial q}$. In this way, if a molecule is Raman active $\frac{\partial \alpha}{\partial q}$ is different than zero, meaning that the polarizability change with the molecular vibration.

While Raman bands are correlated to changes in polarizability of a molecule, IR absorption is attributed to changes in the dipole momentum of a molecule vibrations. When a molecule is Raman active, asymmetric vibrations with respect to the center of symmetry of a molecule are not allowed. In the same way, molecular vibrations which are symmetric with respect to the center of symmetry of a molecule are forbidden in IR spectrum (see figure 1.3).

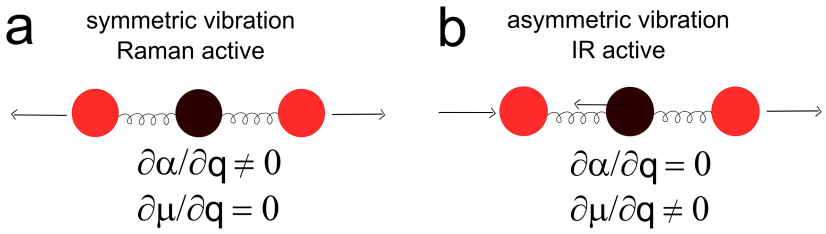

Figure 1.3: Raman and IR active molecules. a) Symmetric vibrations in a triatomic molecule (Raman active) causing changes of the polarizability of the molecule. b) Asymmetrical vibrations in a triatomic molecules (IR active) causing changes of the dipole momentum.

As mentioned, Raman effect requires a change in the molecular polarization potential with respect to the vibrational state. The variation of the magnitude of the polarization between the initial state and the final one determinate the intensity of the Raman dispersion. Taking into account that the emitted electrical field of a dipole momentum is proportional to $\frac{\partial^2 \mu}{\partial t^2}$

$$I \approx \epsilon^2 \approx \frac{\partial^2 \mu}{\partial t^2} \tag{1.12}$$

and also that the intensity of light that a dipole emits is proportional to the square of the electrical field radiated ϵ^2, the scattering power of Stokes and Anti-stokes can be written as:

$$\begin{aligned} P_{Stokes} &\approx (\omega_L - \omega_M)^4 (\frac{\partial \alpha}{\partial q})^2 I_0(\omega_L) \\ P_{AntiStokes} &\approx (\omega_L + \omega_M)^4 (\frac{\partial \alpha}{\partial q})^2 I_0(\omega_L) \exp(\frac{-h\nu_M}{KT}) \end{aligned} \tag{1.13}$$

where both Stokes and Anti-Stokes power are proportional to the four power of the frequency, to the second power of the variation of the polarizability with respect to the coordinate q and to the intensity of the excitation laser. Notice that the Boltzmann factor in $P_{AntiStokes}$ represent the probability of certain energy level to be occupied. In the case of Anti-Stokes process, the scattering starts from an excited energy level, thus the Boltzmann factor makes the Anti-Stokes power values smaller than the Stokes power.

Quantum description of Raman scattering

From the quantum point of view, Raman scattering results from an electron transition between the ground state to a virtual energy level where the molecule stays for a short period of time, causing the Stokes and Anti-Stokes radiation.

The interaction of light with matter can be considered as the collision of two objects [70]. In this context, an inelastic collision between a photon with frequency ν_L and a molecule of mass M and velocity v_0 results in an exchange of energy between them, providing internal molecular excitation in the molecule (vibrational, rotational or electronic). Thus, taking into account the conservation of energy after collision:

$$h\nu_L + \frac{1}{2}(v_0)^2 + E_1 = h\nu + \frac{1}{2}v^2 + E_2 \tag{1.14}$$

with ν_L being the excitation frequency, v_0 and E_1 being the velocity and energy state of the molecule before interaction respectively. Considering that the velocity of the molecule does not change after the collision, it is possible to write an expression for the frequency of the molecule:

$$\nu_L - \nu = \frac{E_2 - E_1}{h} \tag{1.15}$$

$$\triangle E = E_2 - E_1 = h\nu = hc\omega \tag{1.16}$$

where $E_2 - E_1$ is the energy between two quantized states, h is the Plank's constant, c is the velocity of light, ν is the frequency in hertz and ω is the wavenumber measured in cm^{-1} [28].

When photons interact with a molecule, the distribution of electrons in the molecule is altered and thus both, electrons from the lower and higher vibrational energy levels can be excited. As mentioned, in Stokes, photons interact with a molecule in its lower vibrational energy (V_0) and the electrons are excited to a virtual state (Figure 1.2). The energy of the virtual state is higher than the ground state, but not necessary equal to any electronic level thus, the molecule stays in its ground electronic level. However, part of the excited energy of the photons can be transmitted to vibrational energy levels of the molecule. Therefore, when the molecule release energy from the virtual state, the molecule ends in a higher vibrational energy state, emitting photons with lower frequency compared with the initial ones. Similarly, in Anti-stokes, photons interact with a molecule in an excited vibrational state producing the relaxation of the molecule to a lower vibrational energetic level. As a result, the molecule scatters photons with higher frequency compared to the initial ones.

Following Maxwell-Boltzmann distribution, in thermal equilibrium most of the molecules are in their lower vibrational energy levels. Thus, the population of the ground vibrational state (Stokes) is higher compared with a molecule in an excited state (Anti-Stokes), thus

Stokes signals are often higher than Anti-Stokes. The relative intensity between Stokes and Anti-Stokes signals in a Raman spectrum can thus provide information about the temperature of the molecules[71]

$$\frac{I_{Stokes}}{I_{Anti-Stokes}} \propto \exp(\frac{h\nu}{KT}) \tag{1.17}$$

with $h\nu$ being the transition energy, K the Boltzmann constant and T the absolute temperature.

In Raman scattering, not only is the electron cloud distorted but also a nuclear movement (change in the polarizability of the molecule) occurs. In fact, Rayleigh dispersion is a dominant effect while Raman dispersion only involves one photon in each 10^6-10^8 photons. Often in Raman spectroscopy, the intensity can be quantified in terms of the cross section and the intensity and the power of the laser:

$$P(\nu) = N\sigma I_0(\nu_L) \tag{1.18}$$

with N being the number of molecule in the probed volume, σ the Raman cross section and $I_0(\nu_L)$ the excitation laser intensity. Notice that, comparing equation 1.18 with equation 1.13, Raman cross section depends on the polarizability of the molecule $(\frac{\partial\alpha}{\partial q})^2$, which must be non-zero to be Raman active.

As mentioned in the biological motivation (Chapter 1), one of the main goals of this PhD project is to perform Raman spectroscopy in plants. Raman scattering exhibits small scattering cross sections of around $10^{-29}cm^2$ per molecule compared for example, with the cross section of fluorescence backgrounds of around $10^{-17}cm^2$ per molecule[11]. The problem is specially seen in biological tissues which are naturally fluorescent. Since Raman signals are significantly small compared with fluorescence signals, the intensity of Raman signals can be restricted by fluorescence backgrounds very easily. One way to avoid this resolution limitations is to perform SERS.

1.2.2 Surface Enhanced Raman Spectroscopy (SERS)

SERS is a surface optical technique that consists of using metal nanoparticles to enhance the Raman signal intensities, making metal nanoparticles the key element of this optical technique. Already in 1974, Fleischman at al. measured the spectrum of a molecule called Piridin, adsorbed to a silver rough electrode, observing very high Raman intensity signals[72]. Such phenomenon was named as Surface Enhanced Raman Spectroscopy (SERS). After some years, Creightom, Blatchford and Albrecht performed again SERS

measurements in the same molecule, Piridin, but in this case in an aqueous solution contained silver and gold colloidal nanoparticles[75]. With these two experimental evidences, the enhanced phenomena was attributed to the presence of the plasmonic metals[73].

The raman molecules used to perform SERS must be attached to the surface of the metal nanoparticles. An external electromagnetic wave (light) is used to simultaneously excite the free electrons of the metal and the Raman samples, thereby, producing the polarization of the medium. In this way, the plasmon resonances in the metal nanoparticle (surface plasmon resonance) are responsible for the enhanced Raman signals[73]. In this section, the surface plasmon resonance effect will be described, followed by a description of the electromagnetic and chemical enhancements that take place during this optical phenomena.

Surface plasmon resonance of metal nanoparticles

Surface plasmon Resonance (SPR) is an optical phenomena that occur when the collective oscillations of the free electrons in a metal nanoparticle are in resonance with the frequency of an external electromagnetic applied field. Typically, silver and gold nanostructures are the most common nanoparticles used to perform SERS because their surface plasmon resonance occurs in the visible frequency range, causing high enhancements in the visible and near infrared frequency range[42].

When the size of the nanoparticle is smaller than the wavelength of the incident light, i.e. a $<< \lambda$, the optical response of a metal nanoparticle depends strongly on the properties of the material such as dielectric constant of the nanoparticle and the medium, and on the geometry of the nanoparticle as reviewed in e.g.[42]. Figure 1.4 represents the interaction of light with a spherical metal nanoparticle of dielectric constant ε_{in}, in a medium with a dielectric constant of ε_0.

Since the particle is very small, it can be assumed that the external field ϵ_0 applied is homogeneous in the particle. Thus, the dielectric function depends on the frequency of the external field. In this way, the polarizability α and the induced dipole momentum μ of the metal nanoparticle can be ascribed as[74]:

$$\begin{aligned} \alpha &= 4\pi a^3 \frac{\varepsilon_{in}(\omega) - \varepsilon_0}{\varepsilon_{in}(\omega) + 2\varepsilon_0} \\ \mu = \alpha\epsilon_0(\omega) &= 4\pi\epsilon_0 a^3 \frac{\varepsilon_{in}(\omega) - \varepsilon_0}{\varepsilon_{in}(\omega) + 2\varepsilon_0} \end{aligned} \tag{1.19}$$

With ε_{in} and ε_0 being the electric permitivity of the metal and of the medium respectively, ϵ_0 the strength of the external electric field and a as the radius of the nanoparticle. More-

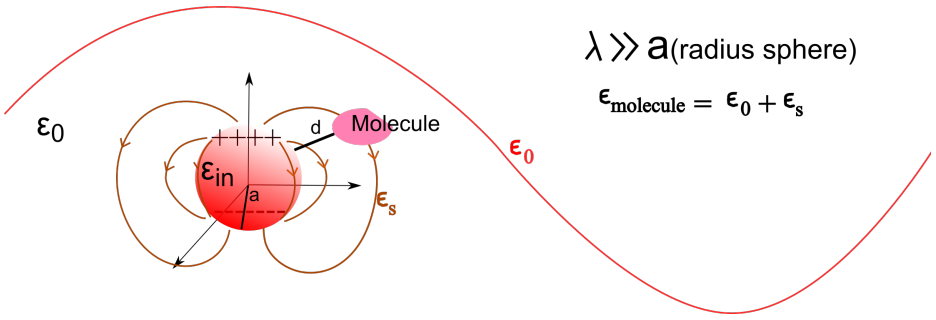

Figure 1.4: Spherical metal nanoparticle (red) of radius a and dielectric constant ε_{in} in a medium of dielectric constant ε_0 where an external electrical field of certain wavelength (λ) propagates, being a $<<$ λ. The electrical field that a molecule (pink), located at a close distance (d) to the surface of a metal nanoparticle, has contributions of both the applied external electrical field (ϵ_0) and the induced electrical field ϵ_s.

over, for particles smaller than 20 nm, the surface plasmon resonance can be quantitatively described by the extinction cross section σ_{ext} as[74]:

$$\sigma_{ext}(\omega) \propto a^3 \lambda \varepsilon_0^{3/2} \frac{Im(\varepsilon_{in})}{[Re(\varepsilon_{in}(\omega)) + 2\varepsilon_0]^2 + Im(\varepsilon_{in}(\omega))^2} \tag{1.20}$$

with λ being the wavelength of the excitation light, $Re(\varepsilon_{in})$ and $Im(\varepsilon_{in})$ as the real and imaginary part of the electric permittivity of the metal nanoparticle respectively. The surface plasmon resonance occurs when the absorption and scattering of the light in the nanoparticle is maximum. Thus, the surface plasmon resonance occurs when $[Re(\varepsilon_{in}(\omega)) + 2\varepsilon_0]^2 + Im(\varepsilon_{in}(\omega))^2$ is minimum (equation 1.20).

In case of metals, with zero or very small $[Im(\varepsilon(w))]$, the condition for surface plasmon resonance would be[42]:

$$Re(\varepsilon_{in}(\omega_{SP})) = -2\varepsilon_0 \tag{1.21}$$

At this frequency (ω_{SP}) the induced dipole momentum and the local electrical field in the proximity of the nanoparticle grows resonantly, reaching intensities much higher than the incident electric field. This resonance implies a strong optical response where the metal nanoparticle absorbs and disperse the light, i.e. plasmon resonance. As mentioned, the optical response of a metal nanoparticle, not only depends on its dielectric constant but also on the geometry itself[42]. Therefore, the resonance conditions given for the equation 1.21 are only satisfied for nanoparticles. However, in all cases, independent of the geometry, the resonance conditions for metal materials are satisfied when the real part of the dielectric constant of the metal is negative $[Re(\varepsilon(w)) < 0]$ and its imaginary part is

zero [$Im(\varepsilon(\omega)) \approx= 0$], implying excellent plasmonic conditions. In this way, the dielectric constant of the medium (which is dependent on the applied electromagnetic field) and the geometry of the particle define the exact resonance conditions. For example, silver and gold nanoparticles exhibit surface plasmon resonances in the visible and violet range while Aluminum nanoparticles typically exhibit surface plasmon resonance at the UV range [43].

An enhancement of a Raman signal takes place due to two major contributions, electromagnetic and chemical enhancements, which are described below.

Electromagnetic enhancement

The electromagnetic enhancement takes place when a metal nanoparticle is illuminated with light that is in resonance with the surface plasmon resonance frequency of the nanoparticle. Thus, this enhancement depends indirectly on the dielectric properties of the nanoparticle, the geometry and size and also on the coupling effect between adjacent nanoparticles hot-spots [45,46]. Enhanced local fields can be quantitatively explained via the simplified Drude model for isolated spheres, where the distribution of charges in a metal nanoparticle can be seen as a sea of electrons moving relative to static positive ions (Figure 1.4) [47]. In this way, an external electric field ϵ_0 interacting with a small particle (a $<< \lambda$), will generate a dipole momentum which itself will induce an electric field surrounding the particle. Therefore, a molecule at a distance d from the surface of the nanoparticle, will be exposed to the resultant electric fields created by both, the external electrical field and the electrical field generated by the nanoparticle due to the surface plasmon (ϵ_s) as reviewed in e.g. [48]:

$$\epsilon_{molecule} = \epsilon_0 + \epsilon_s \tag{1.22}$$

Where ϵ_s can be described in terms of the particle radius (a), the dielectric constant of the metal and of the medium and the distance of the molecule from the surface of the nanoparticle:

$$\epsilon_{molecule} = \epsilon_0 + \epsilon_s = \epsilon_0 + \frac{\varepsilon - \varepsilon_0}{\varepsilon + 2\varepsilon_0} \frac{a^3}{(a+d)^3} \epsilon_0 \tag{1.23}$$

At very close distance to the surface of the nanoparticle $|\epsilon_s| >> |\epsilon_0|$. Thus,

$$\epsilon_{molecule} \approx \epsilon_s = \frac{\varepsilon - \varepsilon_0}{\varepsilon + 2\varepsilon_0} \frac{a^3}{(a+d)^3} \epsilon_0 \tag{1.24}$$

The electromagnetic enhancement factor (A), given by the ratio of the field amplitudes, can then be estimated as:

$$A_{incident}(\nu_L) = \frac{\epsilon_{molecule}}{\epsilon_0} = \frac{\varepsilon - \varepsilon_0}{\varepsilon + 2\varepsilon_0} \frac{a^3}{(a+d)^3} \tag{1.25}$$

Subsequent to the interaction of the incident electric field with the molecule, the resultant Raman scattered light is also enhanced by the surface plasmons. The plasmons will first, enhance the incident light before interacting with the sample and then enhance the Raman scattered light. The total local factor enhancement (G) of the detected Raman intensity can be described as:

$$G = \left| \frac{\varepsilon - \varepsilon_0}{\varepsilon + 2\varepsilon_0} \right|^2_{incident} \left| \frac{\varepsilon - \varepsilon_0}{\varepsilon + 2\varepsilon_0} \right|^2_{Scattered} \frac{a^{12}}{(a+d)^{12}} \tag{1.26}$$

As can be seen, SERS electromagnetic enhancement becomes very large ($\epsilon^4_{molecule}$), and the closer the distance, the higher is the enhancement. In this way, the enhanced power of the SERS stokes signal due to the electromagnetic enhancement, can be written as[11]:

$$P^{SERS}(\nu_L) = N\sigma \left|A(\nu_L)\right|^2 \left|A(\nu_s)\right|^2 I(\nu_L) \tag{1.27}$$

With N being the number of molecules involved, σ as the Raman cross section of the adsorbed molecules, $|A(\nu_L)|$ and $|A(\nu_s)|$ as the enhancement factors of the laser and the scattered light respectively and $I(\nu_L)$ the intensity of the excitation laser.

The electromagnetic enhancement is the strongest mechanism that contributes to the Raman enhancement. However, there is also another effect which contributes to the enhancement of the Raman signal intensities, named chemical enhancement.

Chemical enhancement

The chemical enhancement is related with a transfer of charges between the metal nanoparticle and the adsorbed molecule. In this process, an incident photon excites an electron from the metal nanoparticle to an excited state of the adsorbed molecule, causing a negative charge on it. Consequently, the molecule induces a nuclear relaxation where the electron is released back to the metal, leading to the excited vibration of the neutral molecule and emission of a Raman shifted photon[49–51].

1.3 Optical manipulation techniques

From the macroscopic point of view, light interaction with matter can result in changes in the speed and/or direction of the light due to reflection and refraction. Such variations are

attributed to changes in the linear momentum of the photons, resulting in forces acting on the matter, e.g. radiation forces and gradient forces, that allow trapping, stretching and/or guidance of particles[31,32]. This phenomenon was shown for the first time[31], where a micro-sized particle immersed in water was trapped using two opposite equal transverse Gaussian mode beams. Since then, numerous optical manipulation-based devices have been used for studying biological forces as reviewed in e.g.[33,34] (a more detailed summery of the state of art is provided later in the text, in Chapter 6).

The manipulation of biological micro-objects, i.e. cells, via an optical trapping/stretcher device is possible on condition that the refractive index of the object is larger than the refractive index of the medium[34]. Moreover, the direction and magnitude of the applied forces depend on the size of the object with respect to the wavelength of the incident light[32]. Thus, if the size of the particle is much smaller compared with the wavelength, the particle can be approximated to a point dipole and the calculation of the resultant forces can be described via electromagnetism theory. However, in the case that the size of the molecule is comparable with the wavelength, the description of the forces acting on the particle can be explained through ray optics.

In the following section the trapping and stretcher optical mechanism will be described via optical ray physics.

1.3.1 Optical stretching and trapping forces

Let us consider an external electromagnetic wave, i.e. laser light, of wavelength much smaller than the size of the particle, so ray optics can be applied. The momentum of a photon can be described in terms of energy, the refractive index of the medium where the light propagates and the speed of light in the vacuum:

$$p = \frac{E.n_{medium}}{c} \tag{1.28}$$

with p and E being the scalar values of the momentum and energy. The variation of the momentum after any interaction can be described in terms of the incident, reflected and transmitted momentum of the particle:

$$\Delta p = p_i + p_r - p_t \tag{1.29}$$

Assuming a dielectric cube with a refractive index n_2 in a medium of refractive index n_1, with $n_2 > n_1$ and also considering that the light interacts with the cube with normal incidence angle to the surface, most of the light will be transmitted and only a fraction

(R=0.2%) will be reflected, R being the reflection coefficient which describes the amount of momentum transmitted to and reflected from the particle from an incident electromagnetic wave[34]. Thus, when light with momentum p_i is incident on the surface of the cube a small part of the light will be reflected back to the medium 1 (momentum $p_i R$), and the other part of the light will be transmitted to the medium 2 (momentum $p_i(1-R)$) as described in figure 1.5. Moreover, the transmitted beam (momentum p_t) will interact again on the other side of the cube, reflecting again the same fraction of light, R, and transmitting the other part to the medium 1.

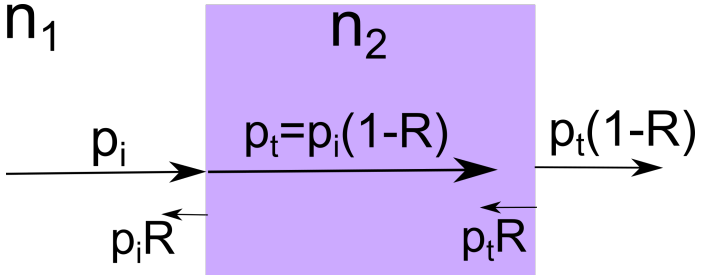

Figure 1.5: Light interacting with a dielectric transparent cube of refractive index n_2 in a medium of refractive index n_1 in terms of the reflection coefficient (R). The interaction of photons with momentum p_i in the cube results in a fraction R of the light reflected back to the medium 1, with the momentum $p_i R$, and in a fraction $(1-R)$ of the light transmitted to the medium 2 with the momentum $p_i(1-R)$. The transmitted beam (p_t) interacts again on the other side of the surface, reflecting again the same fraction of light R ($p_t R$), and transmitting the other part to the medium 1 with the momentum $p_t(1-R)$

As long as $n_2 > n_1$, the cube will gain momentum at the entrance surface. Combining equations 1.28 and 1.29 and writing it in terms of R, the variation of momentum of the light after the interaction with the front surface of the object can be expressed as:

$$\Delta p_{Front} = \frac{E_i n_1}{c} + \frac{E_r n_1}{c} - \frac{E_t n_2}{c} = \frac{E_i n_1}{c} + \frac{R E_i n_1}{c} - \frac{(1-R) E_i n_2}{c} \tag{1.30}$$

In the same way, when the transmitted beam interacts with the other side of the surface, the expression can be written as:

$$\Delta p_{Back} = \frac{E_t n_2}{c} - \frac{E_t (1-R) n_1}{c} + \frac{E_t R n_2}{c} \tag{1.31}$$

The transfer of momentum to the surface of the cube will result in a force acting on the surface of the cube. The same phenomena happens with the interaction of the transmitted beam with the back part of the surface of the cube, leading to two opposite forces that will cause the stretching of the object (see figure 1.6).

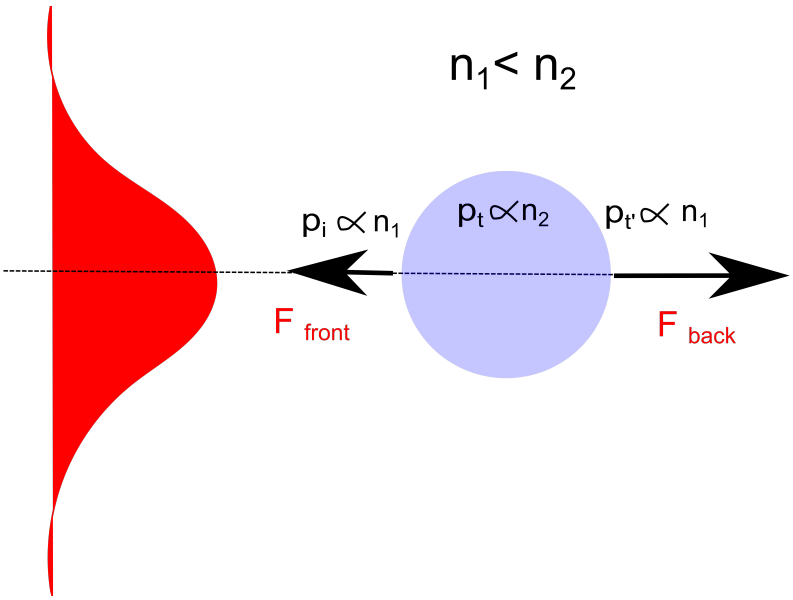

Figure 1.6: Light from a Gaussian laser beam propagating in a medium of refracting index n_1, interacts with a dielectric sphere with a refractive index $n_2 > n_1$ and radius $a >> \lambda$. p_i, p_t and $p_{t'}$ are proportional to the refractive index and represent the momentum of the photons before and after the interaction with the object. The light interacting with the object leads to two forces, F_{front} and F_{back}, acting on the front and back surfaces of the object.

The force acting on the front and back surface of a particle, mainly depend on the refractive index of the medium and power of the laser beam:

$$F_{front} = (n_1 - (1-R)n_2 + Rn_1)\frac{P}{c} \tag{1.32}$$

$$F_{Back} = (n_2 - (1-R)n_1 + Rn_2)(1-R)\frac{P}{c} \tag{1.33}$$

with P being the power of the laser beam. These two opposite forces acting on the surfaces of the dielectric object will result in a stretching force $F_{surface} = (F_{back} + F_{front})/2$. In addition, the sum of these two forces F_{front} and F_{back} acting on the dielectric object results in a net force pushing the particle in the direction of the propagation of the light called scattering force ($F_{net} = F_{back} - F_{front}$) and in a gradient force, a force towards the center of the intensity of the laser beam (see figure 1.7). Notice that for example, for a case where the dielectric object has a refractive index ($n_2 = 1.45$) and it is immersed in water ($n_1 = 1.33$), the scattering force (F_{net}) will be around 20 pN and the surface force $F_{surface}$ will be around 200 pN, i.e. ten times higher[34].

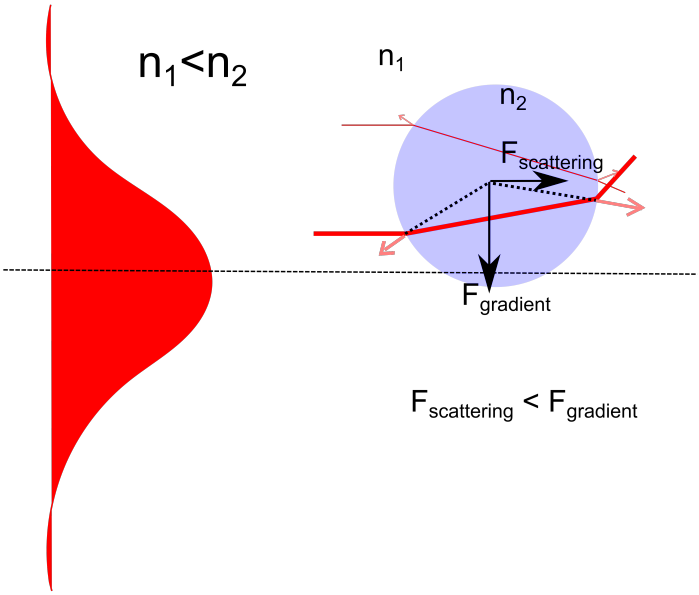

Figure 1.7: Interaction of a Gaussian beam (red region on the left side of the image) with a transparent dielectric sphere (blue circle) results in gradient forces acting on the sphere towards regions of greater light intensity and scattering forces, pushing the sphere in the direction of propagation of light.

When two laser beams are used opposite to each other, the resulting scattering forces will be equilibrated, allowing to trap a particle. Once a particle is trapped, the intensity of the incident beam can be increased or decreased, resulting in changes of the momentum acting on the particle and therefore, allowing to double the stretching forces on the object (figure 1.6).

1.4 Outline of the thesis

The rest of the thesis is organized as follows:

- **Chapter 2: Optical Experimental Techniques**
  The three years PhD project is comprised of two clear lines of inquiry, all based in optical sensors for exploring cells. In this chapter, a description of the experimental techniques, material and methods of two different optical devicesbased sensors, are described. On one hand, an experimental Raman and Surface Enhanced Raman Scattering (SERS) setup is detailed along with its individual components. Also, a brief explanation of the required steps for the acquisition of SERS spectra, including the synthesis and characterization of metallic nanoparticles, is described. On the other hand, an experimental optical trapping setup is detailed and its individual components are specified.

- **Chapter 3: SERS Plasmonic Nanostructures**
  The synthesis and characterization of SERS plasmonic nanostructures were one of the main topics addressed during the first part of the PhD project. In this chapter, three journal articles written during the PhD project show the capability of different plasmon supported spectroscopy materials to enhanced Raman signals using infrared and visible excitation light, along with a description of my contribution to these studies. In the first two of the three journal articles, the formation and characterization of green synthesized silver nanostructures from vegetables, i.e. fruit extracts and Allium Cepa are discussed. In the third paper, Aluminum SERS-substrates show the capability of enhancing Raman signals using near infrared and visible excitation.

- **Chapter 4: Raman and SERS in Plants**
  The application of plasmonic nanosensors in intact plants was a new approach. This chapter is mostly concerned with the application of Raman and Surface Enhanced Raman Spectroscopy to investigate the chemical composition of, and the physical parameters in, fresh plant leaves. A major portion of the performed experiments were not presented in the published paper of Raman spectroscopic probing of plant material using SERS[103], and are instead in this chapter. They were fundamental for disseminating new protocols and generating ideas for the later published experiments based on the performance of SERS in Onions. Therefore, this chapter is based on the design of different protocols to prepare Raman and SERS samples i.e. how to bring silver nanoparticles inside plant tissues as well as how to assign chemical compounds to Raman signatures.

- **Chapter 5: Biomimetic Systems as Sensors**
  The remainder of the second part of the PhD project was largely inspired by the experimental work performed during my MSc thesis work, but collected and concluded during the PhD project and presented in Chapter 5. The chapter is based on exploring biomimetic systems for potential applications to design biosensors, where membrane barrier properties and the function of an embedded integral protein in different synthetic matrices are investigated. In addition, this chapter includes a manuscript gathering all the results, along with a description of my contribution to these studies.

- **Chapter 6: Optical Manipulation**
  Chapter 6 covers the final part of the PhD project. It describes the design and performance of an optofluidic system based-sensor able to trap, hold and stretch micro-objects for studying mechanical properties of mammalian cells.

- **Chapter 7: Concluding Remarks and Perspectives**
  Chapter 7 describes the concluding remarks from the three years project along with some thoughts of future work that could to be done.

1.5 Publications during the project

Papers in peer reviewed journals

1. *Surface enhanced Raman scattering on aluminum using near infrared and visible excitation.*
   Mogensen, Klaus Bo; Gühlke, Marina; Kneipp, Janina; Kadkhodazadeh, Shima; Wagner, Jakob Birkedal; Espina Palanco, Marta; Kneipp, Harald; Kneipp, Katrin.
   In: Chemical Communications **2014**, 50, 3744–3746.

2. *Green preparation and spectroscopic characterization of plasmonic silver nanoparticles using fruits as reducing agents.*
   Hyllested, Jes Ærøe; Espina Palanco, Marta; Hagen, Nicolai; Mogensen, Klaus Bo; Kneipp, Katrin.
   In: Beilstein J. Nanotechnol. **2015**, 6, 293–299.

3. *Raman spectroscopic probing of plant material using SERS.*
   Espina Palanco, Marta; Mogensen, Klaus Bo; Kneipp, Katrin.
   In: J. Raman Spectrosc. **2015**, 47, 156–161.

4. *Green Synthesis of Plasmonic Silver Nano Particles in Onion Layers Suitable for Surface Enhanced Raman and Hyper Raman Scattering.*
   Espina Palanco, Marta; Mogensen, Klaus Bo; Gühlke, Marina; Heiner, Zsuzsanna; Kneipp, Janina; Kneipp, Katrin.
   In: Beilstein J. Nanotechnol **2016**, 7, 834–840.

5. *Modulation of membrane barrier properties in model membranes.*
   Espina Palanco, Marta; Helge Skovgaard, Nils; Sondergaard Hansen, Jesper; Berg-Sørensen, Kirstine; Hélix-Nielsen, Claus.
   Article submitted **2016**.

Papers in peer reviewed conferences

1. *Optical two-beam trap in a polymer microfluidic chip.*
   Espina Palanco, Marta; Catak, Darmin; Marie, Rodolphe; Matteucci, Marco; Bilenberg, Brian; Kristensen, Anders; Berg-Sørensen, Kirstine.
   Article submitted **2016**.

Conference posters

1. *Chemical preparation and spectroscopic characterization of plasmonic silver nanoparticles using fruits as reducing agent*
   Hyllested, J.Æ.; Espina Palanco, Marta; Mogensen, Klaus Bo; Kneipp, Katrin.
   Proceedings of the 24th International Conference on Raman Spectroscopy. Jena **2014**.

2. *SERS sensing of plant materials*
   Espina Palanco, Marta; Mogensen, Klaus Bo; Kneipp, Katrin.
   2nd Optical Nanospectroscopy Conference. Dublin **2015**.

3. *Optical biosensors to explore biological systems*
   Espina Palanco, Marta; Mogensen, Klaus Bo; Kneipp, Katrin; Hélix-Nielsen, Claus; Berg-Sørensen, Kirstine.
   60th Annual meeting Biophysical Society. Los Angeles **2016**.

Co−supervision

1. Preparation of plasmonic nanoparticles by green synthesis and test of their optical properties.
   Jes ærøe Hyllested.
   BSc. thesis, Fysik, DTU, 2014.

2. Preparation and Characterization of Silver and Gold Nano-Structures of Various Sizes and Shapes - the Formation of Aggregates.
   Nicolai Hagen.
   BSc. thesis, Fysik, DTU, 2014.

Chapter 2

Optical experimental techniques

The following chapter describes the experimental techniques, material and methods used during this PhD project, i.e. two different optical devices−based sensors. On one hand, an experimental Raman and Surface Enhanced Raman Scattering (SERS) setup is detailed as well as its individual components. Also, a brief explanation of the required steps for the acquisition of SERS spectra, including the synthesis and characterization of metallic nanoparticles, is described. On the other hand, an experimental optical stretching/trapping setup is detailed and its individual components are specified.

2.1 Experimental Raman scattering

2.1.1 Raman and SERS experimental setup

All Raman spectra presented in this project were measured by using a customized Raman setup. My task was to use the experimental setup to perform Raman and SERS studies on different biological samples, but it did not involve the construction nor maintaining of the setup.

The Raman setup comprised a laser source, optical lenses and mirrors, a Raman sample, a microscope, a monochromator, a Charge Coupled Device (CCD) detector and a customized computer software. The different components are discussed below (Figure 2.1).

- **Laser source**
  The Raman excitation light source was a tunable diode laser driven in continuous wave mode (DL 100−Tunable Diode Laser) with an output power 2 mW−300 mW and wavelength range 370 nm−1770 nm[38]. During this project, all Raman spectra were collected using 2 mW at 785 nm. The laser power and wavelength were chosen taking into account

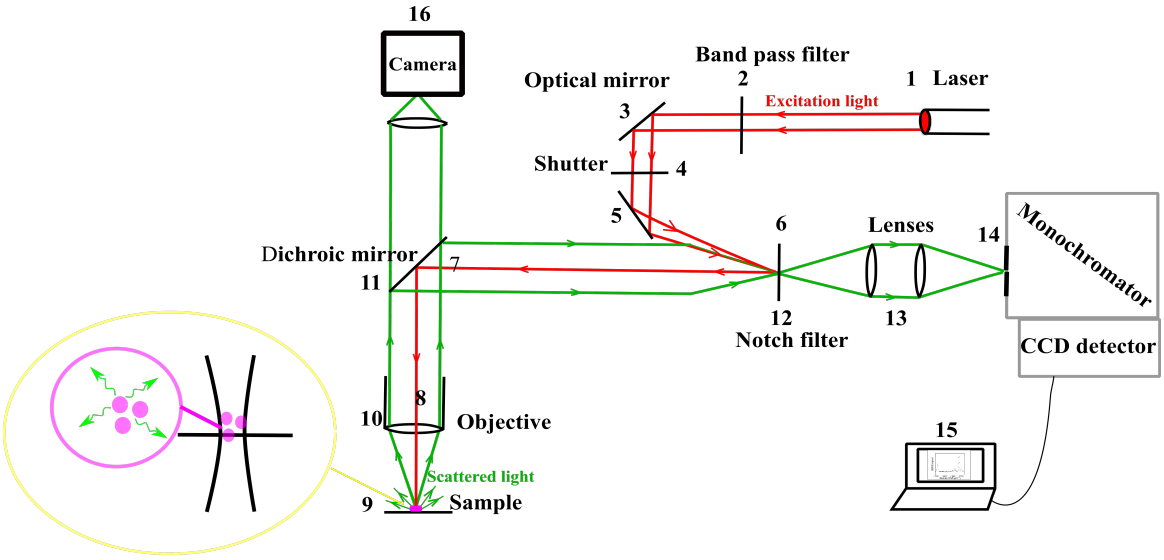

Figure 2.1: Raman setup. The laser beam (1) passes through a band pass filter (2) and is redirected via different optical mirrors (3 and 5) to an optical shutter (4) and to a Notch filter (6), where it is reflected. Finally the beam is redirected via a dichroic mirror (DM, 7) to the objective of an inverted microscope. Raman scattered light triggered after the interaction of the beam with the sample (9), is collected with the same objective (10), reflected in the DM (11) and it passes through the Notch filter (12). Convex lenses (13) focus the beam to a pinhole (14) at the entrance of the monochromator. Once the light reaches the monochromator, a Charge Coupled Device (CCD) converts the optical signal into an electrical signal which is transmitted to a computer (15). In addition, the microscope is equipped with a camera (16).

the Raman samples. Biological samples need to be measured at low power to prevent the sample from degrading. Moreover, the use of near infrared light can avoid strong fluorescent backgrounds in biological samples that can overlap with Raman signals (see sketch of fluorescence and Raman effects in Figure 1.1, Chapter 1).

SERS experiments were also performed with 785 nm wavelength. Therefore, silver nanoparticles used in these experiments were optically tuned in a way that the surface plasmon could be excited at the laser wavelength (explained with more detail in Section *Acquisition of SERS Spectra*, Chapter 2).

- **Optical instruments**
  Several optical lenses were used for focusing the laser beam throughout the whole setup. The laser beam (from step 1) passes through a band pass filter (step 2) in order to clean the laser line and reduce the spectral noise. Afterwards, the beam is redirected via an optical mirror (step 3) to an optical shutter (step 4). The optical shutter blocks the laser beam when is required, e.g. in order to produce a Raman spectrum at a certain exposure time. In step 6, the beam is reflected by a Notch filter and then is redirected via

a dichroic mirror (DM)(step 7) onto the objective of an inverted microscope. The Notch filter cut off a frequency spectra range of $\pm 200 cm^{-1}$ around the frequency of the excited laser beam. Thus, Rayleigh frequencies are prevented from reaching the monochromator and overlapping with signals precedent from the Raman scattering. Raman scattered light triggered after the interaction of the beam with the sample (step 9) is collected by the same objective (step 10), reflected in the DM (step 11) and it passes through the Notch filter (step 12). Convex lenses (step 13) focus the beam to a pinhole (step 14) at the entrance of the monochromator. The pinhole allows only focused light to pass to the monochromator. Once the light reaches the monochromator, a Charge Coupled Device (CCD) converts the optical signal into an electrical signal which is transmitted to a computer (step 15). In addition, the microscope is equipped with a camera (step 16).

- **Raman sample**
  Raman spectra were collected from aqueous solutions and dry state samples. Aqueous samples were studied dropwise in small volumes, with typical drop sizes of $10 - 20\ \mu l$ and at low concentrations. Samples in aqueous solutions were studied with a water immersion objective. The presence of water in the samples does not affect the quality of a Raman spectrum, however, sometimes it can be challenging to measure Raman spectra in solutions due to the difficulty to focus in a specific region. In addition, when using aqueous samples typically the objective was immerse in a sample, therefore, it was very important to maintain the setup clean after each measurement to avoid any chemical contamination.

  Raman samples (both in dry and aqueous state) were deposited onto rectangular transparent hydrolytic class 1 glass (24 mm x 40 mm), with standard thickness of around $0.17 - 0.25$ mm. Figure 2.2 shows an example of one of the Raman samples used during this project.

  The glass slides with the samples were placed on a 3-axis translation mobile stage under the objective. The controlled mobility of the stage allowed to scan samples in the XY plane, over a range of approximately 0.36 mm x 0.27 mm in each scan, controlled by the software.

- **Resolution: microscope, monochromator and CCD**
  The Raman setup was equipped with a custom built microscope which focused the laser beam into the samples and also collected backscattered Raman signals.

  The laser spot−size is related with the wavelength of the laser and the objective[39]:

$$Laserspot = \frac{1.22\lambda}{NA} \tag{2.1}$$

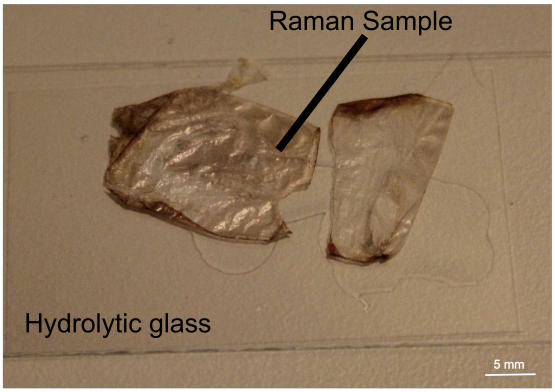

Figure 2.2: Raman sample. Onion cell layers (Raman sample) on a hydrolytic slide, ready for Raman measurements.

with λ the wavelength of the laser and NA the numerical aperture of the microscope objective. Similarly, the diffraction limited spatial resolution is related with the wavelength of the laser and the objective:

$$Spatial resolution = \frac{0.61\lambda}{NA} \tag{2.2}$$

Thus, the higher the NA of the lens (or lower λ), the higher is the spatial resolution and the smaller laser−spot size. The choice of the different NA must take into account the sensitivity of the sample. For example, a higher NA causes light with high power being focused onto a smaller spot in the sample which could damage biological samples. Therefore, there is a compromise between high resolution and damaging the samples which needs to be balanced when performing measurements.

During this PhD thesis, most of the spectra were collected using a $1.3/63x$ or $0.8/25x$ objective, therefore the spectra had a spatial resolution of around 600 nm and laser focal size was around $1-2$ μm.

Notice that during the experiments, not only scattered Raman signals were collected from a focus plane of the sample but also there was unfocused scattered light which can generate backgrounds and overlap with Raman signals. Thus, a pinhole of a few micrometers (step 14, Figure 2.1) located at the entrance of the monochromator was used to avoid this problem by preventing out-of-focus light from reaching the monochromator. In this way, the spectral resolution depends on the width of the slit. The smaller the pinhole, the higher is the spectral resolution but also the lower the Raman signal. Some samples produce weak scattering and in this case if the slit is too narrow no signal is detected by the spectrometer. Thus, there is a trade-off obtaining a lower intensity for

a higher signal-to-noise ratio of the collected scattered Raman signals.

In addition, the spectral resolution of a Raman spectrum depends on different factors related with the spectrometer focal length, diffraction grating, excitation laser wavelength and the CCD[39]. It is important to have good spectral resolution to better determine spectral features and bands in the Raman spectra. In our experiments, the Raman setup integrated two gratings of 900 and 1200 grooves per mm, allowing to measure Stokes spectral regions from 800 to 1600 cm^{-1} or from 600 to 1800 cm^{-1}, respectively. The dispersed light from the grating was collected into a CCD.

- **Computer: spectral measurements and possible source of noises**
  The computer connected to the setup (step 15, Figure 2.1) contained a customized software which allowed to control several parameters in the setup such as light exposure time, a mobile stage and the shutter.

  Before collecting any spectra and also after the acquisition of them, the setup always needed to be calibrated in order to confirm that all components of the setup were working properly. During this project, toluene in aqueous solution was used as a control sample. Figure 2.3 shows a typical Raman spectrum of toluene measured with the setup. As can be seen, the spectrum shows signatures at around 786 cm^{-1}, 1004 cm^{-1}, 1049 cm^{-1}, 1208 cm^{-1}, 1379 cm^{-1} and 1604 cm^{-1} which is in agreement with the literature[41].

  When measuring Raman spectra, there are very typical sources of noise that can reduce the signal-to-noise ratio of the spectrum. These sources of noise are related with the CCD detector, cosmic rays or fluorescent backgrounds. A good signal-to-noise ratio can be achieved by cooling the CCD, applying longer exposure times or increasing the concentration of the samples among others.

  During this project, the light exposure time for acquiring a spectrum was controlled from the software. All the spectra collected in this thesis were collected with an accumulation time between 1 second and 30 seconds. The reason for using long exposure times are related with the increase of the signal−to−noise ratio and therefore, with the improvement of the Raman signal. However, increasing the exposure time might overheat the samples and therefore, damage them.

  The temperature of the CCD was also indicated in the software. The CCD temperature must be below −100 Celsius degree and an increase in temperature would produce a dominant background in the collected spectrum. Therefore, before starting the collection of any spectra the CCD chip needed to be cooled down with liquid nitrogen.

  As mentioned, the Raman setup requires a shutter to block the light when the CCD is reading out. The shutter was automatically closed after collecting the spectra, however, it could also be controlled from the software.

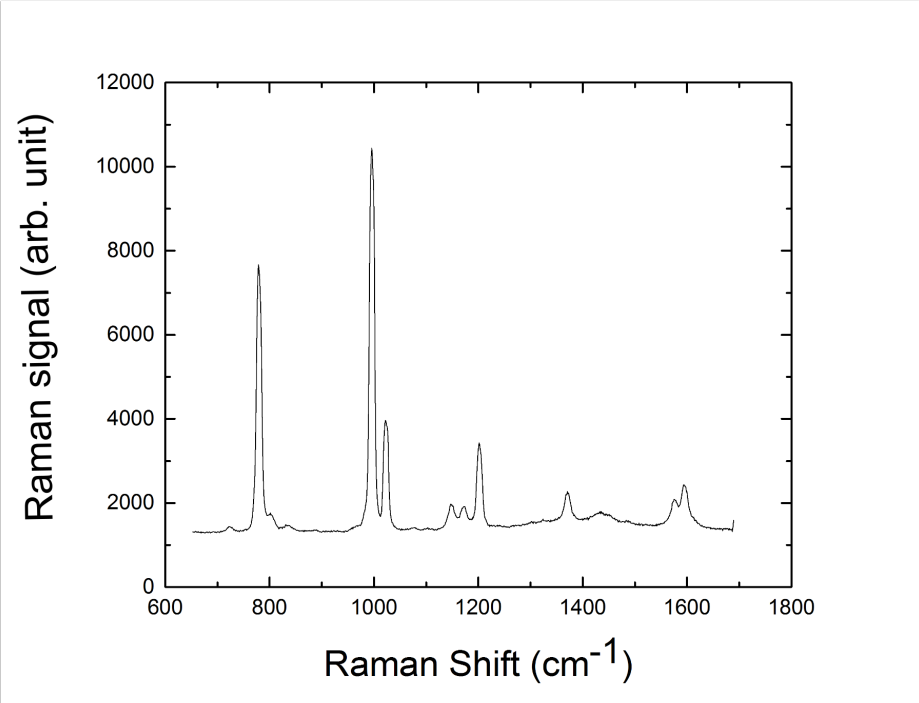

Figure 2.3: Raman Spectrum of Toluene collected in 1 second and excitation light at 2mW and 785nm, CZ63 objective.

All the spectra were collected in a dark room to avoid cosmic spikes over the Raman signals, caused by high energy cosmic rays. The custom-built Raman setup setup was illuminated both from below and from above the sample. This illumination automatically switched off while measuring the Raman spectra. However, it could also be controlled from the software if it is desired.

As mentioned above, all Raman samples were placed on a $3-$axis translation mobile stage also controlled from the software. In this way, Raman imaging based on the spectral output was possible via performing scans all over a sample. For example, Figure 2.4 shows a Raman image and microscope image originated from only one Raman signature. The scan was collected from the surface of an Aloe Vera leaf by using 335 steps, 1 second collection time for each, over an area range of around 0.36 mm x 0.27 mm.

In this particular case, a peak at around 1500 cm^{-1} with a maximum intensity of 159 counts was used to create an intensity color map. The idea to perform this scan was to assign Raman signatures to different parts of the extracellular space of the leaves, thus showing the capability of the Raman technique to study complex biological samples without altering their structure. However, as can be seen in this particular case (Figure 2.4), there is not a clear location at the extracellular space of the leaf where the Raman

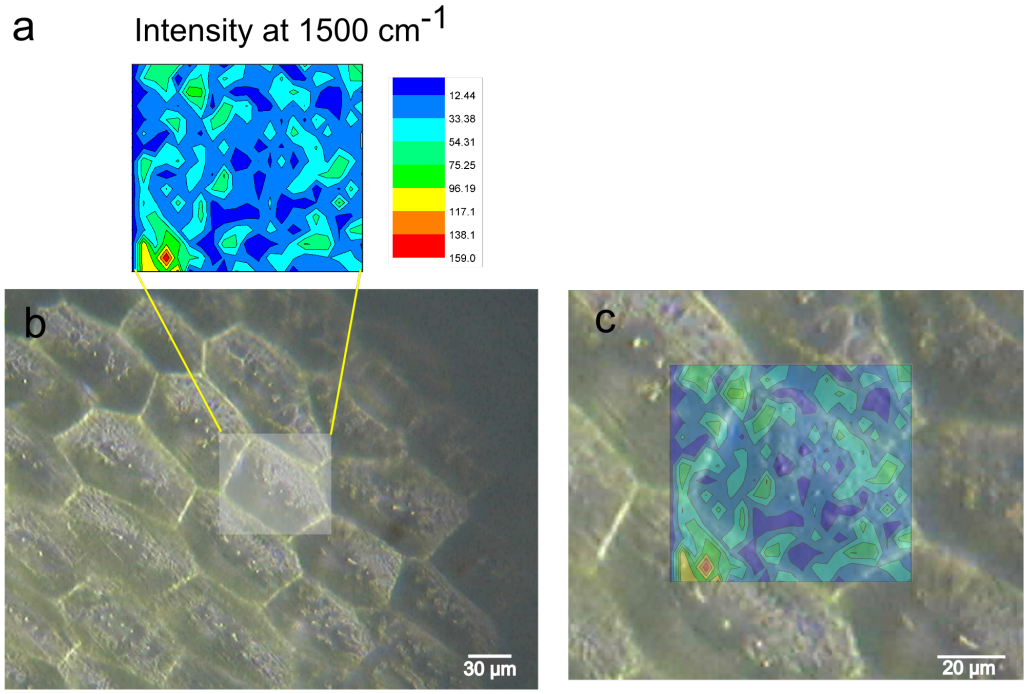

Figure 2.4: (a) Raman image and (b) microscope image originated from the intensity of a Raman signature. Intensity of a Raman signature at 1500 cm^{-1} in a small region (light square located on image b) of the surface of an Aloe Vera leaf, originating a color map (a) with a maximum intensity scale of 159 counts. (c) comparison of the microscope and Raman images.

signature at 1500 cm^{-1} is more dominant. In other words, there is not a clear match between the signal and the different parts of the leaf cell. Furthermore in this particular case, Raman signals are quite low, around 200 counts in average, and probably the contribution of many compounds is not visible in the spectrum. The performance of Raman and SERS in Aloe Vera leaves is described further in Chapter 4.

2.1.2 Acquisition of SERS spectra

As mentioned in Chapter 1, metal nanoparticles are a key element for performing Surface Enhanced Raman Spectroscopy. The synthesis of silver nanoparticles as well as their optical characterization had an important role during this thesis. Furthermore, the development of new protocols for the delivery of such nanostructures into biological samples was one of the main tasks. These points are discussed below very briefly and with more detail in Chapter 3 and 4.

Synthesis and characterization of silver nanoparticles

The SERS experiments performed during this project were carried out with silver nanoparti-

cles. In most of the experiments silver nanoparticles were synthesized by the standard chemical procedure introduced by Lee et al. (protocol described in Appendix A) [58]. Moreover, synthesized silver nanoparticles from plants, i.e. onions, oranges and pineapples, are also presented throughout this thesis (Chapter 3).

As mentioned in Chapter 1, surface plasmon resonance of silver nanoparticles involves a strong extinction of light in the visible range and it depends on anything that could alter the electron charge density at the surface of the nanoparticles, i.e. dielectric constant, size, shape and distance between nanoparticles [42]. The characterization of the nanoparticles were carried out via both, a UV−visible spectrophotometer and a Transmission Electron Microscope (TEM). The UV−visible spectrophotometer allowed to monitor the stability of the nanoparticles via measuring the extinction coefficient while TEM allowed to monitor the morphology and size of the nanoparticles.

- **Ultraviolet-visible spectrophotometer**
  The UV-vis spectrophotometry was situated at the campus of the Technical University of Denmark (DTU), Nanotech department. The spectrophotometer was used as a complementary technique to characterize the synthesized Ag nanoparticles. The ultraviolet-visible spectrophotometer is a device which measures the extinction of light at different wavelengths in aqueous sample solutions. It is composed by a light source, a monochromator, a sample cell with a 1 cm optical path length and a detector that collects the intensity of light transmitted through the sample. In the following experiments the extinction coefficient of light was recorded in the wavelength range between c.a. 350−900 nm. Figure 2.5 shows an example of a typical extinction coefficient spectrum of spherical silver nanoparticles of diameter around 20−80 nm.

  As can be seen in Figure 2.5 a, at very high concentration of silver the absorption band appears saturated, causing a flattening of the absorbance peak. For this reason, as a very first step after synthesizing the nanoparticles, the colloidal solution needed to be diluted to find the optimum concentration of nanoparticles for the detection range in the spectrometer.

  Silver nanoparticles typically show a strong band at around 430 nm (Figure 2.5 a). As mentioned in Chapter 1, the position and width of the peak is specific for each particle and it depends on its dielectric constant. However, in case of spherical nanoparticles, an increase in size causes a slight red shift (towards higher wavelength values) as well as the a broadening of the band (Figure 2.5b) [42].

  To perform SERS it is important to optically tune the sizes and shapes of the nanoparticles in order to be able to excite the surface plasmon with the same laser wavelength as used for performing Raman spectroscopy. For this reason, typically Sodium Chloride

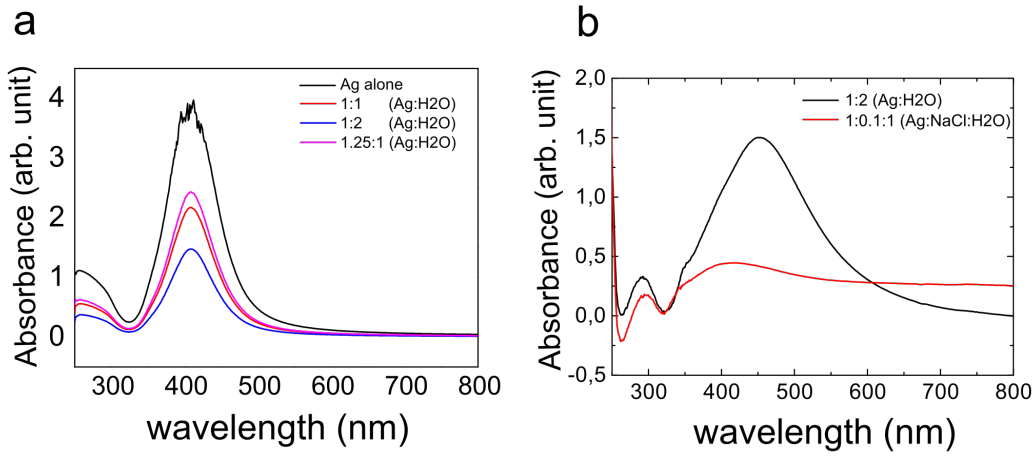

Figure 2.5: Extinction spectrum of synthesized silver nanoparticles via the standard chemical procedure of Lee[58]. a) Surface plasmon resonance wavelength of silver nanoparticles occurs at around 420 nm. b) Addition of NaCl induces a broadening of the peak as well as an increase of the band in the red region, indicating particle aggregation.

(NaCl) is used for inducing particle aggregations. Figure 2.5b shows a particular example where NaCl is added to the colloidal silver nanoparticles. As can be seen, there is a broad peak (a) at around 470 nm suggesting already the existence of bigger nanoparticles. The addition of NaCl (b) trigger in this case a decrease of the intensity of the band around 470 nm and an increase in the red region, leading to increased absorbance at the excitation wavelength range. Moreover, the appearance of a peak at around 300 nm may indicate the presence of silver clusters in the solution, which are the precursors for the growth of the silver nanoparticles (a more detailed discussion is in Chapter 3, article *Green preparation and spectroscopic characterization of plasmonic silver nanoparticles using fruits as reducing agents*).

- **Transmission Electron Microscopy (TEM)**
  The transmission electron microscope is located at the campus of the Technical University of Denmark (DTU), Center of Electron Microscopy. The sample preparation was performed by placing 5 μL of the colloidal nanoparticles on a Lacey carbon film on 300 mesh copper grids ($AGS166-3$, Agar Scientific Axlab, United Kingdom). The spatial resolution of TEM goes down to 1 nm allowing the visualization of nanoparticles with high resolution, and sometimes even lattice ions can be visualized.

  Figure 2.6 shows two images of Ag colloidal nanoparticles synthesized via the reduction of $AgNO_3$ with sodium citrate (Figure 2.6 a) and the reduction of $AgNO_3$ with fruit extracts (Figure 2.6 b), respectively.

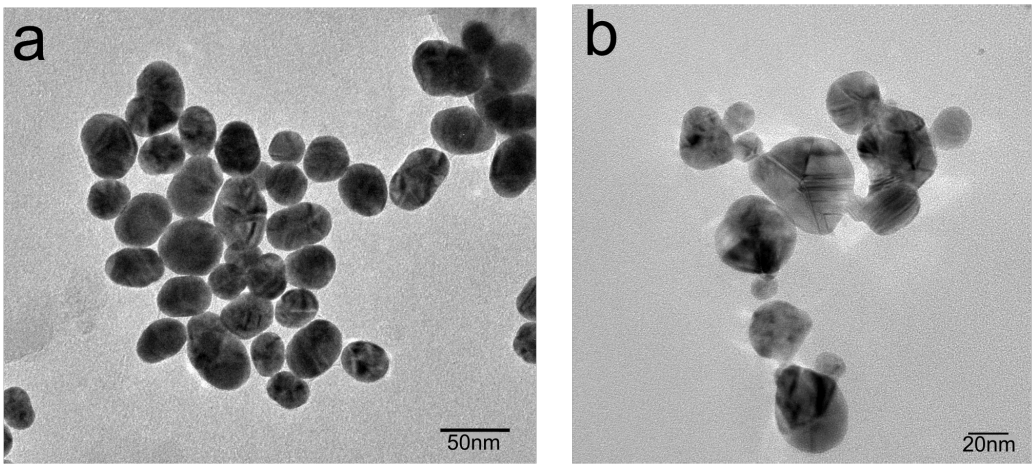

Figure 2.6: TEM images of silver nanoparticles. a) Spherical silver nanoparticles of 20 - 100 nm diameter synthesized via a standard chemical procedure with sodium citrate as a reducing agent. b) Spherical silver nanoparticles of diameter around 10 - 80 nm produced via Green synthesis, i.e. reduction of silver nitrate to silver nanoparticles via fruit extracts as a reducing agent.

As can be seen in Figure 2.6, TEM images identify spherical silver structures between around 10 and 100 nm, consisting of isolated Ag nanoparticles and also small aggregations of particles. Both samples are examples of the nanoparticles synthesized during this project, and they were used as plasmonic building blocks, to enhance Raman signals.

Bringing metal nanoparticles into the Raman samples

One of the main challenges during this project consisted of the development of protocols for the delivery of silver nanoparticles into fresh biological samples without altering their structure, thus allowing to perform SERS. Once the metal nanoparticles were incorporated into the samples all spectra were collected with the same Raman setup described above. The procedure and protocols are described in detail in Chapter 4.

2.1.3 Reagents

The reagents used during the first part of the PhD project were 4-Mercaptobenzoic Acid (pMBA), Silver Nitrate ($AgNO_3$), Gold Chloride Trihydrate ACS Reagent ($HAuCl_4$), Sodium Citrate Tribasic Dihydrate ($C_6H_5Na_3O_7$), Sodium Chloride (NaCl), Tolouene, Lignin Alkali, L−Ascorbic Acid, Adenine and Dopamine were purchased from Sigma−Aldrich Denmark ApS.

All other biological targets used for Raman experiments during this project, such as plant leaves, were collected from natural sources in Denmark. Basil, mint and anise were procured from the plantation of Kaare Hartvig Jensen, Assistant Professor at DTU Physics. Aloe Vera

was procured from the plantation of Henrik Georg Bohr, Professor at DTU Physics. Fresh vegetables such as red onions and celery were bought in the supermarket.

2.2 Experimental optical trapping/stretching

2.2.1 Experimental setup

One of the two goals during the second part of this PhD project was to investigate the capability of an optical trapping device to study the effect of mechanical forces on microscopic objects subject to different environments. All the optical trapping experiments were performed with a customized optical stretcher setup (Figure 2.7) consisting of an optofluidic system providing a stable low−cost instrument able to trap and stretch single microscopic objects. The low cost as well as the mechanical strength of the device makes the production of hundreds of microchips within a few hours feasible, ready to perform optical manipulation experiments.

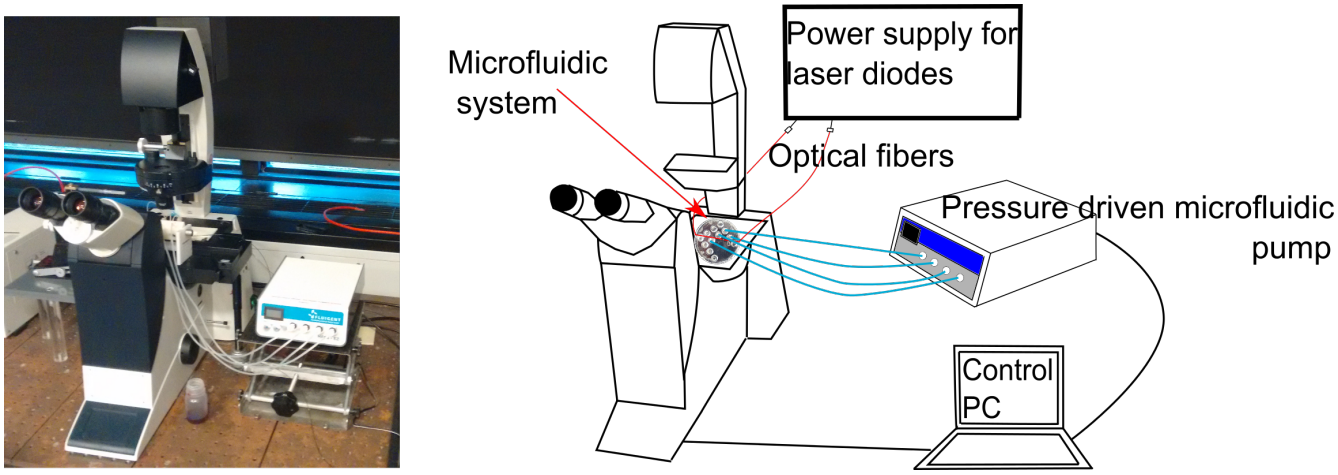

Figure 2.7: Optical trapping setup composed of a microfluidic system, mounted on an inverted microscope and connected to a pressure driven microfluidic pump. Two optical fibers oppositely positioned inside the microfluidic system, are connected to a power supply via standard connectors. The CCD camera of the optical microscope, the pressure driven pump and the power supply are controlled via customized LabVIEW and standard computer software.

The setup was composed of a microfluidic polymer system (Cyclic Olefin Copolymer TOPAS polymer 5013), an inverted optical microscope (Leica DMI3000B) equipped with a CCD camera (Thorlabs DF0420M) and a custom−written LabVIEW software. The microfluidic system had two single−mode fibers (AFM technologies FOP-64-L-5-H64-22) connected to two 1064 nm fiber-couple diode laser (Lumics Lu1064M450-1006N10A). A pressure driven pump (four−channel Fluigent MFCS-EZ, 0-65 mbar) was also connected to the microfluidic system via silicon tubes of 1.5 mm diameter and 50 cm length (VWR ML94231A).

- **Microfluidic system: design and fabrication**
  A key component of the setup was a microfluidic system. The first generation of this device was already reported[69], as well as its functionality and versatility for stretching experiments. In this thesis, a new generation of the device is introduced.

  In all generation−devices, the microfluidic systems were designed and fabricated via injection molding by Darmin Catak (research assistant at DTU), Brian Bilenberg (CTO at NIL Technology), Marco Matteucci (researcher at DTU Nanotech), Professor Anders Kristensen (DTU Nanotech) and associate Professor Kirstine Berg-Sørensen (DTU Physics). The material used to fabricate the microfluidic systems, i.e. CoC polymer, is a transparent material in the visible wavelength range with low water absorption and resistant to different chemicals, e.g. acids and solvents, being very convenient for performing experiments with different solutions in the device[69].

  The microfluidic device was composed of two different parts: the bottom part of the device (lid A) contained the microchannels while the top part (lid B) contained three inlets and one outlet port with the same dimensions as standard Luer fittings (Figure 2.8).

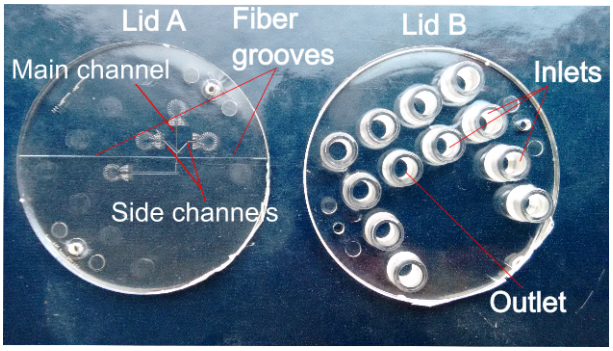

Figure 2.8: Microfluidic device composed of two parts. Lid A contains two side channels that merged together in a main channel, and the fiber grooves. Lid B contains several inlets and outlets Luer fitting ports.

In terms of channel structure, lid A contained three channels, two side channels of cross-section 100 x 100 μm and 3250 μm length each and a central channel of 50 μm depth, 100 μm width and 4350 μm length. The three channels merged together in a main channel of cross-section 100 x 100 μm and 1400 μm length (Figure 2.9). In addition, two fiber grooves of 125 μm width and 135 μm depth were located at around 465 μm behind the merging point of the three channels. The squared geometry and the design of the microchannels together with their sizes were chosen during the design process to optimally balance hydrodynamic resistances through the channels as well as to deliver optical power to the center of the channel[69].

In order to build a trapping/stretching device where particles can be trapped within a few seconds, an important characteristic based on the design of the chip needed to be considered. The microfluidic system was built in a three-layers-technology, such that the different microchannels that form the chip were located at three layers of different depth, ensuring that the microscopic objects that flow through the main channel will reach the focus line of the fiber beams (Figure 2.9). Thus, the central channel was placed on a superior horizontal level with respect to the two side channels, which were on a second lower level and the fiber grooves were placed on the lowest level. The purpose of it was that at the merging point where the three channels join together, the microscopic objects, e.g. cells, will fall down by gravity to the focus line of the two fiber beams, improving their optical capture (Figure 2.9 a) (a further detailed explanation can be found in Chapter 6).

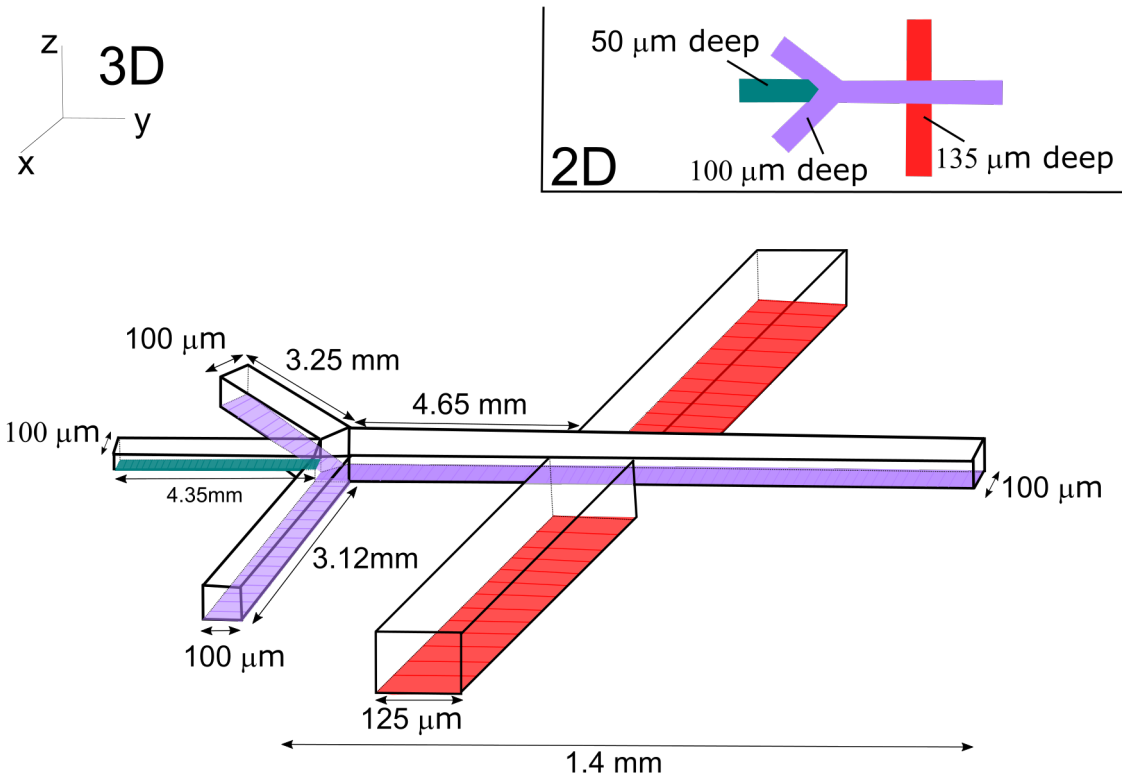

Figure 2.9: Geometry of the microchannels. A central channel situated on a top horizontal level (green), merges with two side channels situated on a lower level (purple). The fiber grooves are placed on the lowest level (red).

- **Optical fibers**

The mentioned design of the microfluidic systems allowed the insertion and alignment of two optical fibers into the systems, with a tip-to-tip distance of around 100 μm. In this way, two single−mode fibers equipped with standard fiber connectors were positioned into the two fiber grooves (Figure 2.8) such that the optical path height is around 30 μm above the main channel (purple level from figure 2.9).

The squared shape of the grooves ensured a better alignment of the fibers via reducing the space surrounding them and therefore, reducing their lateral movement as well as facilitating the fiber bonding. Therefore, the dimensions and the square geometry of the fiber grooves was chosen for an optimal fiber housing.

During the performance of all experiments, the power from each diode laser was kept at 100 mW, reducing the risk of damages in the biological samples due to heating of the sample. Moreover, the wavelength of the two optical beams was adjusted to 1064 nm during all experiments, for the same reason, to avoid damages on the sample. We must note that our experiments are performed in aqueous solutions, thus working in the infrared range could reduce heating of the system due to absorption in water.

- **Mounting fibers and bonding the microchip**
  Two approaches were used for bonding the chip. As a first approach, a transparent microtitreplate tape was used to seal both lids. Further experiments showed that the bonding of the chip was not optimum, causing some technical problems related with leaks of the fluid and/or air between both lids of the chip. Therefore, as a second approach, the two lids were sealed via thermal bonding. In the following section, the bonding procedure via using the transparent tape is described in detail. Moreover, the sealing procedure via thermal bonding is described with more detail in the submitted manuscript, located in Chapter 6 as well as a full protocol of the thermal bonding procedure in Appendix D.

  As mentioned, the microfluidic system was composed by two different parts, lid A and lid B, which needed to be sealed together with the optical fibers in between. Before placing the optical fibers into the fiber grooves (lid A in Figure 2.8), they need to be peeled, cleaved and cleaned to reduce any factor which could scatter the light beam or produce any deviation of the laser beam. Subsequently, the fibers were positioned into the grooves ensuring that both fiber tips were placed at 100 μm distance facing each other. Once the fibers were fitted into the grooves, a small drop of superglue was added on each side of the lid to fix the fibers. At this point, the fibers could easily move due to mechanical traction while the glue was still not dry. For that reason, it was important to check under the microscope that the fibers were correctly positioned during the whole process of bonding.Once the fibers were glued into the grooves, a transparent tape (HJ−Bioanalytik Microtitreplate Technology) was cut in the same shape as the circular lid and positioned very carefully on the top of the lid. This tape is composed

of microdroplets of glue, which when applying a uniform force on the chip, break and expand the glue. The purpose of this tape was to fix the fibers in the grooves and to keep them stable. After adding the tape, the next step consisted of making small holes of around 0.7 mm with a needle (Terumo Neolus, 0.7 x 30 mm), at the position where the inlet and outlet ports will match.

In addition, lid B must be prepared before bonding it to lid A. After cleaning lid B with ethanol, a pressure sensitive tape (Scotch 3M) of thickness around 0.05 mm was added to lid A. The tape needed to be sticky on both sides to be able to glue both parts of the chip, avoiding leaks of air into the channels once the chip was bonded. It was therefore important to use a thick tape to overcome the problem of imperfections regarding the flatness of the surfaces of both lids. Once the tape was placed on lid B, small holes were made at the location of the inlet and outlet ports.

In this first approach, the sealing of the chip was carried out by applying a uniform force generated by a clamp over the surface of the chip. Moreover, during the bonding procedure, the lids were expected to swell into the channels and into the fiber grooves, affecting the alignment of the fibers. However, to prevent that, the chip was designed with grooves of a larger width than the fiber diameter.

The whole process of cleaving the fibers, aligning and gluing them into the chip, and the bounding process took generally around 2 hours.

- **Pressure driven pump**
  The flow through the channel was controlled by a four−channel Fluigent micropump. The pressure pump can hold pressures between 0 to 69 mBar with a pressure sensor resolution of 0.3 and responsive time down to 40 ms (depending on the configuration of the system as well as on the software) while the input pressure was set to 500 mbars.

  The pump was connected to the three inlets and one outlet Luer fitting of the microchip via silicone tubes of diameter 1.5 mm and around 50 cm of length. The length and width of the tubes was chosen to balance hydrodynamic resistances through the tubes. In addition, back flow filters were connected to the pressure pump to avoid the entrance of any liquid into the device.

- **Optical microscope**
  In order to visualize the microscopic particles flowing through the channel, the microfluidic system needed to be positioned under an optical microscope equipped with a CCD camera. Thus, by using different objective magnifications, i.e 63x and 40x, the microscopic objects within the microchannels could be visualized, e.g., trapped particles.

2.2.2 Data acquisition and treatment

A custom written LabVIEW software was used to control different parameters from the setup such as the laser intensity of both optical fibers and the air pressure driven into the microchip. In general, all the experiments were performed via applying small pressures of around 1-2 mbar and a laser intensity of 500 mA.

Images and videos were recorded from the software provided by Leica (Leica Application Suite v3.2.0). In addition, the treatment of images was carried out via ImageJ, e.g. for counting the number of cells inside and outside the focus line between both optical fibers as well as for estimating the flow speed of the particles.

2.2.3 Reagents

Spherical polystyrene microparticles of diameter 5 μm (Fluka, 79633; 10% solid), mixed with water at 1:4 volume ratio, were purchased from Sigma−Aldrich Denmark Aps.

Biological microparticles, e.g. human blood cells and spheroplasts of yeast cells, were prepared via following the protocols detailed in Appendix B and C. Blood cells were obtained from the blood donor center, from the Hospital of Copenhagen, Denmark, while physiological salt water was obtained from Fresenius Kabi AG, Germany.

Chapter 3

SERS plasmonic nanostructures

3.1 Introduction

Metal nanoparticles have gained great attention due to their important role in many fields of science, technology and medicine[42,54,55]. As mentioned earlier in Chapter 1, surface plasmon resonances of gold or silver nanoparticles are very attractive in biology and chemistry for optical sensing and imaging[56]. Moreover, the beneficial usage of these metal nanoparticles have been shown for biomedical applications, e.g. as antimicrobial agents, for diagnostic imaging and for cancer therapeutic techniques as well as for catalysis applications[52,53].

Synthesis of plasmonic nanostructures is necessary and several approaches have been developed for the formation of the nanoparticles[57]. In a *Top to Bottom* approach, nanoparticles are generated from metallic bulk materials by gradual erosion to a specific size and shape for example, via chemical etching or laser ablation. In a *Bottom to top* approach, nanoparticles are built from smaller units such as ions followed by their nucleation, via chemical methods.

Among the chemical processes, the most common procedure to synthesize silver or gold nanoparticles is based on reduction of silver nitrate or chloroauric acid to metal ions by using sodium citrate and sodium borohydride respectively[58]. However, the chemical methods display limitations due to chemical contamination and toxicity during the synthesis procedure. In general, metalic nanoparticles and in particular silver, have limitations associated with their toxicity. The toxicity depends on the size, shape and concentration of the nanoparticles[59].

Instead, an environment friendly approach for the synthesis of metal nanoparticles, known as Green synthesis, has been introduced as reviewed recently[12]. Green synthesis is a simple, rapid, sensitive and inexpensive approach that consists of using biological molecules as a reducing agent. For example, sodium citrate is replaced by biological molecules, i.e. plant extracts, fungus or bacteria, thereby, reducing general toxicity.

Besides silver and gold plasmonics, new extensions of SERS are attractive, e.g. SERS substrates such as Alkali metals that could improve enhanced factors not only in the visible and infrared region of the spectrum but also at shorter wavelengths[60,61]. In particular, the use of Aluminum for the fabrication of SERS substrates have shown to be a good alternative[43,44,62]. The fast oxidation together with the inadequate plasmon wavelength of the metal have not been a problem for creating stable SERS substrates, allowing the enhancement of Raman signals. In this section, we also explored the used of Aluminum SERS-substrates using near infrared and visible excitation light.

In the following sections, 3.2 and 3.3, three journal articles written during the PhD project show the capability of different plasmon supported spectroscopy materials to enhanced Raman signals using infrared and visible excitation light, and are accompanied by a description of my contribution to these studies. In the first two of the three journal articles, the formation and characterization of green synthesized silver nanostructures from plants are discussed. In the third article, Aluminum nanoparticles evaporated in films are probed to work as a supported plasmon materials for SERS.

3.2 Green synthesis of metal nanoparticles

As mentioned earlier, typically the synthesis of silver nanoparticles is carried out by the chemical reduction of silver nitrate with a reducing agent, for example sodium citrate[58]. Thus, in the chemical reaction, silver nitrate gain electrons from the sodium citrate and simultaneously, reduces its oxidation number. This process is followed by the protection of the formed nanoparticles by the capping agent, which is usually also sodium citrate. When the synthesis of metal nanoparticles is carried out via substituting sodium citrate by any biological molecule, the chemical reduction requires the usage of less hazardous substances, thus becoming environmentally friendly[12].

Plant and fruit extracts have shown to be excellent reducing agents in connection with synthesis of nanoparticles for SERS. Typically, compounds with a strong antioxidant activity in plants play a major role in the reduction of silver and gold salts, including saponins, phytosterols, phenolic compounds, quinones, carbohydrates, and protein[64,65]. Moreover, biological molecules also play an important role as capping agents for stabilization of the formed nanoparticles. Once the reduction is completed, the oxidized form of some of the phytochemicals bond with the surface of the particles through Coulomb forces, forming a double layer and controlling the particle size[65]. This prevents the particles from aggregating and therefore stabilizes them. For example, for the specific case of peel extracts as a reducing agent, a total protein concentration in the extract was found to have decreased in the solution that contained nanoparticles, suggesting its possible contribution to the formation of stable

nanoparticles[65]. Also, the capability of oxidized polyphenols to contribute to the stabilization of the formed nanoparticles by capping the surface of the particle has been shown[66].

Not all of the metabolites that contribute in the reduction process contribute as stabilizers. For example, ascorbic acid and pyrogallol have been shown to be excellent reducing agents but their oxidized forms do not contribute to stabilize the nanoparticles or to control their shape[66]. The reason is that once these groups donate an electron in the reaction system, they get transformed to an electrophilic molecule which cannot survive in an aqueous environment and therefore they cannot interact with the surface of the particles[66].

In terms of morphology of the nanoparticles, a strong dependence between the concentration of the plant extract and the size of the formed nanoparticle has been seen[66,67]. If low quantities of the extract are used to reduce, for example, gold ions, the formed nanoparticles will not be protected from agglomerations because of lack of biomolecules to attach to the synthesized nanoparticles. Also, nanoparticles tend to minimize the surface energy forming triangles and pentagons at low concentration of plant extracts[66].

Typically, the reduction of silver and gold ions occur rapidly, i.e. up to 90 percent of the reduction occurs within 8 hours of adding the plant extract to solution of metal ions[66,68]. During this procedure, parameters such as pH, temperature or exposure time must be controlled as they affect the properties of the synthesized nanoparticles[68]. Also, gold ions have a lower tendency to be reduced than the silver ions, due to the difference in the reduction potentials of the two. Thereby the reduction of silver ions is faster than the gold ions[68]. Gold nanoparticles can be cubic, spherical, hexagonal or triangular[65,68]. On the other side, most of the silver nanoparticles tend to be spherical with smooth edges[65].

As mentioned in Chapter 1, the performance of SERS requires the use of nanoparticles which sizes are in resonance with the excitation laser. Most of the synthesized nanoparticles are not in physical contact, but separated by a uniform inter−particle distance[65]. By adding NaCl to the medium, the enzymes and capping agents present in the plants are destroyed, thus destabilizing the nanoparticles and resulting in a decrease of the inter−particle distance via aggregations. High temperature also results in the destruction of the stabilizing proteins and results in aggregations.

One of the main goals of this PhD project was to perform SERS studies in plant tissues. We first looked for a more environmental friendly, simple, fast and low-cost way to deposit these nanoparticles into the plants using natural compounds as reducing agents. For that reason, our first approach consisted of natural synthesis of the metal nanostructures in biological tissue for further experiments, where SERS could be performed directly in the tissue. The following papers,[78,63], presented in section 3.2.1. and 3.2.2., explore the green synthesis of silver nanoparticles using different fruits as well as red onions. These results supported previ-

ous work from literature, where biological molecules were used as template for the formation of silver nanoparticles with a well defined morphology and size.

3.2.1 J. AEre Hyllested, M. Espina Palanco, N. Hagen, K. Bo Mogensen, K. Kneipp. *Beilstein J. Nanotechnol.* 2015, 6, 293–299.

In this section, we explore the formation of silver nanoparticles, of sizes between 10 and 300 nm, as well as the formation of small precursors silver clusters, using pineapples and oranges fruit extracts via varying parameters such as concentration of the extract and light exposure[78]. The formation of different sized and shaped nanoparticles at different inter-particle distance, seems to only depend on the type of extract. The characterization of such nanoparticles was carried out by scanning electron microscopy, transmission electron microscopy and ultraviolet-visible spectrophotometry, together with the spectroscopic techniques luminescence and SERS, proving the formation of silver nanoparticles with different morphologies and sizes.

My contributions to this work was the characterization of the silver nanoparticles through SERS measurements on a target molecule called *para-mercaptobenzoic acid* (pMBA) with NIR excitation light and the Raman setup described in Chapter 2 (Figure 2b from ref[78]). I also characterized the morphology of the nanoparticles by transmission electron microscopy (image from Figure 2a, ref[78]). Also, I conducted a literature study providing the state of art concerning green synthesis of metal nanoparticles from fruit and in general, biological molecules. Finally, I acted as practical co-advisor for the two BSc students co-authoring the paper, namely Jes Ærøe Hyllested and Nicolai Hagen.

beginning of paper

BEILSTEIN JOURNAL OF NANOTECHNOLOGY

Green preparation and spectroscopic characterization of plasmonic silver nanoparticles using fruits as reducing agents

Jes Ærøe Hyllested, Marta Espina Palanco, Nicolai Hagen, Klaus Bo Mogensen and Katrin Kneipp*

Full Research Paper

Open Access

Address:
Danmarks Tekniske Universitet DTU, Department of Physics and Department of Micro- and Nanotechnology, 2800 Kgs. Lyngby, Denmark

Email:
Katrin Kneipp* - katrin.kneipp@fysik.dtu.dk

* Corresponding author

Keywords:
fruits; green synthesis; luminescence; plants; plasmonics; SERS; silver cluster; silver nanoparticles

Beilstein J. Nanotechnol. **2015,** *6,* 293–299.
doi:10.3762/bjnano.6.27

Received: 13 October 2014
Accepted: 05 January 2015
Published: 26 January 2015

Associate Editor: A. J. Meixner

Abstract

Chemicals typically available in plants have the capability to reduce silver and gold salts and to create silver and gold nanoparticles. We report the preparation of silver nanoparticles with sizes between 10 and 300 nm from silver nitrate using fruit extract collected from pineapples and oranges as reducing agents. The evolvement of a characteristic surface plasmon extinction spectrum in the range of 420 nm to 480 nm indicates the formation of silver nanoparticles after mixing silver nitrate solution and fruit extract. Shifts in plasmon peaks over time indicate the growth of nanoparticles. Electron microscopy shows that the shapes of the nanoparticles are different depending on the fruit used for preparation. The green preparation process can result in individual nanoparticles with a very poor tendency to form aggregates with narrow gaps even when aggregation is forced by the addition of NaCl. This explains only modest enhancement factors for near-infrared-excited surface enhanced Raman scattering. In addition to the surface plasmon band, UV–visible absorption spectra show features in the UV range which indicates also the presence of small silver clusters, such as Ag_4^{2+}. The increase of the plasmon absorption correlates with the decrease of absorption band in the UV. This confirms the evolution of silver nanoparticles from silver clusters. The presence of various silver clusters on the surface of the "green" plasmonic silver nanoparticles is also supported by a strong multicolor luminesce signal emitted by the plasmonic particles during 473 nm excitation.

Introduction

Metal nanoparticles in various size ranges play an increasingly important role in many different fields of science, technology and medicine ranging from applications as catalyst, as antibacterial agents in medicine or plasmonic active structures in optical sensing and imaging [1-6]. These broad fields of applications generate a strong interest also in the preparation of metal nanoparticles. Many methods have been invented to synthesize nanoparticles, which can be mainly divided into top down and bottom up processes. Top down processes consist of physical processes where a solid is broken down into nanoparti-

cles as it appears for example during laser ablation of nanoparticles from a macroscopic piece of metal [7,8]. Nanoparticles made by a physical process such as laser ablation have the advantage of being "chemically clean" with no impurities on their surfaces introduced by the chemical preparation process. In the bottom up approach, nanoparticles are created from even smaller structures such as silver ions, which are the outcome of a chemical process. The most popular process among the bottom up methods might be the preparation of silver and gold nanoparticles in aqueous solution by the reduction of silver and gold salts using sodium citrate or sodium borohydride as reducing agent [9]. Recently it has been identified that also plant extracts have the capability to reduce silver and gold salts and to create silver and gold nanoparticles [10-19]. Many different chemical compounds are present in various parts of different plants. Polysaccharides, phenolics, flavoids to mention only a few, could serve as reducing and also stabilizing agents [11]. Overall, using plant materials offers an eco-friendly way to prepare silver- and gold nanoparticles. Moreover, the diversity of chemical composition of plants, i.e., the combination of various reducing and stabilizing agents results in a broad variety of parameters in the chemical preparation process which enables synthesis of many different nanoparticles regarding size and morphology.

Here we study the formation of silver nanoparticles using fruit extracts from oranges and pineapples and check their capability as enhancing plasmonic structures for surface enhanced Raman scattering (SERS). Extracts from these two fruits have been used for preparing silver and gold nanoparticles [12,15-19]. Here we explore the formation of nanoparticles by varying conditions in the preparation process such as ratios of the mixtures of silver nitrate and fruit extracts and the presence or absence of light. Our studies focus on the preparation of nanoparticles between 10 and 100 nm, i.e., a size range which is of particular interest for plasmon-supported spectroscopy, such as SERS.

The formation of silver nanoparticles and their growth is monitored by the increase of the characteristic surface plasmon absorption around 420–470 nm and shifts of the absorption peak, respectively. Absorption signatures in the UV range which can be assigned to small silver clusters and surface enhanced luminescence spectra collected from the particles can provide information on the evolution process of silver nanoparticles.

Results and Discussion

Silver nanoparticles have been prepared at room temperature by mixing silver nitrate solutions and fruit extracts collected from pineapples and oranges. Evolution of the silver nanoparticles starts a few minutes after adding fruit extract to the $AgNO_3$ solution and is indicated by the beginning evolvement of a characteristic surface plasmon extinction band. As Figure 1 shows, for orange extract, the peak of the plasmonic band appears at 420 nm with no shift during the growing process. This indicates that the particles are always within the Rayleigh limit (d << lambda). The increase of the absorption reflects the increasing number of such small silver particles over time. First indication of a plasmon band appears after about 30 minutes. The formation of particles can continue within time spans up to 1 month and longer. No extinction appears in the red and near infrared region.

For pineapple extract, the formation of silver nanoparticles is a faster process. The first sign of a plasmonic band can be seen already after 4 minutes and the process stops after 30 minutes. The peak of the plasmon spectrum appears at 450 nm and shows a small red shift over time. This shift indicates that for pineapple extract, not only the number of particles increases over time, but also the size and morphology of the particles change.

An interesting property of green silver nanoparticles is their capability as enhancing plasmonic structures in SERS, particularly also when excitation in the NIR is used as in many biological applications [20]. High local fields can be generated in small gaps between nanoparticles such as in aggregates [21-23]. The green preparation process using orange extract delivers mainly isolated silver particles and aggregates with relatively wide gaps as it is shown for example in Figure 2a for nanoparticles made from orange extract. Experiments for creating aggregates of green silver nanoparticles with narrow interparticle gaps by adding various molecules, which are known for their capability to foster aggregation of silver nanoparticles [9], such as adenine, guanine, sodium chloride, failed. The extinction spectra in Figure 2a and the SEM image show that also NaCl at relatively high concentration does not force the formation of aggregates with subnanometer gaps as it had been obtained for other silver nanoparticles. The capability of green silver nanoparticles for enhancing Raman signals in SERS was tested by using NIR excitation and the non-resonant target molecule *para*-mercaptobenzoic acid (pMBA). Figure 2b shows a SERS spectrum of pMBA. The enhancement factor was inferred from a comparison with the normal Raman signal of the molecule. Using excitation in the NIR, the green silver nanoparticles provide only modest enhancement factors between 10 and 100 in agreement with computations of field enhancement factors for individual small silver spheres in the near infrared (NIR) [24]. The poor aggregation behavior of the green silver nanoparticles might be explained by the presence of other molecules on the surface of the particles

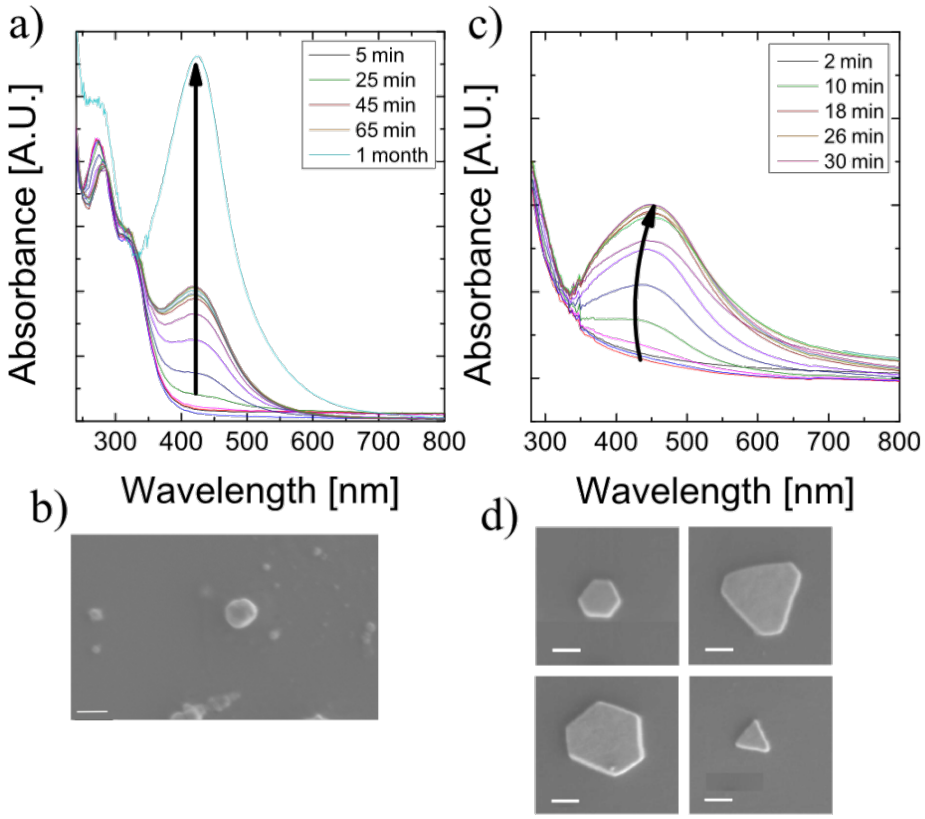

Figure 1: Time evolvement of UV–vis spectra of ≈1:10 orange extract/$AgNO_3$ solution between 5 and 65 minutes after mixing and after 1 month (a) and of ≈1:50 pineapple extract/$AgNO_3$ solution between 2 and 30 minutes after mixing (c). The arrows guide the eye between the peaks of the spectra. (b) and (d) show SEM images of typical nanoparticles prepared by using oranges and pineapples, scale bar is 100 nm.

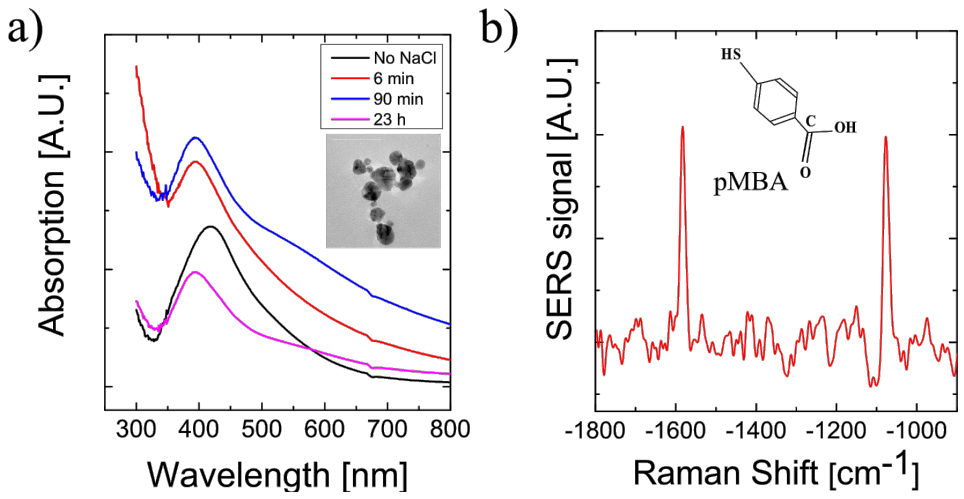

Figure 2: a) Extinction spectra of solutions of green silver nanoparticles made from orange extract before and after the addition of NaCl, final NaCl concentration was 0.2 M. The inset shows an aggregate formed by green nanoparticles. b) SERS spectrum of pMBA collected on green silver nanoparticles as enhancing nanostructure using 50 mW excitation at 785 nm.

related to plant materials introduced due to the green preparation, which prevent that particles come very close together and even touch each other. Moreover, these residual molecules might prevent that analyte molecules find optimum enhancing places in small distances to the surface of the plasmonic particles.

In general, the main differences in the outcome of the green preparation process are related to the different fruits as it is shown in Figure 1b,d. While orange extract gave rise to round and almost spherical silver particles, reduction by pineapple extract results in particles with sharp corners.

However, not only the kind of fruit determines size, shape and speed of growing of silver nanoparticles, also other experimental parameters during the green preparation process play a role. Figure 3 demonstrates the influence of light on the formation of silver nanoparticles using pineapple extract. Figure 3a shows the evolution of plasmonic particles under exactly the same conditions as used in Figure 1b. While the process shown in Figure 1b took place in the presence of light, silver particles in Figure 3a grew in the dark. Figure 3b shows the increase of the extinction over time in the presence of light and without light in a time scale normalized to the time for achieving the end of the reduction process, i.e., the time when no more increase of the extinction can be observed. The two curves show that the yield of the formation of nanoparticles is higher at the presence of light, but the time behavior in the normalized time scale is very similar. Figure 3c displays the peak position as a function of normalized time. Also this plot indicates that the chemical process with and without the presence of light might be almost the same. A difference of about 40 nm between the end peak positions in both processes indicates that the process without light resulted in larger nanoparticles.

As an additional parameter in the preparation process, we change the volume ratio between the silver nitrate solution and the fruit extract. Figure 4 shows how different ratios of silver nitrate solution and orange extract influence the evolution of

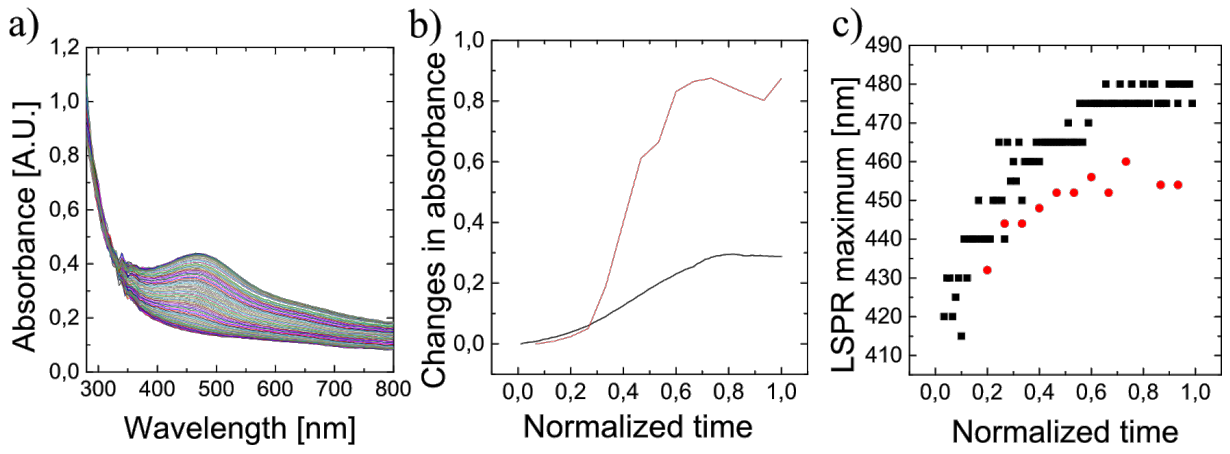

Figure 3: a) Time evolvement of UV–vis spectra of ≈1:50 pineapple extract/$AgNO_3$ solution between 0 and 180 minutes after mixing in darkness, for comparison see Figure 1c that displays the same process in the presence of light. b) Peak growth taken from Figure 1c and Figure 3a as a function of normalized time. c) Peak position taken from Figure 1c and Figure 3a as a function of normalized time. Red and black data in Figure 3b,c are with and without light, respectively.

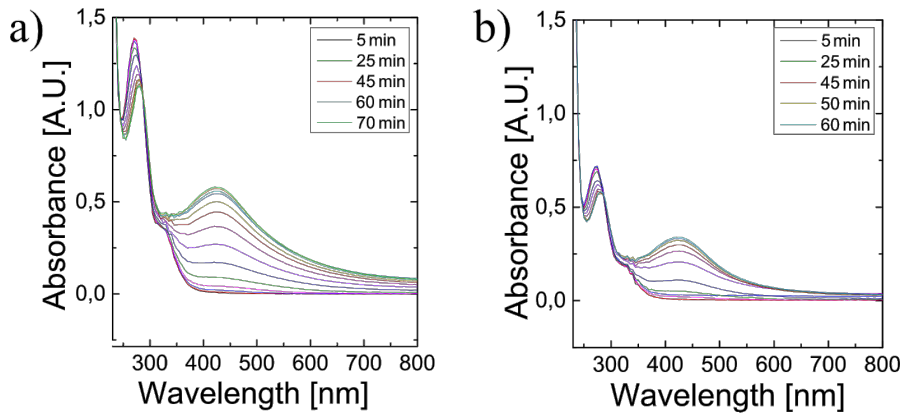

Figure 4: Time evolvement of UV–vis spectra in mixtures of orange extract and $AgNO_3$ solutions between 5 and 60 minutes after mixing. Figure 4a,b represent different ratios of $AgNO_3$ solution and orange extract with a 5 times higher ratio of the $AgNO_3$ solution to plant extract in 4b than in 4a.

silver nanoparticles. The mixture used in Figure 4b was prepared with an excess of silver nitrate solution over the orange extract compared to Figure 4a. Figure 4 shows the surface plasmon peaks always at the same position at 420 nm, i.e., the size and shape of the nanoparticles do not depend on the ratio between silver nitrate and the reducing fruit extract. Much weaker plasmon bands in Figure 4b indicate that in this experiment, the fruit extract is the limiting factor for the total yield of nanoparticles.

In addition to plasmon resonances around 420 nm, the spectra displayed in Figure 4a,b and Figure 1a show peaks in the UV range, which are related to small silver clusters that can be formed from Ag^+ available after the initial reduction process [25]. In particular, the observed UV band at 270 nm can be assigned to Ag_4^{2+} clusters, which, via intermediates Ag_7^{3+} and Ag_8^+, build up metallic particles Ag_n [25]. Figure 5 shows that the increase of the plasmon absorption at 420 nm correlates with the decrease of absorption at 270 nm related to Ag_4^{2+} confirming the conversion of silver clusters to plasmonic silver nanoparticles.

A strong luminescence signal in bright colors emitted from small silver clusters is a very interesting finding [26,27]. As it is shown in Figure 6, the presence of various silver clusters on the surface of the "green" plasmonic silver nanoparticles is also supported by a strong multicolor luminesce signal emitted by the plasmonic particles during visible excitation. The emission appears over a wide wavelength range with a strong contribution in the yellow-green region. At some places, the luminescent light shows strong fluctuations (see movie in Supporting Information File 1). These blinking hints to surface-enhanced emission of individual single emitters made from small silver clusters on the surface of plasmonic silver nanoparticles.

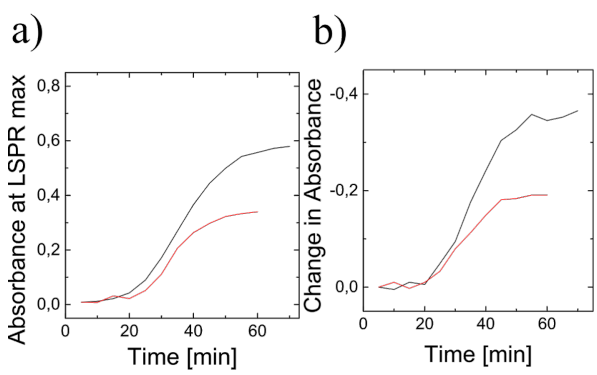

Figure 5: Time evolvement of the extinction spectrum during the formation of silver nanoparticles. The increase of the plasmon related peak at 420 nm (Figure 5a) correlates with the decrease of the peak at 270 nm related to Ag_4^{2+} clusters (Figure 5b). Red and black curves represent different ratios of $AgNO_3$ solution and orange extract.

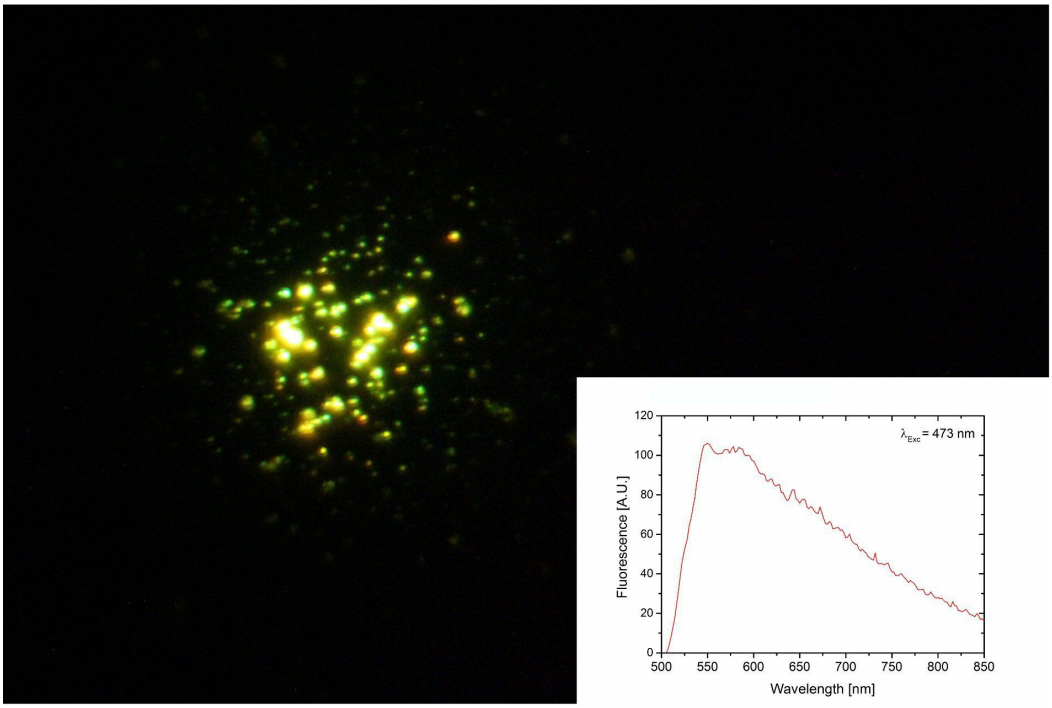

Figure 6: Image and spectrum of multicolor luminescence collected from green silver nanoparticles. The plasmonic silver particles were excited using 473 nm light provided by a 20 mW laser diode through a 100× oil immersion objective. The illuminated spot is around 10 μm^2.

Conclusion

Silver nanoparticles can be prepared in a relatively simple way by using extracts of oranges and pineapples as reducing agents. Size and shape of the particles depend mainly on the kind of fruit used in the chemical preparation process. The UV–vis absorption spectrum displays the surface plasmon resonance and also features in the UV, which can be assigned to small silver clusters. The correlation between the evolution of the surface plasmon band and the decrease of the silver cluster band in the UV confirms the conversion of silver clusters to plasmonic silver nanoparticles. Remaining single small silver clusters on the surface of the plasmonic nanoparticles give rise to a strong surface enhanced multicolor luminescence.

Experimental

Preparation of fruit extract

Ananas comosus: The pineapple extract was prepared by cutting away all parts except the yellow pulp of the pineapple. This was then sliced and blended after which the pulp was filtered through a standard coffee filter twice resulting in a yellow juice.

Citrus sinensis: The orange extract used in Figure 1 was prepared by taking an orange peel and washing it with demineralized water. Then it was cut into small pieces. 4 g of these pieces were added to 40 mL of demineralized water. This solution was then heated and stirred in a boiling water bath for 3 min. After this, it was cooled under stirring for 3 min and then filtered through a standard coffee filter followed by a 2 µm filter. The orange extract used in Figure 4 was made in exactly the same way with the difference that the 4 g of material were taken from only the white part of the orange peel.

All fruits were bought from the local supermarket. The pineapple came from South America. The oranges, sort "Valencia", came from Italy, where they were grown without the use of pesticides.

Supporting Information

A strong and fluctuating luminescence signal hints to surface-enhanced emission of individual single emitters on the surface of plasmonic silver nanoparticles.

Supporting Information File 1

Fluctuations in the luminescent light collected from green silver nanostructures (real time movie).
[http://www.beilstein-journals.org/bjnano/content/supplementary/2190-4286-6-27-S1.wmv]

Acknowledgements

This work was performed in the context of the European COST Action MP1302 "Nanospectroscopy". KBM is thankful for support from the Danish National Advanced Technology Foundation (HTF, grant no.083-2012-1).

References

1. Kneipp, J.; Kneipp, H.; Wittig, B.; Kneipp, K. *Nanomed.: Nanotechnol. Biol. Med.* **2010,** *6,* 214–226. doi:10.1016/j.nano.2009.07.009
2. Ahmad, T.; Wani, I. A.; Manzoor, N.; Ahmed, J.; Asiri, A. M. *Colloids Surf., B* **2013,** *107,* 227–234. doi:10.1016/j.colsurfb.2013.02.004
3. Stockman, M. I. *Opt. Express* **2011,** *19,* 22029–22106. doi:10.1364/OE.19.022029
4. Lal, S.; Link, S.; Halas, N. J. *Nat. Photonics* **2007,** *1,* 641–648. doi:10.1038/nphoton.2007.223
5. Aroca, R. *Surface Enhanced Vibrational Spectroscopy;* Wiley: Chichester, 2006.
6. Ozaki, Y.; Kneipp, K.; Aroca, R., Eds. *Frontiers of Surface Enhanced Raman Scattering;* Wiley: Chichester, 2014. doi:10.1002/9781118703601
7. Fojtik, A.; Henglein, A. *Ber. Bunsen-Ges.* **1993,** *97,* 252.
8. Kneipp, J.; Li, X.; Sherwood, M.; Panne, U.; Kneipp, H.; Stockman, M. I.; Kneipp, K. *Anal. Chem.* **2008,** *80,* 4247–4251. doi:10.1021/ac8002215
9. Lee, P. C.; Meisel, D. *J. Phys. Chem.* **1982,** *86,* 3391–3395. doi:10.1021/j100214a025
10. Ahmad, N.; Sharma, S. *Green Sustainable Chem.* **2012,** *2,* 141–147. doi:10.4236/gsc.2012.24020
11. Akhtar, M. S.; Panwar, J.; Yun, Y.-S. *ACS Sustainable Chem. Eng.* **2013,** *1,* 591–602. doi:10.1021/sc300118u
12. Kahrilas, G. A.; Wally, L. M.; Fredrick, S. J.; Hiskey, M.; Prieto, A. L.; Owens, J. E. *ACS Sustainable Chem. Eng.* **2014,** *2,* 367–376. doi:10.1021/sc4003664
13. Poulose, S.; Panda, T.; Nair, P. P.; Theodore, T. *J. Nanosci. Nanotechnol.* **2014,** *14,* 2038–2049. doi:10.1166/jnn.2014.9019
14. Alam, M. N.; Das, S.; Batuta, S.; Roy, N.; Chatterjee, A.; Mandal, D.; Begum, N. A. *ACS Sustainable Chem. Eng.* **2014,** *2,* 652–664. doi:10.1021/sc400562w
15. Jha, A. K.; Kumar, V.; Prasad, K. *J. Bionanosci.* **2011,** *5,* 162–166. doi:10.1166/jbns.2011.1053
16. Kaviya, S.; Santhanalakshmi, J.; Viswanathan, B.; Muthumary, J.; Srinivasan, K. *Spectrochim. Acta, Part A* **2011,** *79,* 594–598. doi:10.1016/j.saa.2011.03.040
17. Sujitha, M. V.; Kannan, S. *Spectrochim. Acta, Part A* **2013,** *102,* 15–23. doi:10.1016/j.saa.2012.09.042
18. Elemike, E. E.; Oseghale, C. O.; Chuku, A.; Labulo, A. H.; Owoseni, M. C.; Mfon, R.; Enock, O. D.; Adesuji, E. T. *Micron* **2014,** *57,* 1–5. doi:10.1016/j.micron.2013.09.003
19. Hyllested, J. Æ.; Palanco, M. E.; Hagen, N.; Mogensen, K. B.; Kneipp, K. In *Proceedings of the 24th International Conference on Raman Spectroscopy,* Aug 10–15, 2014; Jena; p 124.
20. Kneipp, J.; Kneipp, H.; Kneipp, K. *Chem. Soc. Rev.* **2008,** *37,* 1052–1060. doi:10.1039/b708459p
21. Xu, H.; Bjerneld, E. J.; Käll, M.; Börjesson, L. *Phys. Rev. Lett.* **1999,** *83,* 4357–4360. doi:10.1103/PhysRevLett.83.4357

22. Kneipp, K.; Kneipp, H.; Kneipp, J. *Acc. Chem. Res.* **2006,** *39,* 443–450. doi:10.1021/ar050107x
23. Weber, M. L.; Litz, J. P.; Masiello, D. J.; Willets, K. A. *ACS Nano* **2012,** *6,* 1839–1848. doi:10.1021/nn205080q
24. Kerker, M.; Siiman, O.; Bumm, L. A.; Wang, D.-S. *Appl. Opt.* **1980,** *19,* 3253–3255. doi:10.1364/AO.19.003253
25. Henglein, A. *J. Phys. Chem.* **1993,** *97,* 5457–5471. doi:10.1021/j100123a004
26. Lee, T.-H.; Gonzalez, J. I.; Dickson, R. M. *Proc. Natl. Acad. Sci. U. S. A.* **2002,** *99,* 10272–10275. doi:10.1073/pnas.162356799
27. Choi, S.; Dickson, R. M.; Yu, J. *Chem. Soc. Rev.* **2012,** *41,* 1867–1891. doi:10.1039/c1cs15226b

License and Terms

end of paper

3.2.2 Marta Espina Palanco, Klaus Bo Mogensen, Marina Ghlke, Zsuzsanna Heiner, Janina Kneipp, Katrin Kneipp. *Beilstein J. Nanotechnol.* 2016, 7, 834–840

In this section, 3.2.2., we report the formation of green synthesized silver nanoparticles in intact onion cell layers after the incubation of silver salts into the tissue (ref[63]). This work showed not only the capability of the tissue to provide reducing agents for the synthesis of the nanoparticles but also to provide a SERS-template where silver nanoarticles can grow, opening new possibilities for future investigations in intact plants SERS-based sensors.

Dark field microscopy and luminiscence spectroscopy were used for the characterization of the onion tissue, allowing to visualize the presence of the nanoparticles in the extracellular space of the tissue. Also, SERS and Hyper-Raman scattering (SHERS) was performed to characterize the formed plasmonics, showing signal enhancement of orders of 10^4 and 10^6. These studies brought new perspectives since plasmonic nanostructures were delivered into the extracellular space of a fresh plant tissue via the uptake of silver salts.

My contributions to this work consisted in the experimental sample preparation, also involving the design of the protocol for delivering the nanoparticles into the tissue. During this project, previous attempts to deliver nanoparticles into intact plants were also a key factor for the final development of the presented protocol in this paper. Some of the previous attempts are described in Chapter 4. Furthermore, I contributed with a literature study providing the state of art concerning the green formation of metal nanoparticles in intact tissues.

beginning of paper

BEILSTEIN JOURNAL OF NANOTECHNOLOGY

Templated green synthesis of plasmonic silver nanoparticles in onion epidermal cells suitable for surface-enhanced Raman and hyper-Raman scattering

Marta Espina Palanco[1], Klaus Bo Mogensen[2], Marina Gühlke[3], Zsuzsanna Heiner[3], Janina Kneipp[3] and Katrin Kneipp[*1,§]

Full Research Paper

Open Access

Address:
[1]Danmarks Tekniske Universitet DTU, Department of Physics, 2800 Kgs. Lyngby, Denmark, [2]Danmarks Tekniske Universitet DTU, Department of Micro- and Nanotechnology. 2800 Kgs. Lyngby, Denmark, present affiliation: Philips Biocell, Gydevang 42, 3450 Allerød, Denmark and [3]Humboldt Universität zu Berlin, 12489 Berlin, Germany

Email:
Katrin Kneipp* - kneipp@usa.net

* Corresponding author
§ Phone: +49 15152485604

Keywords:
biotemplates; green preparation; onion; plasmonic nanoparticles; surface-enhanced Raman scattering; surface-enhanced hyper-Raman scattering

Beilstein J. Nanotechnol. **2016,** *7,* 834–840.
doi:10.3762/bjnano.7.75

Received: 19 March 2016
Accepted: 31 May 2016
Published: 09 June 2016

This article is part of the Thematic Series "Physics, chemistry and biology of functional nanostructures III".

Guest Editor: A. S. Sidorenko

Abstract

We report fast and simple green synthesis of plasmonic silver nanoparticles in the epidermal cells of onions after incubation with $AgNO_3$ solution. The biological environment supports the generation of silver nanostructures in two ways. The plant tissue delivers reducing chemicals for the initial formation of small silver clusters and their following conversion to plasmonic particles. Additionally, the natural morphological structures of the onion layers, in particular the extracellular matrix provides a biological template for the growth of plasmonic nanostructures. This is indicated by red glowing images of extracellular spaces in dark field microscopy of onion layers a few hours after $AgNO_3$ exposure due to the formation of silver nanoparticles. Silver nanostructures generated in the extracellular space of onion layers and within the epidermal cell walls can serve as enhancing plasmonic structures for one- and two-photon-excited spectroscopy such as surface enhanced Raman scattering (SERS) and surface enhanced hyper-Raman scattering (SEHRS). Our studies demonstrate a templated green preparation of enhancing plasmonic nanoparticles and suggest a new route to deliver silver nanoparticles as basic building blocks of plasmonic nanosensors to plants by the uptake of solutions of metal salts.

Introduction

Nanostructures made from metals, such as silver, gold, aluminium or palladium in various sizes and shapes attract growing attention because of their interesting properties and broad applications in many different fields of science, technology and medicine [1]. Particularly exciting applications of metal nanostructures exploit the resonant interaction of light with the collective oscillations of the free electrons, so-called surface plasmons. These resonances can give rise to strongly enhanced and highly confined local optical fields in the vicinity of metal nanostructures. Plasmonic field enhancement enables optical and spectroscopic measurements at unprecedented sensitivity and spatial resolution [2]. For chemical analysis, Raman spectroscopy performed in enhanced local fields allows for the detection and structural characterization of single molecules [3]. Beside these advances in sensing and probing, plasmonics has the potential to revolutionize almost all photonic technologies [4].

Numerous technologically and medically relevant applications and particularly also the rapid development of plasmonics as a field of research generate a strong interest in manufacturing metal nanostructures of well-defined morphologies that support plasmon resonances at very different energies within the entire optical spectral range. Moreover, metal nanostructures should be prepared in simple and fast, cheap and also environmentally friendly processes.

Very popular preparation methods of silver and gold nanostructures are based on bottom-up processes, where nanoparticles, are built from smaller structures such as metal ions. Sodium citrate and sodium borohydride are very common reducing chemicals for metal salts [5,6], but also more eco-friendly compounds such as glucose or starch can be used for the preparation of metal nanoparticles [7,8].

Overall, various reducing and stabilization agents as well as variations in experimental conditions during the preparation process, such as the influence of light or temperature , as well as sonochemical preparation routes allow for the synthesis of silver and gold nanoparticles of various sizes and shapes [9,10]. Additionally, appropriate templates for the growing process can define and control size, shape and assembling of nanostructures [9,11,12].

During the last decade, so-called “green synthesis” came into the focus of interest, since many molecules typically available in biological living matter have the capability to reduce silver and gold salts. It has been demonstrated that plants and also microorganisms such as algae, fungi, yeasts, and bacteria provide chemicals suitable for the preparation of metal nanoparticles [13,14]. For example, different parts of plants contain polysaccharides, phenolics, or flavonoids, to mention only a few compounds, which could serve as reducing and also stabilizing agents. The preparation of silver and gold nanoparticles using many very different pre-treated plant materials, such as extracts collected from leafs or vegetables and fruits has been demonstrated in numerous publications [15-19]. The diversity of bioorganic molecules available in plants provides many combinations of reducing and stabilizing agents. This gives rise to a broad variety of parameters in the green preparation process, resulting in metal nanoparticles of different sizes and shapes.

While pre-treated plant materials such as extract and juice have been used in former studies [14,15,18-20]. In this article, we demonstrate and discuss the green preparation of plasmonic silver nanoparticles in intact onion epidermal cells after incubation with $AgNO_3$ solution. The onions deliver reducing and stabilizing chemicals, while the histological structure of the onion layer, in particular the cell walls and the extracellular space they surround provide a biological template for the growth process of plasmonic silver structures. In our experimental study, we exploit luminescence spectroscopy and dark-field microscopy for probing the formation of metal nanostructures in situ in the onion tissue. Local optical fields related to the plasmonic nanostructures are probed by surface-enhanced Raman scattering (SERS) and two-photon-excited analogous surface-enhanced hyper-Raman scattering (SEHRS) [21,22]. While SERS signals scale with the local optical field strengths by 10^4, SEHRS signals have a scaling factor of 10^6. This high non-linearity makes SEHRS a very sensitive method to probe spatial variations in local fields and to localize plasmonic nanostructures, surpassing also SERS. Here we compare SEHRS images and bright field microscopy of the onion cell layers. Additionally, our SERS and SEHRS experiments give evidence of the capability of the “green” silver nanostructures to enhance one- and two-photon-excited optical processes.

Experimental

Sample preparation

A single cell layer of a red onion, purchased from the supermarket, was peeled from fresh vegetables and pieces of about 1 cm^2 were placed in an aqueous silver nitrate solution (10^{-3} M concentration from 99.9% pure $AgNO_3$, Sigma-Aldrich Denmark A/S). After 20 h of incubation at room temperature and in darkness, the pieces were removed, rinsed with tap water and placed on a glass slide to dry for several hours, also in darkness. After drying, the samples were ready for optical experiments. In order to also explore the potential formation of gold nanostructures in onion layers and for a comparison between

green preparation of silver and gold nanostructures, the same sample preparation was applied using aqueous chloroauric acid, $HAuCl_4$ (10^{-3} M, Sigma-Aldrich Denmark A/S) instead of $AgNO_3$.

Luminescence measurements and dark-field microscopy

Luminescence spectra and images were measured through a 100× oil immersion objective (Leica DMLM microscope) using a laser diode (473 nm, ca. 20 mW) for excitation and equipped with a λ = 520 nm long-wave pass filter for emission. Dark Field microscopy was carried out using a Nikon eclipse LN200N microscope with 50 W halogen lamp for illuminating the sample. The spectra were collected using a fiber-coupled spectrum analyzer (Spectro 320, Instrument Systems, Germany).

SERS and SEHRS measurements

Surface-enhanced Raman and hyper-Raman spectra of a test analyte (crystal violet) attached to the onion layer were measured at a customized experimental set-up for Raman microscopy using one- and two-photon excitation [23]. The same objective (NA = 1.2) was used for providing the excitation laser and for collecting the scattered light. Placing the sample on a moving stage allows for the collection of SERS and SEHRS images. Two-photon excited hyper-Raman signals were generated by 1064 nm mode-locked Nd:YAG laser excitation (7 ps pulse duration, 76 MHz repetition rate). The second harmonic wave length of this laser at 532 nm was used for one-photon excitation. Applied peak photon flux densities at the samples were 1×10^{29} photons·cm^{-2}·s^{-1} and 5×10^{25} photons·cm^{-2}·s^{-1} and collection times were 10 s and 2 s for SEHRS and SERS spectra, respectively. Signal strengths for creating images were determined by reading out the maximum signal of the band at 1175 cm^{-1} and subtracting the signal at 1130 cm^{-1} as background.

Results and Discussion

Among various plant materials applied for green synthesis of metal nanoparticles, also the use of onion extract for the preparation of gold and silver nanoparticles has been reported [24,25]. In all those studies, onions have been crushed and boiled and finally, onion extract has been employed in the preparation process. Here, we explore the in situ preparation of metal nanoparticles in intact fresh onion cell layers at room temperature. After about 20 h of exposure to $AgNO_3$ solution, and a following drying period of 2–3 h, the onion samples appear in a reddish color, compared to their initial whitish color, suggesting the formation of nanoparticles. Additionally, Figure 1 shows a strong luminescence signal in yellow-greenish colors emitted from the onion layers upon excitation at 473 nm.

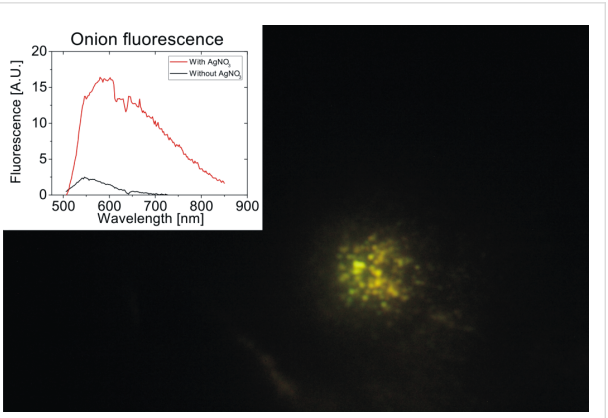

Figure 1: Image and spectrum of multi-color luminescence collected from onion cell layers after incubation with $AgNO_3$. The excitation wavelength was at 473 nm provided by a laser diode operated at around 5 mW through a 100× oil immersion objective. The illuminated spot is ca. 10 μm^2.

In general, bright luminescence signals have been discovered as characteristic optical signatures of small silver clusters [26]. The luminescence observed from the onion layer hints to the existence of small silver clusters Ag_n^+ formed from Ag^+ available after the initial reduction process of $AgNO_3$ [27]. The presence of various small silver clusters in the onion tissue is supported by previous observations reported for the green synthesis of silver nanoparticles using orange extract [19]. There, the same fluorescence signals as shown in Figure 1 have been observed [19]. UV absorption measurements in this study show a band at 270 nm, confirming the existence of Ag_4^{2+} clusters, which, via intermediate larger clusters, eventually form metallic particles Ag_n [27]. From these small metal particles, plasmonic silver particles grow by coalescence [27,28]. The dark red color of the onion layer described above is an indicator that plasmonic silver nanoparticles have formed, including also the formation of aggregates.

Dark field microscopy provides more detailed spatial information about where these silver nanostructures exist. The red glowing of the extracellular matrix of the onion layer in the dark field images shown in Figure 2 is due to the scattered light from silver nanoparticles and their aggregates. The dark field images of the onion cell layer show that the plasmonic silver nanostructures grow preferentially in the extracellular matrix between the epidermal cells of the onion tissue. The luminescence pattern in Figure 1 shows that some silver ions are taken up into the protoplast during the osmotic imbalance when the hypertonic silver salt solution is added, and the small clusters must be stabilized there. In contrast, at the outer cell walls and in the extracellular space a biomolecular environment is provided that enables the templated growth and the stabilization of larger plasmonic nanoparticles. As suggested by uptake studies

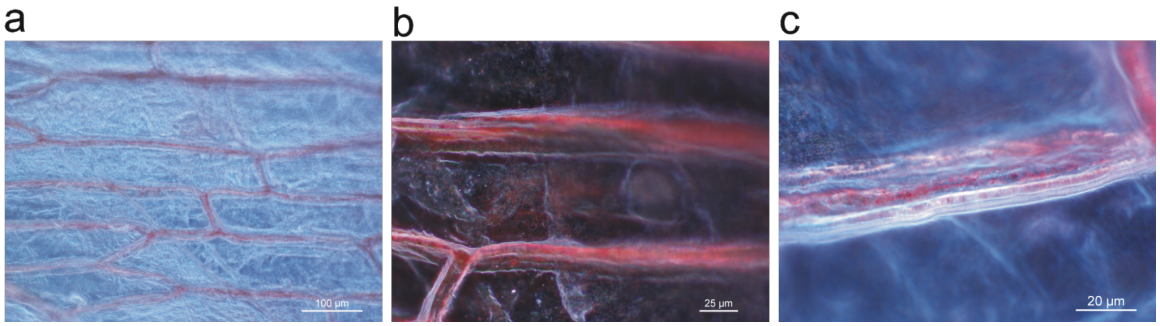

Figure 2: Dark field images of onion cell layers after incubation with $AgNO_3$ solution. The magnification is a) 10×, b) 20× and c) 50×, respectively. Scattering of red light originating from silver nanoparticles appears in the extracellular space of the epithelial layer.

with other metal ions into epidermal cells, adsorption of the silver to the extracellular matrix is expected to be faster than uptake into the cells [29]. Several molecular candidates can be responsible for the reduction and stabilization of the nanoparticles in these regions, specifically pectin, which is part of the cell wall, and which has been shown to be an efficient reducing and stabilizing agent for the synthesis of silver nanoparticles in several studies [30-32]. Glycoproteins that have a function in cellular adhesion or have enzymatic activity such as alliinase, which is a major protein component of *Allium sp*., provide several possibilities for the reduction and the stabilization of the silver metal nanoparticles.

For comparison, Figure 3 shows dark field images of onion cell layers after 20 h of incubation with chloroauric acid. The onion samples incubated in chloroauric acid did not show any change of color after drying. In the dark field micrographs, yellow light scattered from small gold nanoparticles shows that these gold structures are formed only at a few points without any correlation to the cellular structure of the epithelial tissue. A templating effect due to the cellular matrix of the onion layer as it has been observed for silver does not exist for the formation of gold nanoparticles.

Raman scattering experiments performed on onion cell layers exposed to $HAuCl_4$ show a strong Raman line at 346 cm^{-1}, which exists across the entire sample. This line can be assigned to an Au–Cl stretching vibration [33] and indicates the presence of a large amount of excess gold chloride. This suggests that reduction agents available in the onion layers are obviously not very efficient for the reduction of $HAuCl_4$. This is surprising since onion extract was reported to work well for the reduction of $HAuCl_4$ [24]. On the other hand, green synthesis involves complex mixtures of molecules with both reducing and stabilizing function, which can indeed be different in plant extracts and in plant tissue, where compartmentalization and spatial separation also play a role. Our experiments indicate that the chemical composition and micromorphological structure in onion epidermal tissue is much more efficient for the reduction of $AgNO_3$ than for the reduction of $HAuCl_4$.

In the following, we check silver and gold nanostructures grown in onion cell layers regarding their capability as field-enhancing plasmonic structures. SERS tests on onion layer–gold samples as shown for example in Figure 3 using 633 and 785 nm excitation wavelengths and crystal violet (CV) as test analyte resulted in only very weak SERS signals that were collected only from

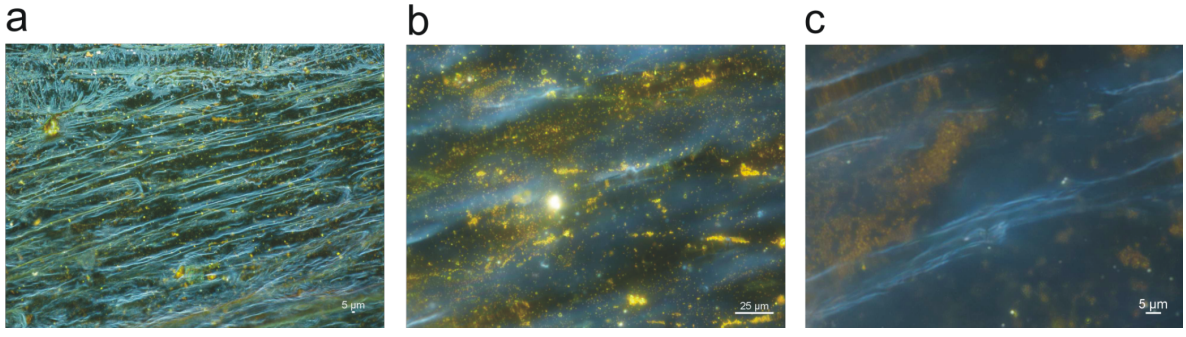

Figure 3: Dark field images of onion layers after incubation with $HAuCl_4$ solution, using a similar protocol as in Figure 2. The magnification is a) 10×, b) 20× and c) 50×, respectively. The scattering of yellow light originating from gold nanoparticles appears without any correlation to the cellular structure of the onion layer.

particular places of the sample where gold nanostructures were found (data not shown). The extremely poor SERS signals indicate that the gold nanostructures formed in the onion layers do not support high local fields.

In contrast, silver nanostructures grown in onion layers are well suited for SERS experiments. Figure 4a shows a typical SERS spectrum collected from CV attached to onion–silver samples. The strongest SERS signals were obtained from the region of extracellular space and cell walls. We did not measure SERS signals that we could ascribe to intrinsic biomolecules present in the plant tissue. This is in accordance with the assumption that mainly carbohydrate species (such as pectin) are present the cell walls and in the extracellular space and with the finding that SERS measurements of these molecules require special functionalization of the silver nanostructures [34]. Furthermore, the intrinsic plant molecules are probably present at much lower concentrations than the test molecule, where about 1000–2000 CV molecules contribute to the observed SERS signals. Moreover, at the applied 532 nm excitation, CV benefits from additional resonance enhancement as a further advantage over colorless biomolecules.

In addition to one-photon-excited SERS we checked the silver nanostructures in onion layers also by two-photon-excited SEHRS. In a hyper-Raman process, two photons are scattered simultaneously and the hyper-Raman spectrum appears shifted relative to the second harmonic of the excitation laser. Since we excited normal SERS using the second harmonic of the 1064 nm SEHRS excitation laser, SERS and SEHRS spectra shown in Figure 4a and Figure 4b, respectively, appear in the same spectral range. Figure 4b shows a typical SEHRS spectrum collected from the same sample. Spectra in Figure 4a and Figure 4b show the well-known Raman and hyper-Raman features of CV [35].

The main enhancement mechanism for SERS and SEHRS are high local fields in the vicinity of metal nanostructures related to resonances between light and surface plasmon modes of these structures [36]. Therefore, SERS or SEHRS can be exploited to probe local optical fields [37]. As mentioned above, its high non-linearity makes SEHRS a very sensitive tool to image spatial variations in local fields and to localize plasmonic nanostructures. Here we perform SEHRS scans across the onion sample. A SEHRS image, shown in Figure 4c, indicates that places displaying highest SEHRS signals correlate with the extracellular space and cell walls in the onion cell layer. SEHRS images support the finding from dark field images and show that plasmonic silver nanoparticles are formed and confined to the extracellular space and cell walls.

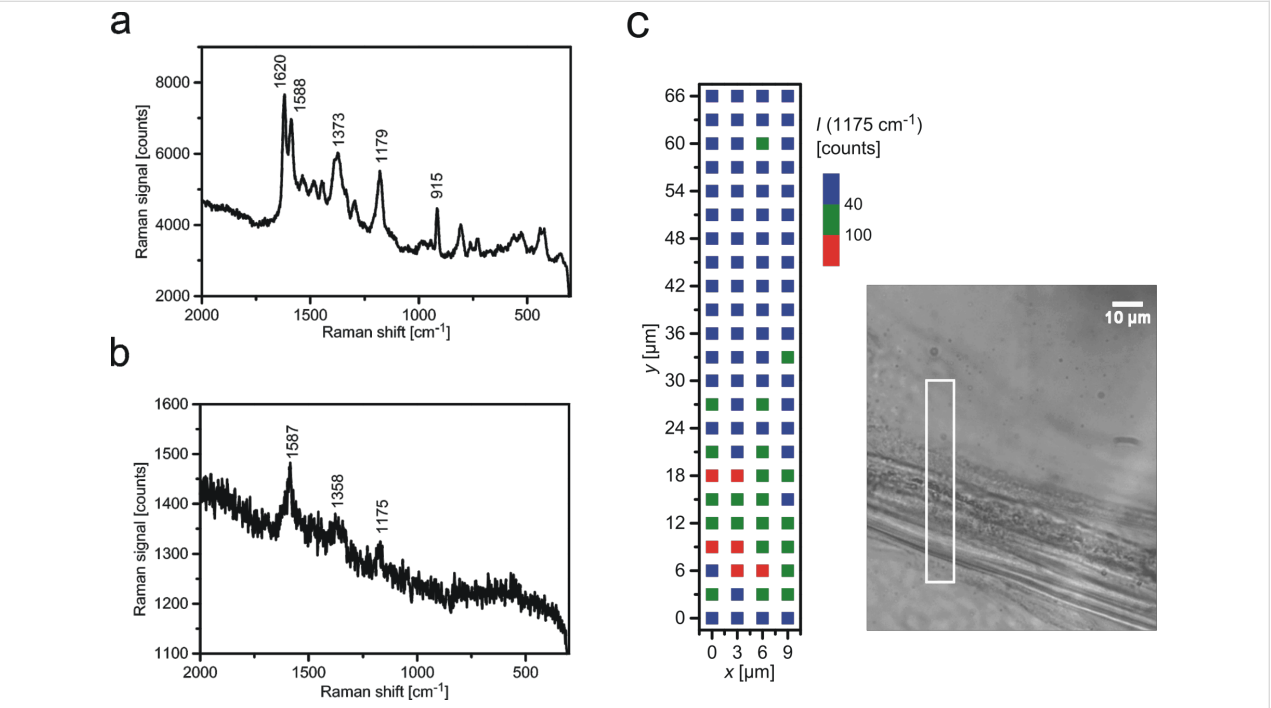

Figure 4: SERS and SEHRS measured from crystal violet attached to an onion cell layer containing plasmonic silver nanostrcutures in the extracellular space. a) SERS spectrum of crystal violet measured using 23 µW pulsed excitation at 532 nm, collection time 2 s. b) SEHRS spectrum of crystal violet measured using 1064 nm pulsed excitation; collection time 10 s. About 10^3 molecules contribute to the obtained SERS and SEHRS signals. c) Two-photon-excited hyper-Raman image collected from the rectangle shown in the bright field picture of the onion layer. The image displays the 1175 cm^{-1} SEHRS band (see spectrum in panel b). The color code represents the signal from lowest (blue) to highest (red).

Conclusion

Our studies demonstrate the green synthesis of plasmonic silver nanoparticles in onion layers after incubation with $AgNO_3$ solution without any additional reducing or stabilizing chemicals. The plant delivers not only the required chemicals, the extracellular matrix including cell walls in the onion layer also provide a bio-template for growing the plasmonic silver nanostructures. Green silver nanostructures grown in the cell walls and extracellular space are suited for enhancing one- and two-photon-excited surface enhanced Raman and hyper-Raman scattering, respectively. Our studies suggest also the preparation of silver nanoparticles directly inside living plants after the uptake of solutions of metal salts. This would be of particular interest as an efficient method to deliver silver nanoparticles as basic building blocks of SERS nanosensors [38-40] to study chemical compositions and processes inside plants.

Acknowledgements

We thank Harald Kneipp for support of the experiments and useful discussion. MG, ZH and JK acknowledge funding by ERC Grant 259432 MULTIBIOPHOT. ZH acknowledges funding by DFG GSC 1013 (SALSA). This work was performed in the context of the European COST Action MP1302 Nanospectroscopy

References

1. Zamborini, F. P.; Bao, L.; Dasari, R. *Anal. Chem.* **2012,** *84,* 541–576. doi:10.1021/ac203233q
2. Meixner, A. J.; Leiderer, P. *Beilstein J. Nanotechnol.* **2014,** *5,* 186–187. doi:10.3762/bjnano.5.19
3. Ozaki, Y.; Kneipp, K.; Aroca, R., Eds. *Frontiers of Surface-Enhanced Raman Scattering: Single Nanoparticles and Single Cells;* John Wiley & Sons: Chichester, United Kingdom, 2014. doi:10.1002/9781118703601
4. Stockman, M. I. *Opt. Express* **2011,** *19,* 22029–22106. doi:10.1364/OE.19.022029
5. Creighton, J. A.; Blatchford, C. G.; Albrecht, M. G. *J. Chem. Soc., Faraday Trans. 2* **1979,** *75,* 790–798. doi:10.1039/f29797500790
6. Lee, P. C.; Meisel, D. *J. Phys. Chem.* **1982,** *86,* 3391–3395. doi:10.1021/j100214a025
7. Engelbrekt, C.; Sørensen, K. H.; Zhang, J.; Welinder, A. C.; Jensen, P. S.; Ulstrup, J. *J. Mater. Chem.* **2009,** *19,* 7839–7847. doi:10.1039/b911111e
8. Pienpinijtham, P.; Han, X. X.; Suzuki, T.; Thammacharoen, C.; Ekgasit, S.; Ozaki, Y. *Phys. Chem. Chem. Phys.* **2012,** *14,* 9636–9641. doi:10.1039/c2cp40330g
9. Rycenga, M.; Cobley, C. M.; Zeng, J.; Li, W.; Moran, C. H.; Zhang, Q.; Qin, D.; Xia, Y. *Chem. Rev.* **2011,** *111,* 3669–3712. doi:10.1021/cr100275d
10. Salkar, R. A.; Jeevanandam, P.; Aruna, S. T.; Koltypin, Y.; Gedanken, A. *J. Mater. Chem.* **1999,** *9,* 1333–1335. doi:10.1039/a900568d
11. Young, K. L.; Ross, M. B.; Blaber, M. G.; Rycenga, M.; Jones, M. R.; Zhang, C.; Senesi, A. J.; Lee, B.; Schatz, G. C.; Mirkin, C. A. *Adv. Mater.* **2014,** *26,* 653–659. doi:10.1002/adma.201302938
12. Pushpavanam, K.; Santra, S.; Rege, K. *Langmuir* **2014,** *30,* 14095–14103. doi:10.1021/la5041568
13. Zeiri, L. *J. Raman Spectrosc.* **2007,** *38,* 950–955. doi:10.1002/jrs.1714
14. Akhtar, M. S.; Panwar, J.; Yun, Y.-S. *ACS Sustainable Chem. Eng.* **2013,** *1,* 591–602. doi:10.1021/sc300118u
15. Ahmad, N.; Sharma, S. *Green Sustainable Chem.* **2012,** *2,* 141–147. doi:10.4236/gsc.2012.24020
16. Kahrilas, G. A.; Wally, L. M.; Fredrick, S. J.; Hiskey, M.; Prieto, A. L.; Owens, J. E. *ACS Sustainable Chem. Eng.* **2014,** *2,* 367–376. doi:10.1021/sc4003664
17. Alam, M. N.; Das, S.; Batuta, S.; Roy, N.; Chatterjee, A.; Mandal, D.; Begum, N. A. *ACS Sustainable Chem. Eng.* **2014,** *2,* 652–664. doi:10.1021/sc400562w
18. Poulose, S.; Panda, T.; Nair, P. P.; Theodore, T. *J. Nanosci. Nanotechnol.* **2014,** *14,* 2038–2049. doi:10.1166/jnn.2014.9019
19. Hyllested, J. Æ.; Palanco, M. E.; Hagen, N.; Mogensen, K. B.; Kneipp, K. *Beilstein J. Nanotechnol.* **2015,** *6,* 293–299. doi:10.3762/bjnano.6.27
20. Zuas, O.; Hamim, N.; Sampora, Y. *Mater. Lett.* **2014,** *123,* 156–159. doi:10.1016/j.matlet.2014.03.026
21. Kneipp, K.; Kneipp, H.; Kneipp, J. *Acc. Chem. Res.* **2006,** *39,* 443–450. doi:10.1021/ar050107x
22. Kneipp, J.; Kneipp, H.; Kneipp, K. *Proc. Natl. Acad. Sci. U. S. A.* **2006,** *103,* 17149–17153. doi:10.1073/pnas.0608262103
23. Gühlke, M.; Heiner, Z.; Kneipp, J. *Phys. Chem. Chem. Phys.* **2015,** *17,* 26093–26100. doi:10.1039/c5cp03844h
24. Parida, U. K.; Bindhani, B. K.; Nayak, P. *World J. Nano Sci. Eng.* **2011,** *1,* 93–98. doi:10.4236/wjnse.2011.14015
25. Abboud, Y.; Eddahbi, A.; El Bouari, A.; Aitenneite, H.; Brouzi, K.; Mouslim, J. *J. Nanostruct. Chem.* **2013,** *3,* 84–90. doi:10.1186/2193-8865-3-84
26. Choi, S.; Dickson, R. M.; Yu, J. *Chem. Soc. Rev.* **2012,** *41,* 1867–1891. doi:10.1039/c1cs15226b
27. Henglein, A. *J. Phys. Chem.* **1993,** *97,* 5457–5471. doi:10.1021/j100123a004
28. Polte, J.; Tuaev, X.; Wuithschick, M.; Fischer, A.; Thuenemann, A. F.; Rademann, K.; Kraehnert, R.; Enmmerling, F. *ACS Nano* **2012,** *6,* 5791–5802. doi:10.1021/nn301724z
29. Brune, A.; Urbach, W.; Dietz, K.-J. *Plant, Cell Environ.* **1994,** *17,* 153–162. doi:10.1111/j.1365-3040.1994.tb00278.x
30. Kong, J. M.; Wong, C. V.; Gao, Z. Q.; Chen, X. T. *Synth. React. Inorg., Met.-Org., Nano-Met. Chem.* **2008,** *38,* 186–188. doi:10.1080/15533170801926218
31. Zahran, M. K.; Ahmed, H. B.; El-Rafie, M. H. *Carbohydr. Polym.* **2014,** *111,* 971–978. doi:10.1016/j.carbpol.2014.05.028
32. Tummalapalli, M.; Deopura, B. L.; Alam, M. S.; Gupta, B. *Mater. Sci. Eng., C* **2015,** *50,* 31–36. doi:10.1016/j.msec.2015.01.055
33. Stammreich, H.; Forneris, R. *Spectrochim. Acta* **1960,** *16,* 363. doi:10.1016/0371-1951(60)80097-5
34. Stuart, D. A.; Yonzon, C. R.; Zhang, X.; Lyandres, O.; Shah, N. C.; Glucksberg, M. R.; Walsh, J. T.; Van Duyne, R. P. *Anal. Chem.* **2005,** *77,* 4013–4019. doi:10.1021/ac0501238
35. Kneipp, K.; Kneipp, H.; Seifert, F. *Chem. Phys. Lett.* **1995,** *233,* 519. doi:10.1016/0009-2614(94)01513-U
36. Moskovits, M. *Rev. Mod. Phys.* **1985,** *57,* 783–826. doi:10.1103/RevModPhys.57.783

37. Kneipp, K.; Kneipp, H.; Kneipp, J. *Chem. Sci.* **2015,** *6,* 2721–2726. doi:10.1039/c4sc03508a
38. Kneipp, J.; Kneipp, H.; Kneipp, K. *Chem. Soc. Rev.* **2008,** *37,* 1052–1060. doi:10.1039/b708459p
39. Matschulat, A.; Drescher, D.; Kneipp, J. *ACS Nano* **2010,** *4,* 3259–3269. doi:10.1021/nn100280z
40. Kneipp, J.; Kneipp, H.; Wittig, B.; Kneipp, K. *Nanomedicine* **2010,** *6,* 214–226. doi:10.1016/j.nano.2009.07.009

License and Terms

end of paper

3.3 Other plasmonic nanostructures to perform SERS

In the following section, 3.3.1., aluminum SERS-substrates were used to enhance Raman signals using near infrared laser excitations[77]. The studies suggested that the geometry of the metal nanoparticles is as important as the dielectric properties for the performance of a SERS measurement. Aluminum evaporated at different thicknesses in films were used for these experiments. The characterization of the films was carried out by scanning electron microscopy, electron energy loss spectroscopy (EELS), measuring the excitation coefficient spectra of the samples as well as SERS measurements of an attach molecule pMBA on the Aluminum films. My contributions to this work was the measurements of the SERS spectrum of pMBA and adenine on the different thicknesses of the aluminum films, using the setup described in Chapter 2.

3.3.1 K.B. Mogensen, M. Ghlke, J. Kneipp, S. Kadkhodazadeh, J.B. Wagner, M. Espina Palanco, H. Kneipp and K. Kneipp. *Royal Society of Chemistry* 2014, 50, 3744–3746.

beginning of paper

ChemComm

COMMUNICATION

View Article Online
View Journal | View Issue

Surface-enhanced Raman scattering on aluminum using near infrared and visible excitation

Cite this: *Chem. Commun.*, 2014, 50, 3744

Received 6th January 2014,
Accepted 17th February 2014

DOI: 10.1039/c4cc00010b

www.rsc.org/chemcomm

Klaus Bo Mogensen,[a] Marina Gühlke,[b] Janina Kneipp,[bc] Shima Kadkhodazadeh,[d] Jakob B. Wagner,[d] Marta Espina Palanco,[e] Harald Kneipp[e] and Katrin Kneipp*[e]

We observed strong surface-enhanced Raman scattering on discontinuous nanostructured aluminum films using 785 nm excitation even though dielectric constants of this metal suggest plasmon supported spectroscopy in the ultraviolet range. The excitation of SERS correlates with plasmon resonances in the 1.3–2.5 eV range identified in electron energy loss spectra.

Surface-enhanced Raman scattering (SERS), that is, Raman scattering taking place in enhanced and highly confined local fields[1] is one of the most prominent plasmon supported spectroscopic effects. The creation of strong local fields depends on the dielectric constant ε_m of the metal and requires a negative real part of the complex dielectric constant. Additionally, in order to achieve high enhancement levels, plasmons should exhibit small damping, *i.e.* the imaginary part of ε_m has to be small.[2] Gold and silver nanospheres fulfil these requirements in the visible and violet range, respectively, and are the most common materials in plasmon supported optics and spectroscopy. In particular, surface plasmon resonances of these metals can be shifted to lower energies not only by variations in shape and size of the nanoparticles, and the formation of nanoshells, but also by coupling of plasmons in composites of nanoparticles, such as in aggregates and in arrays.[3] This enables plasmon support by silver and gold in the entire visible and near infrared (NIR) wavelength range. There is also a strong interest in the extension of SERS and other plasmon enhanced spectroscopy techniques, and plasmon supported photonics in general, to shorter wavelengths. Aluminum is considered to be a promising material for employing plasmonics in the ultraviolet (UV)-range.[4,5] UV SERS experiments using various Al nanostructures have been reported.[6–10] The overall potential capabilities of this metal have been discussed based on computational and experimental characterization of its surface plasmon spectrum.[11–16] These studies show that Al nanostructures exhibit plasmon resonances in the UV range for isolated small spherical particles. But, as for other metals, with increasing sizes and aspect ratios of Al nanoparticles,[12,16] and also interacting nanostructures such as arrays of Al nanostructures[11] or metal films with nanoholes,[13] plasmon resonances can shift to lower energies and appear in the visible and even in the NIR range. Additional shifts in the plasmon resonances to longer wavelengths can occur due to the formation of aluminum oxide.[13,16] This makes aluminum interesting for its application in plasmonics in the entire optical range from UV to NIR.

Here we study SERS of molecules on discontinuous nanostructured Al films. In particular, we want to explore SERS capabilities of these films beyond the UV range at longer wavelength excitations. The films are prepared by evaporating aluminum at various thicknesses on glass substrates followed by annealing.

Fig. 1 shows SEM images of an annealed Al film along with extinction spectra of evaporated films before and after annealing. Compared to other metals, the plasma resonance of aluminum appears at a relatively high energy at 15 eV. Therefore, smooth aluminum films show a strong reflectivity in the entire optical

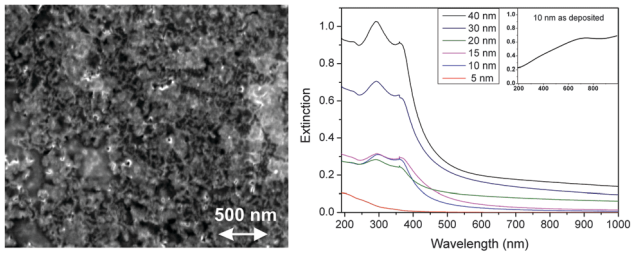

Fig. 1 SEM image of an annealed Al film and optical extinction spectra of a smooth aluminum film (inset) and annealed films (700 °C for 10 min in forming gas) at varying thicknesses.

[a] *Danmarks Tekniske Universitet DTU, Department of Micro- and Nanotechnology, 2800 Kgs. Lyngby, Denmark*
[b] *Humboldt Universität zu Berlin, Department of Chemistry, 12489 Berlin, Germany*
[c] *BAM Federal Institute for Materials Research and Testing, 12489 Berlin, Germany*
[d] *Danmarks Tekniske Universitet DTU, Center for Electron Nanoscopy, 2800 Kgs. Lyngby, Denmark*
[e] *Danmarks Tekniske Universitet DTU, Department of Physics, 2800 Kgs. Lyngby, Denmark. E-mail: katrin.kneipp@fysik.dtu.dk*

range from UV to NIR (see the inset in Fig. 1). The discontinuous aluminum films formed after annealing display a changed extinction spectrum. The films now show broad extinction features in the UV range. Similar changes in the extinction spectra have recently been reported for the formation of small Al nanoparticles from nanostructured aluminum films with thicknesses between 2.5 and 8 nm.[17] While the formation of isolated Al nanoparticles, as discussed in ref. 17, results in an absorption at around 200 nm, discontinuous Al films with thicknesses between 10 and 40 nm give rise to extinction spectra up to 400 nm. Freshly prepared Al-films do not show any intrinsic Raman signature, but a very thin aluminum oxide layer of a few nanometers might exist on these films. After several days, a Raman line at $\sim$500 cm^{-1} appears which is probably due to the oxidation of the film. The reported SERS studies have been performed on fresh films.

Fig. 2 shows SERS spectra using discontinuous Al-films as enhancing nanostructures and 785 and 532 nm excitation. Molecules for the Raman experiments were applied to the film in 5 μL droplets of 10^{-6}–10^{-4} M aqueous solution spread over $\sim$10 mm^2. After evaporation, spectra were collected in a 180° backscattering geometry using the same objective for excitation and collection of the scattered light. Depending on the concentration of the target molecule in the droplet, 3×10^5–3×10^7 molecules are present in the $\sim$1 μm^2 probed area on the film. All target molecules, adenine, *para*-mercaptobenzoic acid (pMBA) and *para*-aminothiophenol (pATP) have their electronic absorption in the UV range, so that there is no resonance Raman contribution to the SERS enhancement at the applied excitation.

SERS spectra of all three molecules are in agreement with NIR-SERS spectra reported for these molecules on gold or silver. There is no Raman spectroscopic indication for a chemical interaction of the molecules with aluminum or aluminum oxide.

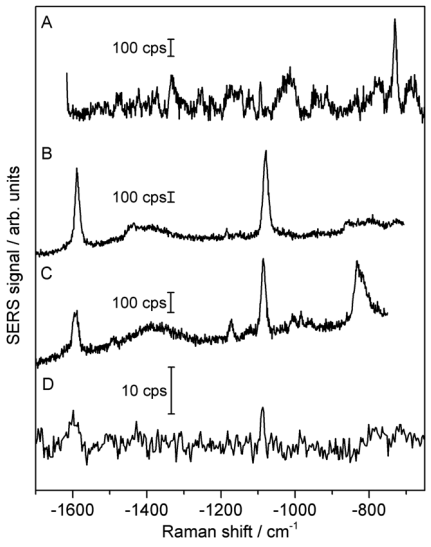

Fig. 2 SERS spectra measured on discontinuous aluminum films. Spectra A–C: SERS collected from 3×10^5 molecules of adenine, pMBA and pATP, respectively, using 785 nm excitation, spectrum D: SERS collected from $\sim 10^7$ molecules of pATP using 532 nm excitation. Excitation 10^5–10^6 W cm^{-2}, collection time 1 s (spectra A–C) and 10 s (spectrum D).

It is noteworthy that in our NIR excited non-resonant SERS experiment with adenine, the ring breathing mode at 730 cm^{-1} is the dominating spectral feature. This is different from UV-excited and hence resonant SERRS spectra of adenine on aluminum, where mainly the stretching modes of various CN bonds at around 1335 cm^{-1} were reported previously.[9,10]

Our experiments show that 785 nm excitation results in much stronger SERS signals than 532 nm excitation. At 532 nm excitation, only pATP at higher concentrations gives rise to a measurable SERS spectrum. This could be explained by a possible "chemical" contribution to SERS enhancement for this molecule as it has been discussed,[18] while the electromagnetic field enhancement is only very weak at 532 nm excitation. Excitation at 405 nm did not result in any detectable SERS signal.

We can understand the strong SERS enhancement particularly at NIR excitation in the framework of the plasmonic properties of discontinuous metal films. Theory predicts intense and extremely localized fields, so-called hot spots, for aggregates formed by metal nanoparticles, fractal structures and semi-continuous random metal films related to specific plasmonic eigenmodes in these structures.[19–22] These hot spots have been experimentally verified for silver and gold nanostructures. For example, they enable single molecule SERS at an extremely high enhancement level using non-resonant near infrared excitation.[23] The interesting observation here is that discontinuous aluminum films also provide hot spots in the near infrared range. This might support the hypothesis that field confinement is controlled by the geometry of the nanostructure and not by the nature of the metal or the dielectric constant of the embedding medium.[24]

Plasmonic nanostructures and plasmon resonances can also be probed by electron energy loss spectroscopy (EELS).[25,26] Compared to optical methods, EELS can provide three orders of magnitude better spatial resolution. Experimental evidence of the nanometer-scale confinement of plasmonic eigenmodes in random silver films has been recently provided by EELS.[27] EELS studies on aluminum nanoparticles performed 30 years ago have identified plasmon resonances of small isolated Al spheres at 6.7 eV and red shifted plasmon resonances at around 4 eV for coupled spheres.[28] Here we probe the discontinuous Al films using EELS.

The EELS data were acquired using an FEI Titan instrument operating at 120 kV, having a subnanometer spatial resolution and better than 0.2 eV energy resolution.[29] Fig. 3 shows the nanostructured Al film along with a typical EELS spectrum. In addition to a strong peak at 15 eV related to bulk plasmons in aluminum, EELS spectra show resonances in the 1.3–2.5 eV range, *i.e.* in the excitation range in which the strong SERS signals have been obtained (compare Fig. 2). This correlation between plasmon resonances and the excitation wavelength of SERS strongly supports the electromagnetic origin of the strong SERS effect on discontinuous Al-films. In agreement with the structure of the film shown in the STEM image that lacks indications of isolated nanoparticles, we have not observed resonances at around 6.7 eV corresponding to surface plasmons of isolated small Al nanoparticles.[28] More studies are under way

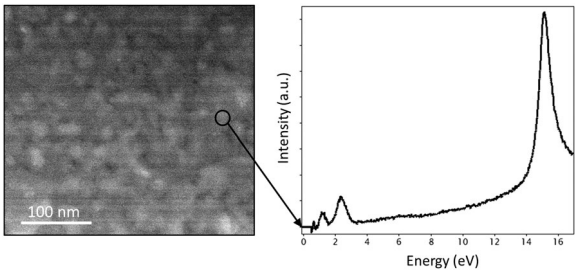

Fig. 3 Scanning transmission electron micrograph of the aluminum film and electron energy loss spectrum collected from the region marked in the image.

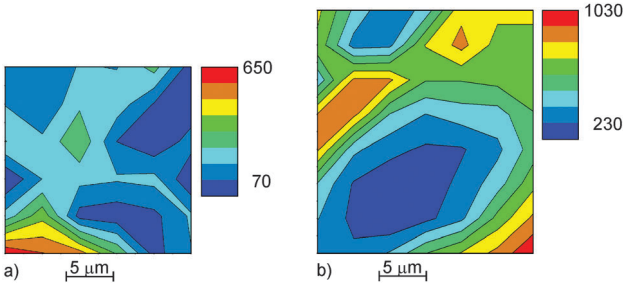

Fig. 4 Distribution of the SERS signal (arbitrary units) on the Al film collected with a spot size of 1 μm^2 using 785 nm excitation. Images are based on the SERS signal of the 730 cm^{-1} line of adenine (a) and the 1080 cm^{-1} line of pMBA (b). The images were obtained by raster scanning a $\sim$1 μm^2 spot over a larger area.

to correlate and interpret EELS data and morphology of discontinuous metal films.

Considering the large area from which the signal is collected in an optical experiment, statistically, the area on the nanostructured Al film used for collecting a SERS spectrum should support almost all possible plasmonic eigenmodes of the film. However, only excitation in the near infrared region results in strong SERS enhancement, which means that only molecules in the hottest spots related to NIR excitation essentially contribute to the SERS signal.

Fig. 4 displays typical images of SERS signals of two probe molecules collected by scanning a $\sim$1 μm^2 spot over a larger area using 785 nm excitation. Differences in signals are less than a factor of ten, indicating a relatively uniform mean SERS enhancement, *i.e.* about the same number of hottest spots related to 785 nm excitation in each $\sim$1 μm^2 sampled spot.

In conclusion, we have demonstrated strong SERS on discontinuous aluminum films using NIR excitation. EELS measurements identify plasmon modes in the visible and near infrared range for these Al structures. So far, the metal was considered as a material which supports SERS at UV excitation. Our experimental results suggest the use of aluminum nanostructures for plasmon supported spectroscopy and photonics beyond the UV range.

The A. P. Møller and Chastine Mc-Kinney Møller Foundation are gratefully acknowledged for their contribution towards the establishment of the Centre for Electron Nanoscopy in the Technical University of Denmark. Financial support from ERC Grant no. 259432 (J.K., M.G.) is gratefully acknowledged.

Notes and references

1 K. Kneipp, *Phys. Today*, 2007, **60**, 40–46.
2 M. I. Stockman, *Opt. Express*, 2011, **19**, 22029–22106.
3 N. J. Halas, S. Lal, W. S. Chang, S. Link and P. Nordlander, *Chem. Rev.*, 2011, **111**, 3913–3961.
4 P. R. West, S. Ishii, G. V. Naik, N. K. Emani, V. M. Shalaev and A. Boltasseva, *Laser Photonics Rev.*, 2010, **4**, 795–808.
5 J. M. McMahon, G. C. Schatz and S. K. Gray, *Phys. Chem. Chem. Phys.*, 2013, **15**, 5415–5423.
6 T. Dorfer, M. Schmitt and J. Popp, *J. Raman Spectrosc.*, 2007, **38**, 1379–1382.
7 A. Taguchi, N. Hayazawa, K. Furusawa, H. Ishitobi and S. Kawata, *J. Raman Spectrosc.*, 2009, **40**, 1324–1330.
8 L. Li, S. F. Lim, A. A. Puretzky, R. Riehn and H. D. Hallen, *Appl. Phys. Lett.*, 2012, **101**, 4.
9 S. K. Jha, Z. Ahmed, M. Agio, Y. Ekinci and J. F. Loffler, *J. Am. Chem. Soc.*, 2012, **134**, 1966–1969.
10 D. O. Sigle, E. Perkins, J. J. Baumberg and S. Mahajan, *J. Phys. Chem. Lett.*, 2013, **4**, 1449–1452.
11 G. H. Chan, J. Zhao, G. C. Schatz and R. P. Van Duyne, *J. Phys. Chem. C*, 2008, **112**, 13958–13963.
12 Y. Ekinci, H. H. Solak and J. F. Loffler, *J. Appl. Phys.*, 2008, **104**, 6.
13 M. Schwind, B. Kasemo and I. Zoric, *Nano Lett.*, 2013, **13**, 1743–1750.
14 M. W. Knight, L. F. Liu, Y. M. Wang, L. Brown, S. Mukherjee, N. S. King, H. O. Everitt, P. Nordlander and N. J. Halas, *Nano Lett.*, 2012, **12**, 6000–6004.
15 P. M. Schwab, C. Moosmann, M. D. Wissert, E. W. G. Schmidt, K. S. Ilin, M. Siegel, U. Lemmer and H. J. Eisler, *Nano Lett.*, 2013, **13**, 1535–1540.
16 M. W. Knight, N. S. King, L. F. Liu, H. O. Everitt, P. Nordlander and N. J. Halas, *ACS Nano*, 2014, **8**, 834–840.
17 J. Martin, J. Proust, D. Gerard and J. Plain, *Opt. Mater. Express*, 2013, **3**, 6.
18 W. H. Park and Z. H. Kim, *Nano Lett.*, 2010, **10**, 4040–4048.
19 V. A. Markel, L. S. Muratov, M. I. Stockman, V. M. Shalaev and T. F. George, *Phys. Rev. B: Condens. Matter Mater. Phys.*, 1991, **43**, 8183.
20 M. I. Stockman, V. M. Shalaev, M. Moskovits, R. Botet and T. F. George, *Phys. Rev. B: Condens. Matter Mater. Phys.*, 1992, **46**, 2821–2830.
21 M. I. Stockman, S. V. Faleev and D. J. Bergman, *Phys. Rev. Lett.*, 2001, **87**, 167401.
22 K. Seal, D. A. Genov, A. K. Sarychev, H. Noh, V. M. Shalaev, Z. C. Ying, X. Zhang and H. Cao, *Phys. Rev. Lett.*, 2006, **97**, 206103.
23 K. Kneipp, Y. Wang, H. Kneipp, L. T. Perelman, I. Itzkan, R. R. Dasari and M. S. Feld, *Phys. Rev. Lett.*, 1997, **78**, 1667.
24 M. Essone Mezeme and C. Brosseau, *Opt. Express*, 2012, **20**, 17591–17599.
25 J. Nelayah, M. Kociak, O. Stephan, F. J. G. de Abajo, M. Tence, L. Henrard, D. Taverna, I. Pastoriza-Santos, L. M. Liz-Marzan and C. Colliex, *Nat. Phys.*, 2007, **3**, 348–353.
26 F. J. G. de Abajo, *Rev. Mod. Phys.*, 2012, **82**, 209.
27 A. Losquin, S. Camelio, D. Rossouw, M. Besbes, F. Pailloux, D. Babonneau, G. A. Botton, J. J. Greffet, O. Stephan and M. Kociak, *Phys. Rev. B: Condens. Matter Mater. Phys.*, 2013, **88**, 7.
28 P. E. Batson, *Ultramicroscopy*, 1982, **9**, 277–282.
29 S. Kadkhodazadeh, J. B. Wagner, H. Kneipp and K. Kneipp, *Appl. Phys. Lett.*, 2013, **103**, 083103.

end of paper

Chapter 4

Raman and SERS in plants

Throughout this project, Raman and Surface Enhanced Raman Spectroscopy were performed in several plant species as a biosensor tool, aiming to investigate physical and physiological parameters inside the plants such as chemical compounds. A major portion of the performed experiments were not presented in the published paper of *Raman spectroscopic probing of plant material using SERS*. However, they were fundamental to disseminating new protocols and generating ideas for the later published experiments based on the performance of SERS in Onions (section 4.4.1.). Therefore, this chapter is based on the design of different protocols to prepare Raman and SERS samples i.e. how to bring silver nanoparticles inside plant tissues as well as how to assign chemical compounds to Raman signatures.

4.1 Introduction

As mentioned in the motivation (Section 1.1), plants contribute the majority of living being on Earth. It is, therefore, essential to optimize the use of plants by investigating their functionality and properties. The functionality of a plant not only depends on its constituents but also on their distribution at the micro and nano-scale. Very often, the study of the chemical composition of biological material are carried out by chemical procedures[6] which are time consuming and require the disintegration of the materials[79,80]. Moreover, the techniques present limitations, such as the identification of compounds is not always complete and detection of functional groups after a depolymerization is limited.

Also, as previously mentioned in this thesis, Raman spectroscopy can provide a fingerprint of specific molecules in a sample in a way that individual bands in a Raman spectrum can be correlated with specific molecular vibrations[36]. Moreover, it does not require any destructive protocols and can be applied in fresh plants[81,10,82,83]. Therefore, this technique is a great alternative for sensing biological systems. In this context, Raman spectroscopy

studies on plants has developed great interest during the past years[81,83,84,35,85–89]. Already in the 1980s, Raman spectroscopy was performed to investigate the cell wall components in woody tissues[90,91]. Furthermore, essential oil substances of several Basil chemotypes were identified and quantified via various vibrational spectroscopy methods[84]. Moreover, Raman spectroscopy has been also used for the investigation of Triterpenoids (secondary metabolities) in plant cuticle membranes[92], for the detection of polycetylenes in Apiaceae fresh vegetables[83] and in general for the study of the primary and secondary metabolities in the cell wall of plants including carbohydrates, lignin, proteins, lipids and phenolic groups among others[82,35,10,93].

The performance of Raman spectroscopy in plants can be challenging due to the presence of natural fluorescence signals which typically are several orders of magnitude higher than the Raman signals[73]. In this context, SERS has shown the capability to enhance Raman signals from tracked constituents at very low concentrations (and even down to one unique molecule)[94–96], and therefore has developed great interest in applications for studying biological samples[97–103]. For example, different Raman signatures associated with pigment molecules present in plants have been identified via SERS[98,101,102]. In these studies, the preparation of the biological samples required different procedures to extract the dye, i.e. boiling, crushing or mixing the tissue with other chemicals. Recently, SERS has been used to analyze genomic DNA from in vitro grown plant species such as apples and tomatoes[100,104,105]. Also in these studies, DNA was extracted via different chemical protocols from in vitro leaves, without keeping them intact. There have been several studies where SERS has been used to detect pesticides from the surface of intact fruits and vegetables[106–108]. In these studies, gold nanoparticles were adhered, together with different insecticides, to the surface of the samples proving the capability of the technique to discriminate them *in-situ*. In addition, SERS has been used to investigate *in-vivo* vegetables, such as Lamiaceae plants, were sections of stalks of the plants were merged into silver soil[97]. An interesting nondestructive protocol for introducing metal nanoparticles into living plant leaves has been also designed[99]. SERS tags made of 4-MBA labeled Au-Ag-Shell nanoparticles were injected non-invasively into tobacco leaves, showing for the first time a strategy for delivering nanoparticles into the leaf tissues.

In particular, the influence of metallic silver nanostructures, its level of toxicity in fresh plants at low concentrations and its effects on features in SERS is not well known[119,120]. For that reason, during the recent years, numerous studies are being carried out on green synthesis of metal nanoparticles with plant tissues, where the general toxicity can be lowered by using biological molecules as reducing agents of the nanoparticles (a more detailed description is available in Chapter 3).

SERS studies into intact leaves plants where silver nanoparticles are synthesized naturally

in the epidermis of the leaves, i.e. green synthesis, are rare in the literature. In the following experiments, described in section 4.2., 4.3. and 4.4., different approaches are compared for delivering plasmonic silver nanostructures in three common plant leaves. SERS sensors with silver nanoaggregates are used as building blocks. As a first approach, silver nanoparticles are naturally synthesized by the plant extract inside the tissue of an intact Aloe Vera leaf via injecting $AgNO_3$. As a second approach, silver nanoparticles prepared by the standard chemical procedure[58], are directly delivered into the extracellular spaces of celery and basil leaves. The results suggested that the delivery of silver nanoparticles into different parts of the tissue is probably favored by the presence of stomata at the surface of the leaves, which facilitate their transport[99]. The plasmonic structures in the epidermis of the tissues provided modest to high electromagnetic fields depending on the leaf used, enabling to collect enhanced Raman signatures from chemical compounds present at the extracellular space of the leaves.

For these experiments, Aloe Vera, basil and celery were used. Aloe Vera has received high interest due to its numerous benefits used for medicinal, cosmetic and nutritional applications[109,110]. Moreover, it has shown the capability of synthesizing silver and gold nanoparticles, using the extract of Aloe Vera as a reducing agent[112,113]. Familiarly, other plant species, such as basil and celery have also been shown to contain beneficial compounds. Celery is a vegetable that contains highly amount of Flavonols[114], which are beneficial for their natural antioxidants[115]. Basil is constituted of several essential oils which have also been shown to be beneficial not only from nutritional aspect but also for cosmetics and medicines[111]. It is, therefore, of high interest to investigate their chemical constituents which are responsible for their natural benefits. In our experiments, these three plants were chosen not only for the general interest on their valuable compounds, but also for practical reasons of availability and accessibility. Moreover, celery and basil plants are very convenient for performing Raman since they are composed of thin leaves, thus preventing the total absorption of the scattered Raman light[86].

4.2 Raman and SERS performed in leaves

In order to perform the following experiments, silver nanoparticles were prepared by the standard chemical procedure via reduction of 10^{-3}M $AgNO_3$ with sodium citrate (see Chapter 2)[58], where 0.35 M of NaCl was added to the colloids in a 1 : 10 ratios in order to induce aggregations. As a result, spherical isolated nanoparticles as well as small aggregations of $10 - 100$ nm size gave rise to an absorbance band at around 420 nm together with an increase of the band signal in the red region of frequencies; the nanoparticles being in resonance with the excitation laser light in the near-infrared and therefore optimum for SERS

experiments. Characterization of the nanoparticles via extinction coefficient and scanning electron microscopy has been shown in our previous work[103].

For the preparation of the three biological samples, each leaf was cut from the stem, washed with water and dried at room temperature. For the delivery of silver nanoparticles into the three species, two different approaches (inspired by the works of A. Shen[99]) were carried out:

Approach 1: A leaf of Aloe Vera was cut off from the plant, flushed with water and exposed to dry at room temperature. Once it dried, $AgNO_3$ was injected into the leaf from the surface, using 2 ml syringe with a 24 G, 0.55x25 mm needle. The leaf was again flushed with water and kept in darkness for at least 24 hours. Raman measurements were taken directly from the surface of the leaf.

Approach 2 (applied in Celery and Basil): A 2 ml syringe tip was positioned against the lower surface of the leaf. Colloidal silver nanoparticles were delivered inside the surface layer of the leaf by applying small pressure with the fingers so as to avoid any damages in the tissue. Thus, to create small negative pressure the syringe was pulled opposite to the tip, while it adhered to the surface of the leaf. Afterward, the syringe was pushed very gently. In this way, a small pressure was applied to assist the leaf in absorbing the nanoparticles.

In order to analyze the Raman spectra, as well as to assign chemical compounds to the signatures of the chosen plants, it is necessary to consider the most expected compounds that are typically present on the plants. All plants are composed of a lipid membrane called cuticle, covering the epidermal cells of the leaves[93]. The plant cuticle is composed of a rich fraction of cutin and contains high amount of phenolic groups such as flavonols and soluble waxes such as alcohols, fatty acids and esters among others. Moreover, within the cuticle (at the primary cell wall), there is a rich region of carbohydrates such as hemicellulose, cellulose and pectin. In adition, proteins such as Amide I, II, III are also very important in plants as primary metabolities but the amount of cellulose is often much higher, and therefore these signals much weaker[86]. Also, often cellulose and pectin appear within the same frequency region of a Raman spectrum, therefore it is often difficult to distinguish them.

All the experiments were carried out by using the customized Raman setup described in Chapter 2.

4.2.1 Aloe Vera

Figure 4.1a shows the Raman spectrum of the Aloe Vera leaf collected in 20 seconds. The Raman spectrum show signatures at ca. 1150 cm^{-1}, 1185 cm^{-1}, 1440 cm^{-1} and 1520 cm^{-1}. These could tentatively be assigned to the bending mode of CH and the stretching vibration

of $C = C$ associated with the presence of peridinin and diadinoxathinand[116,117], which are responsible for the yellow pigments of the leaf. It has been shown that the accumulation of diadinoxathin occurs as a photo-protective effect of the leaf being exposed to stress, e.g. by high irradiation[121]. However, there was no appearance of changes in the color of the leaf, nor signs of disintegration after performing the measurements, suggesting that the leaf was under stress as a result of removal from the stem of the plant. In addition, Raman signatures are quite broad and therefore might have contributions from other chemical compounds in the tissue. For example, comparing the measured Raman lines with the observed in the review of J. Heredia[93], Raman signatures at ca. 1150 cm^{-1}, 1220 cm^{-1} and 1320 cm^{-1} could also tentatively be assigned to the asymmetric stretching vibration of C-O-C, bending mode of OH and bending mode of CH_2 respectively, of cuticle compounds typically located at the epidermis of the leaf[93]. In the same way, the Raman signatures at ca. 1440 cm^{-1} and 1520 cm^{-1} could be assigned to aromatic stretching vibration of C=C due to the presence of phenolic compounds at the plant cuticle. Notice that the thickness of Aloe Vera leaves is around 15-20 μm[118] and the laser spot area is around 1 μm^2, therefore the chemical information obtained when performing Raman on the surface of the plant leaf is probably coming from those compounds located at the epidermis of the leaf.

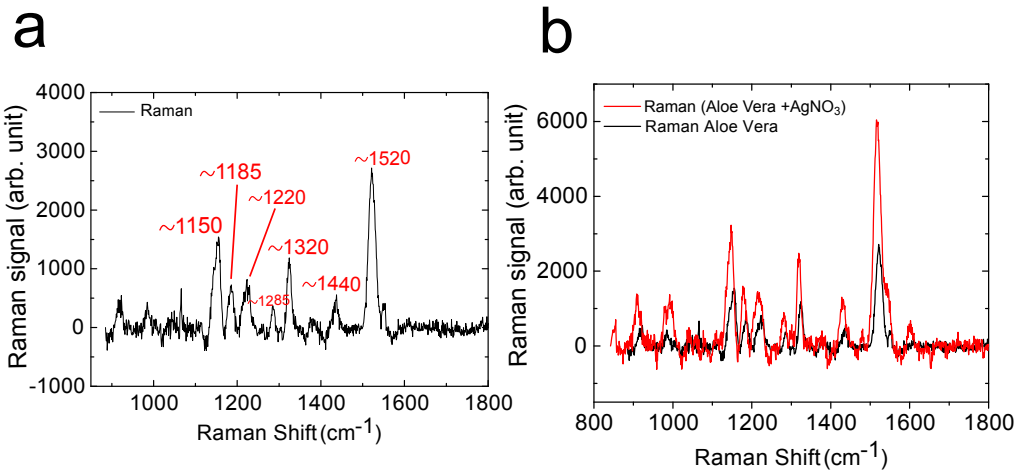

Figure 4.1: (a) Raman spectrum collected from an Aloe Vera leaf. b) Raman spectrum collected from the epidermis layer of the Aloe Vera leaf after incubation of $AgNO_3$ inside the fresh leaf via injection of silver salt into the tissue. Both spectra collected in 20 seconds using 2 mW 785 nm excitation.

Figure 4.1b shows the Raman spectrum of the leaf of Aloe Vera, also measured from the surface, after 72 hours of incubation time of $AgNO_3$ (see protocol above). The spectrum shows very modest or almost non enhancement of the Raman signatures at ca. 905 cm^{-1}, 995 cm^{-1}, 1150 cm^{-1}, 1185 cm^{-1}, 1220 cm^{-1}, 1285 cm^{-1}, 1320 cm^{-1}, 1440 cm^{-1} and 1520

cm^{-1}. Enhancements factors of 2-3, compared to spectrum shown in Figure 4.1a, are too low for being calling SERS, therefore these results can not guarantee the formation of the silver nanoparticles inside the tissue. In addition, a new signature appears in the spectrum at 1600 cm^{-1} which might be assigned to the aromatic stretching vibration $C-C$ of phenolic compounds[93]. The low enhancement of the Raman signatures together with the appearance of a new signature cannot guarantee an enhancement due to the presence of nanoparticles; it can be attributed to better conditions in a particular spot in the sample, leading to increase the signal to noise ratio, i.e. related with the presence of higher number of molecules at a particular spot of the leaf.

Notice that sizes of the silver nanoparticles are many orders of magnitude smaller than the sizes of the stomata; therefore, when applying small pressures to inject the nanoparticles inside the leaf tissue, nanoparticles might pass through the stomata to the extracellular space[99].

4.2.2 Celery

However, the cuticle layer thickness of Aloe Vera leaves is very thick and probably hinders the uptake of nanoparticles through the stomata to the extracellular space of the leaves. In contrast, basil and celery are composed of very thin leaves, and in this case stomata could assist silver nanoparticles to pass through the cuticle to the extracellular space of the tissues. Figure 4.2a displays the Raman spectrum taken from the surface of a fresh celery leaf. As can be seen, the Raman spectrum show similar Raman signatures compared to Aloe Vera (Figure 4.1). Thus, signatures at ca. 1150 cm^{-1}, 1185 cm^{-1}, 1440 cm^{-1} and 1520 cm^{-1} could probably be assigned to the presence of peridinin and diadinoxathinand as well contributions from phenolic groups and cuticle compounds[116,117]. In addition, Figure 4.2b shows the Raman spectrum taken from the surface of the leaf after injecting silver nanoparticles following the Approach 2 described before. The spectrum of celery again shows very modest or almost non enhancement of the peaks at ca. 905 cm^{-1}, 995 cm^{-1}, 1150 cm^{-1}, 1185 cm^{-1}, 1220 cm^{-1}, 1285 cm^{-1}, 1320 cm^{-1}, 1440 cm^{-1} and 1520 cm^{-1} compared to the Raman spectrum in Figure 4.2a. Also, the aromatic stretching vibration $C-C$ due to the phenolic compounds could be a possible signature that appears in the spectrum at 1600 cm^{-1} [93]. As can be seen, spectra of Aloe Vera (Figure 4.1) and the spectra of celery show similar signatures, suggesting that the compounds present in both parts of the plant leaves are common primary metabolites, found in all plants and necessary for the existence of plants.

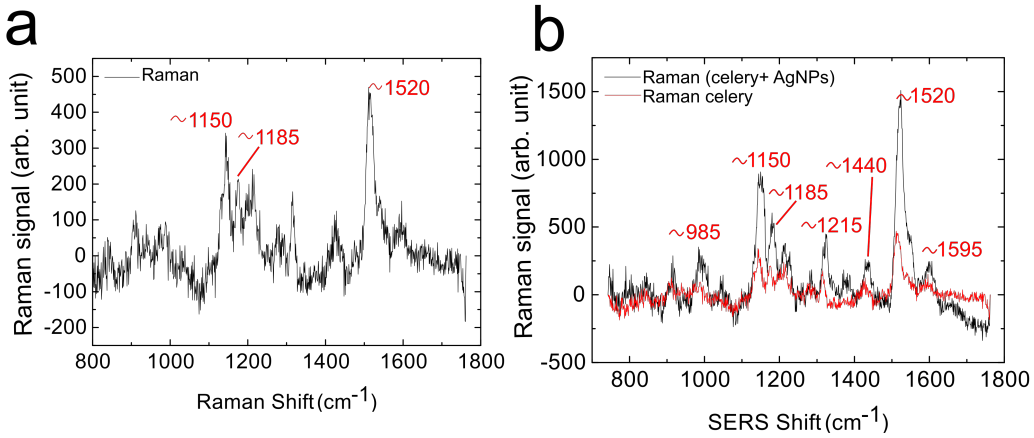

Figure 4.2: Raman spectrum collected from the surface of a celery leaf. a) Raman spectrum b) Raman spectrum measured from the surface of the leaf after delivering silver nanoparticles into the fresh tissue. Both spectra collected in 1 second using 2 mW 785 nm excitation.

4.2.3 Basil

Figure 4.3a shows the Raman spectrum measured from the surface of a basil leaf. Similarly to the Raman spectra of Aloe Vera and celery, the spectrum shows Raman signatures at ca. 1150 cm^{-1}, 1185 cm^{-1}, 1220 cm^{-1} and 1520 cm^{-1} tentatively assigned to molecular vibrations of peridinin and diadinoxathinand as well as phenolic groups and cuticle compounds. In addition, the SERS spectrum in Figure 4.3b shows an enhancement of these Raman signatures by more than one order of magnitude. This enhancement factor is higher compared to Aloe Vera and Celery SERS spectra (Figures 4.1 and 4.2), suggesting that the location of the silver nanoparticles in the extracellular space of the basil leaf is either more homogeneous, i.e. molecules of the leaf are in closer contact with the nanoparticles; or there is a higher concentration of nanoparticles inside, providing numerous hot spots.

It is well known that the sizes and number of stomata vary with each plant. Figure 4.4 shows a microscopy image of the top of the basil and celery leaves used during these experiments, after measuring the Raman spectra of the two leaves. Raman measurements and the injection of the silver nanoparticles were carried out on the top surface of the leaves where the basil stomata (around 30 μm) are bigger than the celery stomata (around 20 μm). This difference in sizes could provide an explanation towards why higher amounts of silver nanoparticles reach the extracellular space in basil leaves. In addition, the SERS spectrum of basil shows new Raman signatures at ca. 995 cm^{-1}, 1100 cm^{-1}, 1130 cm^{-1}, 1320 cm^{-1}, 1375 cm^{-1}, 1430 cm^{-1} which could tentatively be assigned to the presence of essential oils typically found in basil[84]. Thus, signatures 1100 cm^{-1} and 1320 cm^{-1} could be assigned to the $C-O-C$ vibration of esters groups in the oil, 995 cm^{-1} and 1130 cm^{-1} could be associated with

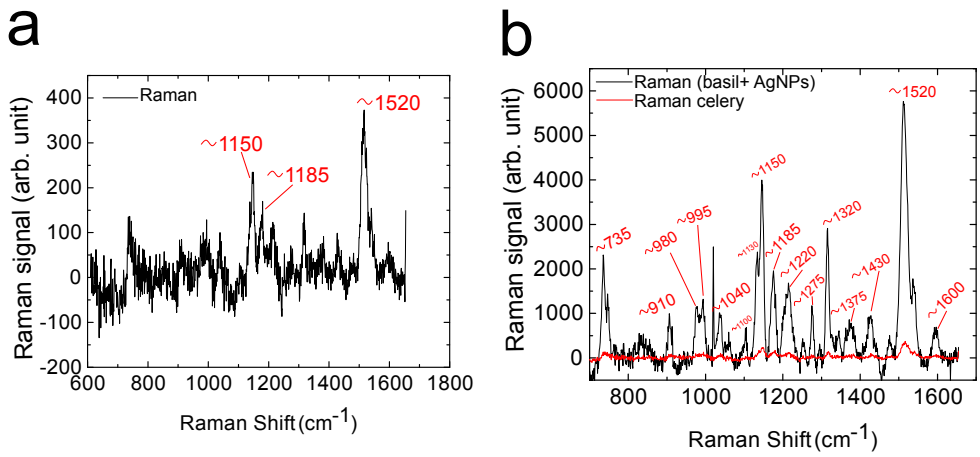

Figure 4.3: Raman spectrum collected from the surface of a basil leaf. a) Raman spectrum b) Raman spectrum measured from the surface of the leaf after delivering silver nanoparticles into the fresh tissue. Both spectra collected in 1 second using 2 mW 785 nm excitation.

the stretching benzene ring and 1375 cm^{-1} and 1430 cm^{-1} assigned to CH_2 deformation modes[84,35]. In addition, 735 cm^{-1} might be associated with the bending mode of CH_2 due to the presence of cutin (cuticle component)[93]. Also a new signature appears in the spectrum at ca. 1550 cm^{-1} and 1600 cm^{-1} which could probably be assigned to the aromatic stretching vibration $C-C$ of phenolic compounds[93].

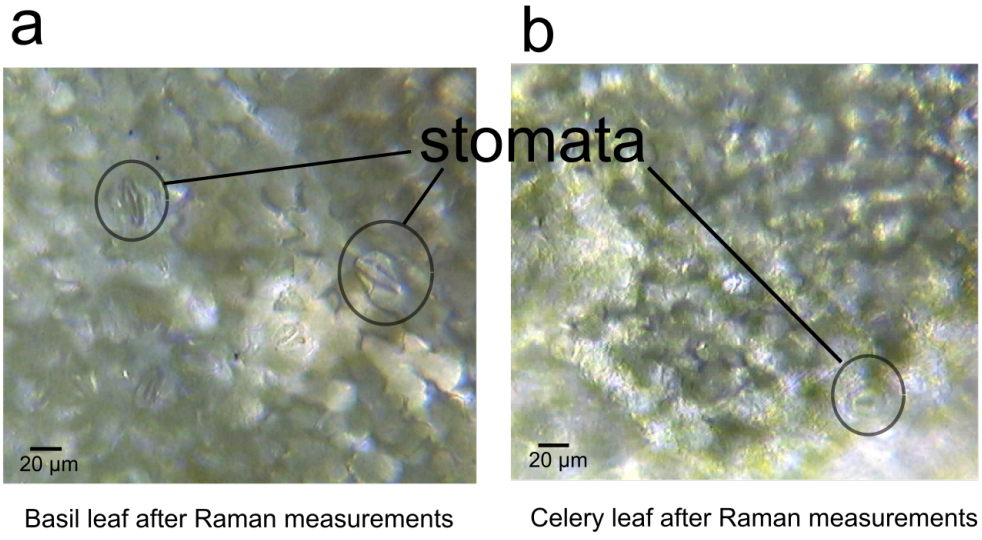

Figure 4.4: Microscope image taken from a basil and celery leaf after measurement of Raman spectra. (a) Image of the surface of a basil leaf showing the presence of stomata with around 30 μm diameter. (b) Image of the surface of a celery leaf showing the presence of stomata with around 20 μm diameter.

4.3 Inside from initial studies from plant leaves

In this work, SERS studies to chemically probe fresh Aloe vera, celery and basil leaves via delivering silver nanosensors into the tissues were performed. The difference between the thicknesses of the epidermis layers of the three chosen plants allowed chemically sensing different parts of the leaves, i.e. epidermis and extracellular space, by delivering silver plasmonic building blocks into the different part of the tissues. Two different approaches were used to deliver these nanosensors into the plant: $AgNO_3$ was directly injected into the epidermis of the Aloe Vera leaf, and silver nanoparticles were injected directly into celery and basil leaves. Only in case of basil, SERS spectrum gave rise to strong enhanced Raman signals suggesting the location of the silver nanostructures inside the different parts of tissue. The Raman signals indicated the presence of common compounds in the three species (tentatively polyenic compounds located at the tissues) as well as the presence of specific essential oils located at the extracellular space of the Basil and celery leaf. In addition, SERS spectra collected from the basil leaves showed higher Raman enhancement (around one order of magnitude) compared with Aloe Vera and celery leaves; probably influenced by the bigger size of the stomata at the basil leaf which facilitated higher transport of nanoparticles into the epidermis.

After performing the experiments, the leaves did not show apparent change of color nor necrosis of the tissues.

4.4 Allium cepa

In a very simplified approach an optical nanosensor, can be though of as a tiny element which is able to detect chemical or physical parameters on a sample via interactions of electromagnetic waves. To build a nanosensor, it is convenient to use a sensitive reporter molecule which can generate optical signals as a response. Thus, the emitted optical signal needs to be strongly dependent on its surrounding location, allowing to sense different properties in a specific environment. In this way, a SERS-sensor comprised of metal nanostructures could provide specific molecular information of any sample based on the Raman signature of a reporter molecule attached to the nanoparticles. A pH−SERS sensor consisting of a molecule called para mercapto benzoic acid (pMBA), attached to gold or silver plasmonic nanostructures has already been introduce[122,123]. This molecule is suitable for pH measurements due to the fact that its Raman spectrum varies with the pH environment where is located, thus acting as a pH-meter.

In the following paper,[103], section 4.4.1., SERS was performed in Onion cell layers by delivering SERS nanosensors into the extracellular space of the tissue. The SERS nanosensors

consisted of pMBA molecules attached to plasmonic nanostructures, thus providing information of the chemical compounds and pH value of the extracellular space of the onion cell. Raman images originated from specific Raman signatures associated with onion compounds and the pMBA molecule, allowed to visualize the location of both, the nanoparticles and the reporter molecule, in the extracellular space of the onion. Additionally, the use of Ag island films as SERS substrates allowed us to study the intact cell layer, showing the chemical complexity of the tissue.

4.4.1 Espina Palanco, Marta; Mogensen, Klaus Bo; Kneipp, Katrin. J. Raman Spectrosc 2015, 47, 156–161

beginning of paper

Research article

Journal of RAMAN SPECTROSCOPY

Received: 9 April 2015 Revised: 19 June 2015 Accepted: 20 July 2015 Published online in Wiley Online Library

(wileyonlinelibrary.com) DOI 10.1002/jrs.4768

Raman spectroscopic probing of plant material using SERS

Marta Espina Palanco,[a] Klaus Bo Mogensen[b] and Katrin Kneipp[a]*

We report surface-enhanced Raman studies on intact plant material using onion layers as a biological target, and silver nanoaggregates and silver island films as enhancing plasmonic structures. Surface-enhanced Raman scattering (SERS) enhancement allows the detection of strong Raman signatures of chemical constituents of the surface of the onion layer such as cellulose, proteins, and flavonols. Because of long-time incubation, SERS sensors can access the extracellular space in the inner of the layer. The location of silver nanoparticles inside the onion layer has been monitored by the SERS images collected from chemicals present in the onion and/or reporter molecules attached to the nanoparticles. Our studies show a competitive adsorption of intrinsic bio molecules of the onion layer and reporter molecules. Different spectra from different places of the layer indicate the complex heterogeneous chemical structure of the plant material. The pH-sensitive reporter molecule para mercapto benzoic acid attached to the nanoparticles allows us to infer pH values inside the extracellular matrix of the onion layer. Copyright © 2015 John Wiley & Sons, Ltd.

Keywords: surface-enhanced Raman spectroscopy; silver nanoparticles; silver island films; plant material; onion; pH sensor

Introduction

There is a strong interest in exploring and developing new methodologies in order to study complex biological structures such as plants.[1–3] The chemical composition of plants can be investigated by using 'classical' biochemical and biophysical methods.[4,5] However, these methods are destructive techniques and, in many cases, do not allow a correlation between identified chemicals and their location inside a plant structure.

Raman spectroscopy provides a direct non-invasive access to the molecular structure and allows us to study the chemical composition of plants.[6] Usually, Raman spectroscopy does not require any sophisticated sample preparation and can provide rapid *in vivo* probing in both fresh and processed plant materials. Excitation wavelengths in the near infrared (NIR) range avoid a strong fluorescence background, which usually exists in Raman spectra of plants and which is related to many biological fluorophores present in the excitation volume of the plant. Combination of Raman scattering and microscopy enables Raman imaging and, by this way, an assignment of a chemical to its location in the structure of a plant. Typical spatial resolution of about 1 μm is well suited to probe the chemistry of plants in their different compartments, such as cell wall, cytoplasm, and cell membrane. However, a drawback in Raman studies is the extremely small cross section of the inelastic scattering process, which results in relatively weak signals.

Surface-enhanced Raman scattering can overcome this low-signal problem of Raman spectroscopy.[7] Resonances between optical fields and the collective oscillations of the conduction electrons in nanometer-sized metal structures, so-called surface plasmons, produce high fields in nanometer-scaled small volumes in the vicinity of metal nanostructures. Most popular enhancing plasmonic structures are made from gold and silver in size ranges between 10 and 100 nm. Performing Raman spectroscopy in the enhanced local fields in close proximity of these metal nanostructures results in the enhancement of the Raman signal by many orders of magnitude. SERS combines the structural selectivity of Raman spectroscopy with detection sensitivity comparable or even better than fluorescence. The method has a great potential for probing and sensing also biological objects and materials[8] and should also be very useful for studying plants.[9–14] Different approaches have been presented in the literature in order to exploit SERS for studying plants. Already in 1985, spinach chloroplasts were used for SERS studies of a plant membrane system. Photosystem II membranes, i.e. structures that are composed of a protein complex, which is involved in the first reaction of the photosynthesis process, were chemically extracted from spinach.[9] Enhanced Raman signals were measured because of contact of the extracted aqueous sample solution with a rough silver electrode. In other studies, metal plasmonic nanostructures have been used for SERS experiments on plants.[10–14] Such structures, sometimes with an attached reporter molecule for SERS studies, were delivered into plants by injection or up take and have been imaged in roots, stems, and leafs based on the Raman signature of the reporter. A more recent paper reported SERS studies of DNA of several plant species using silver nanoparticles[13] suggesting the capability of SERS to analyze genetic connections among plants.

In our study, we apply SERS to measure and image vibrational signatures of intrinsic biological molecules of plants. We also

* *Correspondence to: Katrin Kneipp, Department of Physics, Danmarks Tekniske Universitet DTU, Lyngby, Denmark.*
E-mail: kneipp@usa.net

a *Department of Physics, Danmarks Tekniske Universitet DTU, 2800 Kgs. Lyngby, Denmark*

b *Department of Micro- and Nanotechnology, Danmarks Tekniske Universitet DTU, 2800 Kgs. Lyngby, Denmark*

explore the simultaneous use of SERS sensors to measure pH values inside plant material.

We use layers of onion as a plant target and explore different approaches to apply plasmonic active silver nanostructures to plant material. Onions are a good candidate for these studies because to extract cell layers from an onion is very feasible, allowing them to be analyzed in its natural state. In the first type of experiments, we use SERS sensors with silver nanoaggregates as basic building blocks.[15] These plasmonic structures provide high local fields and enable to collect Raman spectra from molecules present in their biological environment. Moreover, SERS sensors can be identified and imaged based on the Raman signature of an attached reporter molecule. In case the reporter has a pH-sensitive Raman spectrum, the SERS sensor also acts as local pH meter for the biological structure. SERS nanosensors can be placed on top of the onion layer delivering information on the surface of the layer. During long-time incubation, nanosensors can pass the wall and enable SERS measurements inside the onion layer. In a second type of experiments, enhanced Raman spectra have been measured from onion layers attached to silver island films.

Experimental

Silver nanoparticles were prepared by the standard chemical procedure via reduction of 10^{-3} M $AgNO_3$ by sodium citrate.[16] A 0.35 M NaCl was added to the colloidal solution in 1 : 10 ratios to achieve optimum SERS conditions.[17–19]

Silver island films were produced by Ag evaporation at controlled pressure of 2×10^{-6} mbar. The nominal deposited thickness was 10 nm. The nano-island formation took place during annealing in forming gas for 10 min at 400 °C in an in-house built reactor.[20,21] The silver nanostructures were characterized by their optical extinction spectra and scanning electron microscopy (SEM) images.

To build a SERS pH sensor, para mercapto benzoic acid (pMBA) as a pH-sensitive reporter molecule has been attached to silver nanoaggregates.[22–24] An aqueous solution of 10^{-4} M pMBA was mixed with 0.35 M NaCl and aqueous solution of silver nanoparticles prepared in the reduction process described previously in 1 : 1 : 10 ratios, respectively. A calibration curve for this pH sensor has been established by SERS measurements from this solution of nanoparticles with attached pMBA at various pH values.

For the preparation of the biological target, a rectangular piece of onion was cut from its surface. This slice of onion contains several cell layers. One of the layers was peeled with tweezers and deposited onto a square transparent hydrolytic class 1 glass (15 × 15 mm) ready for Raman measurements.

Three different ways to bring the silver nanostructures in contact with the plant material have been explored:

Protocol 1: 50 µl drop of the solution of the SERS sensor was placed on the top of the onion cell layer, covering the whole target. Once the drop was completely dry, the sample was ready for Raman measurements. This approach enabled to measure Raman spectra from the surface of the onion cell layer.

Protocol 2: An onion layer was deposited over an AgNPs film. Once the sample dried, it was ready for surface-enhanced Raman measurements from the surface of the onion layer.

Protocol 3: An onion cell layer was immersed in the aqueous solution of the SERS sensor by varying the incubation time between 10 min and 20 h. Following incubation, each sample was flushed with tap water in order to remove silver nanoparticles from the surface of the layer. This enables to measure Raman signals originating from inside the onion layer without contribution from the surface of the layer.

Surface-enhanced Raman scattering spectra were measured by a customized Raman setup using 2 mW 785 nm diode laser excitation focused to a spot of ~1 μm^2.[25] Typical collection time for a spectrum was 1 s. Placing the sample on a moving stage allows to scan over the sample and to create Raman images at micrometer resolution.

Results and discussion

Figure 1a shows typical electron microscope images and extinction spectra of chemically prepared silver nanoparticles and small aggregates used in the reported SERS experiments. SEM images identify silver structures at sizes between 30 and 120 nm consisting of isolated almost spherical particles and small aggregates of a few particles. The applied NaCl concentrations on the order of 10^{-2} M do not give rise to the formation of larger aggregates.[17–19] These structures are also confirmed by extinction spectra collected from the solution of the silver nanoparticless, which show a band around 420 nm. SEM images of the evaporated silver film in Fig. 1b indicate silver islands in similar sizes between 20 and 150 nm, where many larger island structures have more elongated shapes and are built from smaller more spherical structures. The distance between the islands is large compared with their dimension. Therefore, no

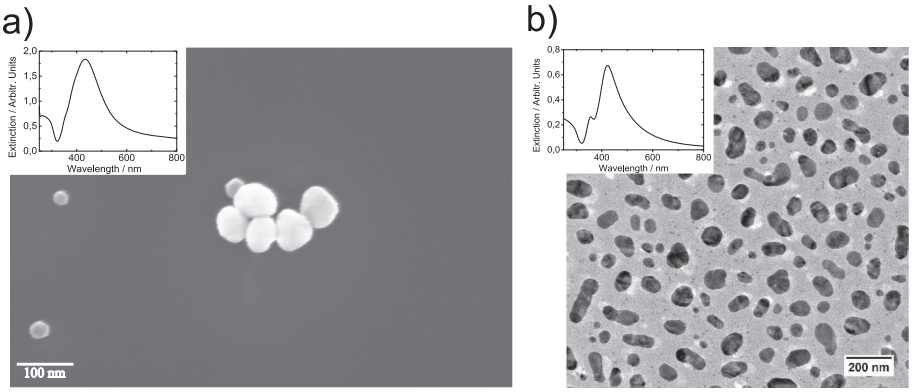

Figure 1. Characterization of surface-enhanced Raman scattering-active silver nanostructures: Electron microscope images and extinction spectra of (a) chemically prepared silver nanoparticles and nanoaggregates, (b) evaporated silver islands films.

plasmonic interaction between them can be expected.[25] This is also in agreement with the extinction spectrum collected from the silver film, which peaks around 440 nm and has no features at longer wavelengths.

Despite their extinction in the near ultraviolet and blue range, the structures shown in Fig. 1 provide strong SERS enhancement at NIR excitation. This is in agreement with former studies, which did show that extinction spectra of plasmonic structures providing extremely high enhancement level in the NIR, such as used in NIR-excited single molecule SERS experiments, do not necessarily show optically active resonances in the NIR range.[18,21,26,27] This can be understood in the framework of the plasmonic properties of these structures. Theory predicts intense and extremely localized fields in the NIR range for aggregates formed by metal nanoparticles and semicontinuous random metal films related to bright and dark plasmonic eigenmodes in these structures.[28–30]

The small aggregates shown in Fig. 1a are main building blocks for the pH sensor based on the SERS signal of the attached pMBA. Figure 2a shows SERS spectra measured from pMBA on silver nanoaggregates at different pH values between 8.6 and 4.8. Strong lines appear at 1076 and 1586 cm^{-1}, which belong to aromatic ring vibrations.[24] Lines at 1140 cm^{-1} (assigned to C–COO^- stretching mode) and 1380 cm^{-1} (assigned to the COO^- stretching mode) appear at different signal level depending on the protonation state of pMBA, which is related to the pH of the environment.[22–24,31–34] Changes in the signal ratio of the pH-sensitive SERS lines relative to the pH-insensitive aromatic ring vibrations can be obtained in dependence on the pH value. In previous work,[23,24,32,33] different signatures of pMBA have been used for pH sensing. The authors of some studies[23,24,31–33] used ratios between pMBA Raman lines at 1423 and 1380 cm^{-1}, assigned to the COO^- stretching mode of pMBA on gold and silver, respectively, and the SERS line of the ring mode at 1076 cm^{-1} to infer pH values. Additionally, in ref[32], a calibration curve for pH sensing has been generated based on the 1430 cm^{-1} line and the ring mode at 1590 cm^{-1}. Ref.[33] discusses pH measurements using variations in the ratio of the SERS peaks at 1136 and 1078 cm^{-1} in the pH range 5–9. In our work, the ring mode at 1076 cm^{-1} was not used as this Raman line might include contributions from other vibrations related to the biological target. We found the pMBA line at 1140 cm^{-1} together with the ring mode at 1586 cm^{-1} as the most convenient SERS signatures to generate a calibration curve for pH measurements. Figure 2b displays the signal ratio of these two lines as function of the pH environment. For pH values below 4.5, the intensity of the band at 1140 cm^{-1} becomes very weak, making its measurement infeasible. For pH values above 8.6, the signal ratio tends to be constants. For pH values between 4.5 and 8.6, the ratio increases linearly with increasing pH, providing a calibration curve for pH measurements. This potential operation range of the pH sensor covers physiologically interesting pH values in plants.[35] We discuss pH measurements in onion layers later in Fig. 5.

Figure 3 shows a typical Raman spectrum collected from the onion layer (spectrum a) and a SERS spectrum of the layer using pH-sensitive SERS nanosensors (spectrum b). A comparison between Raman and SERS spectra indicates strong SERS enhancement by the appearance of several 'new' SERS lines, which cannot be detected in 'normal' Raman experiments even at longer collection times, such as lines at ~1635, ~1510, ~1380, ~1270, ~1120, ~975, and ~845 cm^{-1}. On the other hand, lines that appear in normal Raman scattering, such as those at ~1075, ~1025, and ~765 cm^{-1}, show almost no SERS enhancement but appear at slightly shifted wave numbers in SERS compared with Raman. The measured SERS signatures can be tentatively assigned to chemicals available in onions: A strong band at ~1510 cm^{-1} can be related to amino acid residues[36] present on proteins, which are distributed in the cell membranes of the onion.[37] SERS lines at ~975, ~1120, and ~1380 cm^{-1} may indicate the presence of cellulose in the onion.[38]

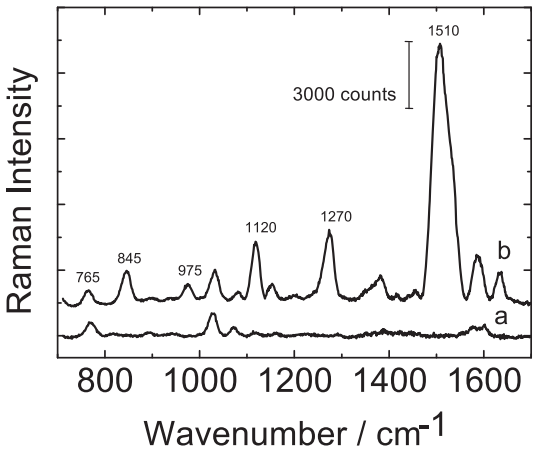

Figure 3. Typical Raman and surface-enhanced Raman scattering (SERS) spectrum of onion layers: spectrum (a) Raman spectrum collected from onion layer, (b) SERS spectrum measured from the surface of an onion layer using silver nanoaggregates with attached para mercapto benzoic acid as enhancing nanostructures. Both spectra were collected in 1 s using 2 mW 785 nm excitation.

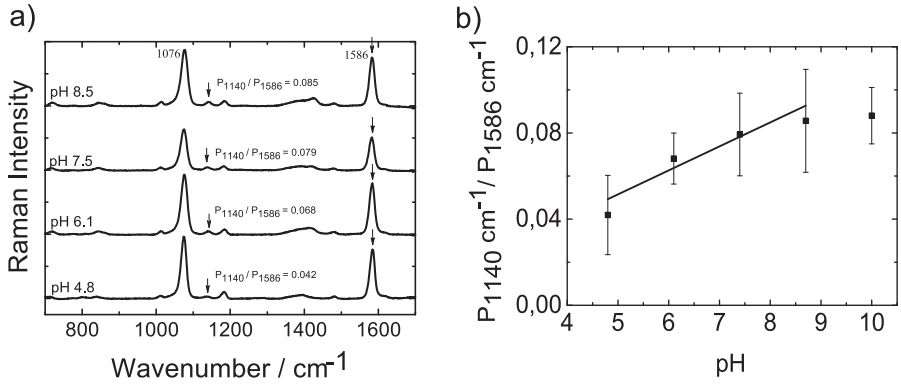

Figure 2. A pH surface-enhanced Raman scattering (SERS) sensor and calibration curve: (a) SERS spectra of para mercapto benzoic acid at different pH values and (b) signal ratio of 1140 and 1586 cm^{-1} SERS bands as a function of pH values. Error bars correspond to the standard deviation.

A line at ~1120 cm^{-1} can be assigned to the symmetric mode ν(COC) in the glycosidic bond in the cellulose. SERS signatures at ~845 and ~1635 cm^{-1} could be assigned to the ring stretch of a quercetin structure (flavonol)[39] and to a C–C stretch of a diallyl disulfide,[40] respectively, which are typically present in onions.[41] Other Raman lines we could observe in the SERS spectra of the onion layer could originate from other components present in onions such as pectin, lignin, or other polysaccharides.[42] Despite of the used silver nanoaggregates with pMBA attached, SERS signature from the reporter does not dominate the measured SERS spectra and might appear only very weak compared with the SERS signals generated by molecules present in the onion. We explain this by a possible replacement of pMBA by intrinsic biological molecules on the surface of the onion layer. It is known that proteins can contain SH groups,[43,44] and also other bioactive compounds containing sulfur compounds have been predicted in onions such as quercetin and diallyl sulfides.[45] It is well known that sulfur has a strong affinity to silver. For example, interaction of silver with thiol groups is important in terms of inhibitory effects on bacteria.[44] Because of this strong affinity of sulfur to silver, it is very likely that sulfur groups present in onion compounds favor the adsorption of these molecules on the silver nanoparticles resulting in replacement of pMBA.

Alternatively, in a second type of experiments, silver films have been used as enhancing plasmonic structures to measure SERS spectra of onion layers (protocol 2). Figure 4 shows that SERS spectra appear at about the same signal level as for silver nanoparticles, which can be expected from the very similar plasmonic properties of both structures. However, different molecular vibrations are enhanced when the onion layer contacts the silver island film compared with silver nanoaggregates placed on top of the layer. In particular, Raman lines at ~1030 and ~1080 cm^{-1} are now strongly enhanced. The different selectivity in SERS enhancement for the two SERS-active structures could be explained by optimum contacts between the plasmonic structures and the onion layer, which occurs for different parts of the layer for both structures. Therefore, different places on the onion composed by different chemical compounds exhibit optimum SERS enhancement.

Spectra shown in Figs 3 and 4 provide information of the surface of the onion layer. In order to measure SERS spectra from inside the layer and also inside onion cells, a piece of onion layer was incubated within the pH SERS nanosensor solution (protocol 3). In general, the inner of a plant cell is not easy to access by this procedure because of the properties of the cell walls in plants, which are composed of a cellulose and pectin network, limiting the pores sizes to about 6 nm.[46,47] By removing the pectin network of an onion, the pores sizes can be prolonged up to 60 nm.[47,48] It has also been discussed that silver nanoparticles can infiltrate into the cytoplasm space of a cell.[44,49] Here, we study whether SERS nanosensors can access the inner of an onion cell just by uptake through the cell wall.

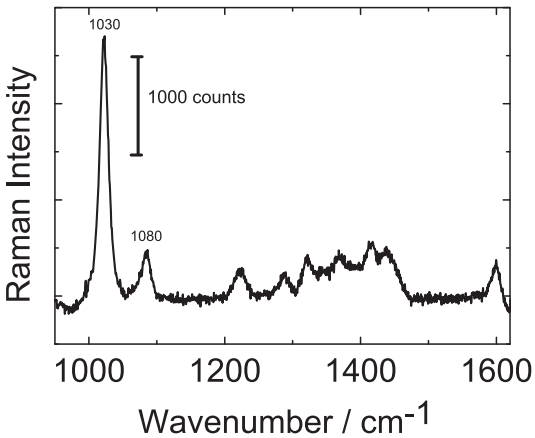

Figure 4. Surface-enhanced Raman scattering spectrum of an onion layer placed on silver islands films. Experimental conditions as in Fig. 3.

Figure 5a shows a typical SERS spectrum after 10 min of incubation. After this short time, only one SERS line at ~975 cm^{-1} related to onion can be measured. A comparison of SERS image and microscope image shows that SERS signals originate from only one point in the extracellular space between onion cells inside the layer. The Raman image suggests that after 10-min incubation, almost no nanoparticles can be found inside the onion layer.

Figure 5b displays a SERS spectrum collected from inside the onion layer after 1 h of incubation time. In contrast to Fig. 5a, now, we detect typical pMBA signatures at 1076 and 1586 cm^{-1}. Interestingly, inside the onion layer, pMBA seems not to be so rigorously replaced by other 'bio molecules' as in Fig. 3, which obviously mainly exist on the surface of the onion layer. Comparing Fig. 5b with Fig. 2a, the relative intensities of the 1586 and 1076 cm^{-1} show a deviation. This suggests that the line at 1076 cm^{-1} has also some contributions from another molecular vibration, which is related to an intrinsic onion component.

As SERS image and microscope image show, also SERS signals in Fig. 5b originate from only very few points inside the onion layer, and again, only from the space between onion cells. Because the uptake of silver nanoparticles by the onion layer appears to be a very slow process, even into the extracellular space, Fig. 5c displays a typical SERS spectrum collected from the onion after 20-h incubation time. The spectrum shows the typical signatures coming from pMBA at 1076 and 1586 cm^{-1} as well as the pH-sensitive line at 1140 cm^{-1}. Raman lines related to intrinsic onion compounds contribute to the 1076 cm^{-1} signal and appear also at 975 cm^{-1}.

Surface-enhanced Raman scattering maps using these two lines show an increased number of silver nanoparticles inside the onion layer. SERS images of the pMBA reporter and intrinsic onion lines correlate and indicate the location of plasmonic nanoparticles inside the onion layer. Despite the long incubation time, the numbers of silver nanoparticles inside the onion layer are still small, and again, the nanoparticles seem to concentrate in the extracellular space and do not enter the inner of the plant cell. This can be related to the small pore sizes that prevent penetration of plasmonic nanoparticles through the cell wall. Furthermore, silver ions that are present on the surface of the silver nanoparticles due to the preparation process can hinder the passage of the nanoparticles through the cell wall. It is known that Ag ions in cells can be toxic, and therefore, as a natural reaction, the ions are bound within the cell wall in order not to allow these ions to pass into the cells interior.[49]

We also use SERS signals of pMBA to infer the pH value in the extracellular space in an onion layer mainly composed of the two cell walls of neighboring cells. There are reports on measurements of pH in plant fiber cell walls based on fluorescence ratio imaging of introduced dyes.[50] As we have discussed previously, SERS sensors enable pH measurements in biological structures by using the signal ration of two Raman lines, i.e. the accuracy of the measurements is not disturbed by any background fluorescence signal that might exist in biological materials. Moreover, SERS works very well as nonresonant process using one-photon and two-photon excitation, and therefore, the operation wavelengths of the SERS sensor is a free parameter and can be set particularly also in the NIR.[15,24,31]

Journal of RAMAN SPECTROSCOPY

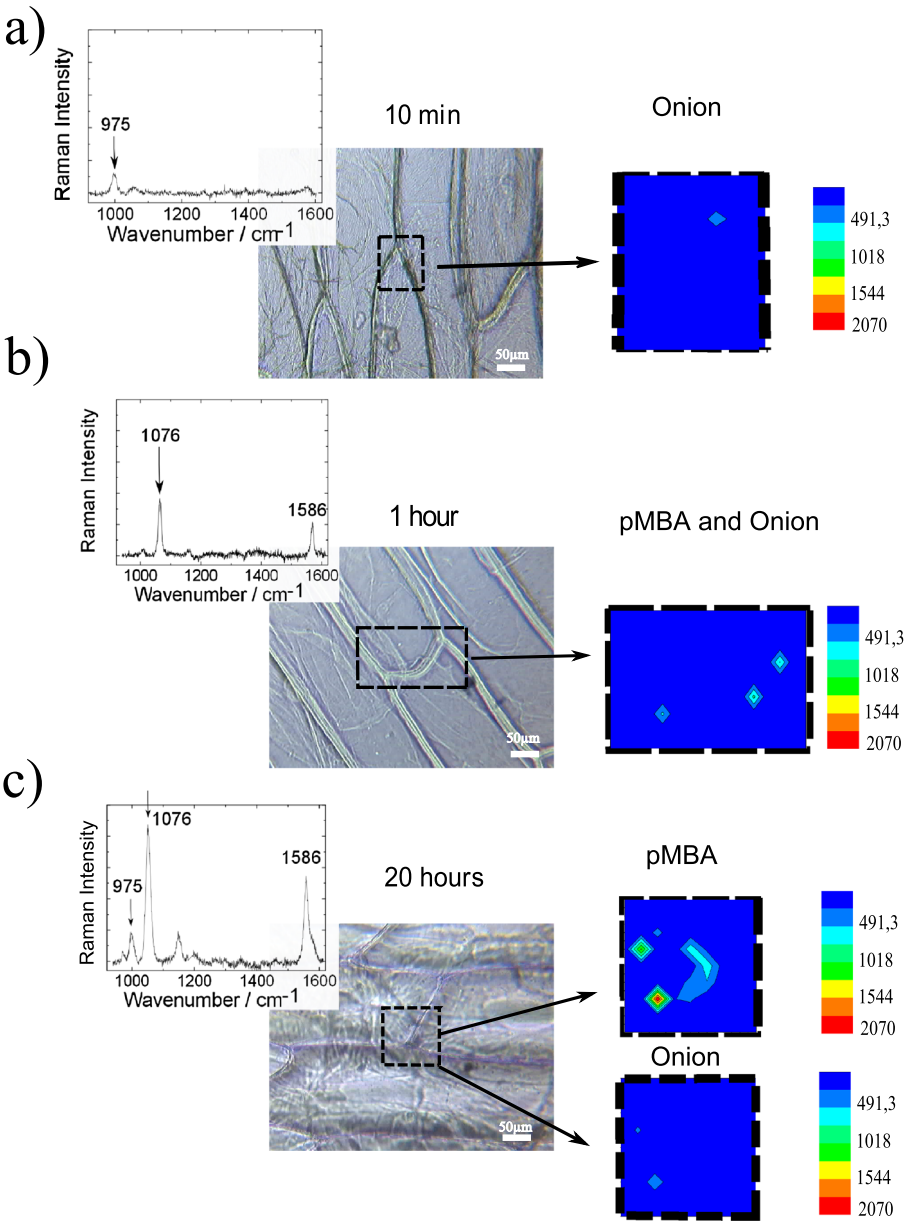

Figure 5. Surface-enhanced Raman scattering (SERS) spectra collected from inside an onion layer after incubation with silver nanoaggregates with para mercapto benzoic acid (pMBA) attached. (a–c) represent different incubation times. Spectra indicate Raman lines of intrinsic compounds of the onion (a) and of both onion and reporter (b, c). The images display SERS signals mapped over the rectangle shown in the microscopic image of the onion layer at the Raman shift indicated in the spectra by arrows.

SERS spectra of pMBA measured from the extracellular space inside the onion layer give an average signal ratio of 0.06 ± 0.001 for pMBA lines at 1140 and 1586 cm^{-1}. According to the calibration curve from Fig. 2b, this signal ratio corresponds to pH values of 5.84 ± 0.5 pH. Conferring with the pH values listed of common food, the pH of red onions is in the range 5.30–5.88.[51]

Conclusion

We have investigated SERS as a method for collecting information on plant materials and pH values inside plants using onion layers as a biological object. In addition to SERS sensors made from silver nanoaggregates, placing thin layers of plant material on silver islands films is an effective and easy way for studying intact plant material, which does not require any sophisticated sample preparation. Enhancement of Raman signals due to SERS allows detection of strong Raman signatures of chemicals in the onion layer without destroying or modifying its internal structure. Different spectra from different places in the layer indicate the complex and heterogeneous chemical structure of the biological target. SERS images show that measured SERS signals come from the extracellular space of the onion layer. Our studies show that SERS-active silver nanoaggregates in sizes between 60 and 110 nm do not penetrate the cell wall of the plant. SERS studies do not only provide vibrational signatures, and thereby molecular structural information on chemical constituents of plants, SERS spectra of pH-sensitive reporter molecules also deliver information on the pH value inside plants, in our experiments, the pH in the extracellular space of the onion.

Acknowledgements

We thank Kaare Hartvig Jensen and Janina Kneipp for interesting discussions and Harald Kneipp for support of the experiments and data analysis. This work was performed in the context of the European COST Action MP1302 Nanospectroscopy.

References

[1] D. Drescher, J. Kneipp, *Chem. Soc. Rev.* **2012**, *41*, 5780.
[2] L. Pu, S. Brady, *Plant Physiol.* **2010**, *152*, 411–419.
[3] J. W. Allwood, R. C. H. De Vos, A. Moing, C. Deborde, A. Erban, J. Kopka, R. Goodacre, R. D. Hall, in *Methods in Enzymology*, vol. *500*, (Eds.: D. Jameson, M. Verma, H. V. Westerhoff), Academic Press, Burlington, **2011**, pp. 299–336.
[4] E. Reich, A. Schibli, *High-Performance Thin-Layer Chromatography for the Analysis of Medicinal Plants*, Thieme, New York, **2006**.
[5] S. S. Conte, E. L. Walker, *Curr. Top. Membr.* **2012**, *69*, 295–322.
[6] M. Baranska, M. Roman, J. C. Dobrowolski, H. Schulz, R. Baranski, *Curr. Anal. Chem.* **2013**, *9*, 108–127.
[7] K. Kneipp, *Phys. Today* **2007**, *60*, 40–46.
[8] J. Kneipp, H. Kneipp, K. Kneipp, *Chem. Soc. Rev.* **2008**, *37*, 1052–1060.
[9] M. Seibert, T. M. Cotton, *FEBS Lett.* **1985**, *182*, 34–38.
[10] R. Gessner, P. Rösch, W. Kiefer, J. Popp, *Biopolym. - Biospectroscopy Sect.* **2002**, *67*, 327–330.
[11] L. Zeiri, *J. Raman Spectrosc.* **2007**, *38*, 950–955.
[12] A. Shen, J. Guo, W. Xie, M. Sun, R. Richards, J. Hu, *J. Raman Spectrosc.* **2011**, *42*, 879–884.
[13] L. Qiu, P. Liu, L. Zhao, M. Wen, H. Yang, S. Fan, *Vib. Spectrosc.* **2014**, *72*, 134–141.
[14] Z. A. Nima, M. H. Lahiani, F. Watanabe, Y. Xu, M. V. Khodakovskaya, A. S. Biris, *RSC Adv.* **2014**, *4*, 64985–64993.
[15] J. Kneipp, H. Kneipp, B. Wittig, K. Kneipp, *Nanomedicine Nanotechnology, Biol. Med.* **2010**, *6*, 214–226.
[16] P. C. Lee, D. Meisel, *J. Phys. Chem.* **1982**, *86*, 3391–3395.
[17] K. Kneipp, E. Roth, C. Engert, W. Kiefer, *Chem. Phys. Lett.* **1993**, *207*, 450–454.
[18] K. Kneipp, Y. Wang, H. Kneipp, L. T. Perelman, I. Itzkan, R. R. Dasari, M. S. Feld, *Phys. Rev. Lett.* **1997**, *78*, 1667–1670.
[19] K. Kneipp, H. Kneipp, G. Deinum, I. Itzkan, R. R. Dasari, M. S. Feld, *Appl. Spectrosc.* **1998**, *52*, 175–178.
[20] K. B. Mogensen, K. Kneipp, *J. Phys. Chem.* **2014**, *118*, 28075–28083.
[21] K. B. Mogensen, M. Gühlke, J. Kneipp, S. Kadkhodazadeh, J. B. Wagner, M. Espina Palanco, H. Kneipp, K. Kneipp, *Chem. Commun. (Camb.)* **2014**, *50*, 3744–3746.
[22] A. Michota, J. Bukowska, *J. Raman Spectrosc.* **2003**, *34*, 21–25.
[23] S. W. Bishnoi, C. J. Rozell, C. S. Levin, M. K. Gheith, B. R. Johnson, D. H. Johnson, N. J. Halas, *Nano Lett.* **2006**, *6*, 1687–1692.
[24] J. Kneipp, H. Kneipp, B. Wittig, K. Kneipp, *Nano Lett.* **2007**, *7*, 2819–2823.
[25] S. Kadkhodazadeh, J. R. De Lasson, M. Beleggia, H. Kneipp, J. B. Wagner, K. Kneipp, *J. Phys. Chem. C* **2014**, *118*, 5478–5485.
[26] K. Kneipp, H. Kneipp, *Beilstein J. Nanotechnol.* **2013**, *4*, 834–842.
[27] K. Kneipp, H. Kneipp, J. Kneipp, *Chem. Sci.* **2015**, *00*, 1–6.
[28] V. A. Markel, L. S. Muratov, M. I. Stockman, V. M. Shalaev, T. F. George, *Phys. Rev. B* **1991**, *43*, 8183.
[29] M. I. Stockman, V. M. Shalaev, M. Moskovits, R. Botet, T. F. George, *Phys. Rev. B* **1992**, 46, 2821–2830.
[30] M. I. Stockman, S. Faleev, D. J. Bergman, *Phys. Rev. Lett.* **2001**, *87*, 167401.
[31] J. Kneipp, H. Kneipp, A. Rajadurai, R. W. Redmond, K. Kneipp, *J. Raman Spectrosc.* **2009**, *40*, 1–5.
[32] A. M. Schwartzberg, T. Y. Oshiro, J. Z. Zhang, T. Huser, C. E. Talley, *Anal. Chem.* **2006**, *78*, 4732–4736.
[33] Y. Liu, H. Yuan, A. M. Fales, T. Vo-Dinh, *Proc. Spie* **2014**, 8957, 895703–1.
[34] K. V. Kong, U. S. Dinish, W. K. O. Lau, M. Olivo, *Biosens. Bioelectron.* **2014**, *54*, 135–140.
[35] L. Perry. pH for the garden; University of Vermont. Extension Department of Plant and Soil Science, **2003**. (URL: http://pss.uvm.edu/ppp/pubs/oh34.htm). Accessed on 1 March 2015
[36] J. Hu, R. S. Sheng, Z. S. Xu, Y. Zeng, *Spectrochim. Acta Part A Mol. Biomol. Spectrosc.* **1995**, *51*, 1087–1096.
[37] J. L. Brewster, H. D. Rabinowitch, *Onions and Allied Crops*, CRC Press, Boca Raton (Florida), **1990**.
[38] M. Chylińska, M. Szymańska-Chargot, A. Zdunek, *Plant Methods* **2014**, *10*, 14.
[39] Y. Numata, H. Tanaka, *Food Chem.* **2011**, *126*, 751–755.
[40] M. T. Devlin, V. F. Kalasinsky, I. W. Levin, *J. Mol. Struct.* **1989**, *213*, 35–50.
[41] M. Corzo-Martínez, N. Corzo, M. Villamiel, *Trends Food Sci. Technol.* **2007**, *18*, 609–625.
[42] R. H. Wilson, A. C. Smith, M. Kacuráková, P. K. Saunders, N. Wellner, K. W. Waldron, M. Kac, *Plant Physiol.* **2000**, *124*, 397–405.
[43] W. M. Morton, *Plant Physiol.* **1969**, *44*, 168–172.
[44] Q. L. Feng, J. Wu, G. Q. Chen, F. Z. Cui, T. N. Kim, J. O. Kim, *J. Biomedial Mater. Res.* **2000**, *52*, 662–668.
[45] X. Lu, The application of molecular vibrational spectroscopy to determine selective bioactive compounds, total antioxidant activity and the antimicrobial effect of onion (*Allium cepa*) and garlic (*Allium sativum*), Diss. Washington State University, **2011**. (*URI:* http://hdl.handle.net/2376/2882). Accessed on 6 February 2015
[46] N. Carpita, D. Sabularse, D. Montezinos, D. P. Delmer, *Science* **1979**, *205*, 1144–1147.
[47] P. Albersheim, A. Darvill, K. Roberts, R. Sederoff, A. Staehelin, *Plant Cell Walls from Chemistry to Biology*, Garland Science, New York, **2010**.
[48] M. C. McCann, B. Wells, K. Roberts, *J. Cell Sci.* **1990**, *96*, 323–334.
[49] A. Manara, in *Plants and Heavy Metals*, (Ed.: A. Furini), SpringerBriefs in Molecular Science, Netherlands, **2012**, pp. 27–54.
[50] B. J. Hidayat, L. G. Thygesen, K. S. Johansen, *Cellulose* **2013**, *20*, 1041–1055.
[51] A. Jonathan, R. Ann, pH values of common foods and ingredients, University of Wisconsin System, **2015**, pp. 2–3. (URL: https://www.foodsafety.wisc.edu/business_food/files/Approximate_pH.pdf) Accessed on 26 November 2014

end of paper

Beginning of second part of the PhD project

In this second part of the thesis, focus is on cells and biosensors. As mentioned in section 4.4, the key elements of a biosensor are bioreceptors (able to chemically react and recognize specific targets) and reader/transducer media (able to change signals from the receptor into measurable outputs)[124]. Similar to the first part of this project, where the receptor was a pH sensitive reporter molecule (i.e. pMBA) and the transducer media were plasmonics (Chapter 4), during the second part, biomimetic systems could be the active elements of the biosensor. Thus, the receptor that reacts under different environments could be a membrane protein while the transducer media could be the matrix that hosts the protein (e.g. a cell membrane) where the biological events takes place providing a recognizable signal[124]. In addition, the metrological part of the biosensor system (responsible for transforming the signal provided by the reader into a corresponding electrical signal) will be an optical trapping device (described in Chapter 2 and Chapter 6), while in the first part of the project it was the Raman-SERS setup (Chapter 2).

The next two chapters, i.e. Chapter 5 and Chapter 6, involve the design of an optically based sensor; addressing the topic from a different point of view compared to the first part of the project. Chapter 5 is related with molecular interactions in cells or cell-like structures, e.g. membrane-protein interactions where the chemical (activity of the protein) and structural (curvature/diffusivity through a membrane) properties of the membrane and protein are investigated. Chapter 6, on the other hand, is based on the development of a related metrological part.

Chapter 5

Biomimetic systems as sensors

5.1 Introduction

Different devices for studying cells based on biomimetic systems have been presented in the literature, e.g. artificial cells for drug delivery applications, for water purification purposes as well as for energy conservation technologies[125–128]. Very often, biomimetic systems are used in order to perform *in-vitro* studies of the surface chemistry of a cell. These systems artificially replicate the natural environment of a cell, allowing to mimic their natural properties, and thus, study the properties of a cell environment or interaction of their constituents (e.g. membrane-proteins). Lipid membranes have been investigated intensively since they not only act as a protective container for cells, but also, provide the place where many chemical interactions, e.g. cell communications and transport of molecules, take place[76].

Already in 1977, for the first time the formation of a stable synthetic vesicle composed by an organic compound was shown[129]. Since then, numerous work based on building robust and stable biomimetic sensors have been done as reviewed recently in[126,130]. For example, systems composed of lipid bilayers where the head of the lipids have been altered in order to increase the robustness of the system, e.g. membranes attached to surfaces or surrounded by hydrogel films[131,132]. Further, phospholipids, block-copolymers and cholesterol are often used to build robust biomimetic systems since they naturally assemble into vesicles or lamellae[133].

The membrane curvature is strongly influenced by the chemical properties of its constituents, i.e. head groups, polar/apolar interfaces and hydrocarbon chain regions[134–139]. For example, the cylindrical molecular shape of phosphatidylserine (PS) and phosphaticholine (PC) result in the formation of bilayers, while the conical molecular shape of phophatidylethanolamine (PE) results in the formation of inverse hexagonal phases as re-

viewed in e.g.[139,140]. It has also been shown that the addition of solvents and/or cholesterol to a lipid mixture influence the structural ordering of the lipid chains[136,141,142]. For example, alkanes in a phospholipid membrane have been probed to strongly influences the curvature of the membrane by the chain-length alkane, i.e. the effect on the curvature is stronger for shorter chains[136].

Additionally, there is a strong link between the curvature of a membrane and the function of a protein embedded into the membrane[143–147]. The insertion of membrane-proteins into a lipid membrane leads to coupling between both the hydrophobic lipid bilayer and the hydrophobic length of the protein, altering the structure and function of the protein[148,145].

In order to build a biosensor based on a biomimetic system, both the function of the protein and of the membrane must be optimized. In section 5.2, we embedded a membrane protein called Bacteriorhodopsin (bR) into different synthetic membranes. We studied the activity response of the protein versus the capability of the membranes to let ions cross, by active and passive transport. In addition, we analyzed how the performance of lipid membranes (and that of bR) as a whole system can be modulated and controlled by the addition of cholesterol and hydrocarbon molecules as well as block co-polymers. One of the main findings was the possibility to induce a completely new membrane response, where the activity of the membrane protein and the membrane permeability is increased up to four and ten times respectively, as compared to a pure lipid or a polymeric membrane model system. In addition, we showed how the membrane protein-orientation is influenced and controlled by the membrane composition.

The main part of the experimental work was performed during my MSc thesis work, but collected and concluded during the PhD studies, where it inspired the remainder of the second part of the PhD project.

5.2 Tuning biomimetic membrane barrier properties

The manuscript has been written with shared authorship between Marta Espina Palanco (Physics Department, DTU) and Nils Helge Skovgaard (Biology Department, KU University (Denmark). My contributions to this manuscript were the experimental results obtained during my Master's Thesis project, i.e. section 2, 3.5, 3.6, 3.7 and 4from the manuscript. These results have been included in this project for two main reasons. First, several months were dedicated to write a new story for the manuscript included here, based on potential applications to design biosensors. Next, the second part of this PhD project (Chapter 6) was largely motivated by these previous results.
The manuscript has been submitted to the journal Langmuir and we are currently working on answering the queries from the referees.

5.2.1 Espina Palanco, Marta; Helge Skovgaard, Nils; Sondergaard Hansen, Jesper; Berg-Sørensen, Kirstine; Hélix-Nielsen, Claus. Article submitted 2016

beginning of paper

Tuning biomimetic membrane barrier properties by hydrocarbon, cholesterol and polymeric additives

Marta Espina Palanco‡[†], *Nils Helge Skovgaard Andersen*‡[§], *Jesper Søndergaard Hansen*[∥], *Kirstine Berg-Sørensen* [†] *and Claus Hélix-Nielsen* [*⊥]

[†] Technical University of Denmark (DTU), Department of Physics. 2800 Kgs. Lyngby, Denmark, [§] Copenhagen University (KU), Department of Drug Design and Pharmacology. 2100 Copenhagen, Denmark, [∥] Lund University, Department of Experimental Medical Science. 22100 Lund, Sweden, [⊥] Technical University of Denmark (DTU), Department of Environmental Engineering. 2800 Kgs. Lyngby Denmark & University of Maribor, Faculty of Chemistry and Chemical Engineering, 2000 Maribor, Slovenia. E-mail: clhe@env.dtu.dk

‡These authors contributed equally to this work.

ABSTRACT: The barrier properties of cellular membranes are increasingly attracting attention as a source of inspiration for designing biomimetic membranes. The broad range of potential technological applications makes the use of lipid, and lately also polymeric materials, a popular choice for constructing biomimetic membranes, where the barrier properties can be controlled by the composition of the membrane constituent elements. Here we investigate the membrane properties reported by the light-induced proton pumping activity of bacteriorhodopsin (bR) reconstituted in vesicles. Specifically we quantify how the resulting proton influx and efflux

rates are influenced by the membrane composition. We demonstrate that, by adding hydrocarbons to vesicles with reconstituted bR formed from asolectin lipids, the resulting transmembrane proton fluxes changes proportional to the carbon chain length. We replicate the same proportionality in simple 1,2-Dioleoyl-sn-glycero-3-phosphocholine (DOPC) model membranes when using cholesterol. Lastly we investigate the effects of adding the amphiphilic di-block co-polymer polybutadiene-polyethyleneoxide (PB_{12}-PEO_{10}) to phospholipid made from DOPC as well as 1,2-Dioleoyl-sn-glycero-3-phosphatidylethanolamine (DOPE), and 1,2-Dioleoyl-sn-glycero-3-phosphatidylserine (DOPS) model membranes. The proton pumping activity of bR (measured as a change in extra-vesicular pH) in mixed lipid/PB_{12}-PEO_{10} lipid systems is up to six-fold higher compared to that observed for bR containing vesicles made from PB_{12}-PEO_{10} alone. Interestingly, bR inserts with apparent opposite orientation in pure PB_{12}-PEO_{10} vesicles as compared to pure lipid vesicles. Addition of equimolar amounts of lipids to PB_{12}-PEO_{10} results in bR orientation similar to that observed for pure lipids. In conclusion our results show how the barrier properties of the membranes can be controlled by the composition of the membrane. In particular the use of mixed lipid-polymer systems may pave the way for constructing biomimetic membranes tailored for optimal properties in various applications, including drug delivery systems, biosensors and energy conservation technology.

1. INTRODUCTION

Fabrication of biosynthetic composite materials, incorporating biological constituents into synthetic matrices, is being actively investigated in basic research and for applications in biotechnology and medicine [1–3]. The use of membrane proteins is of particular interest due to

their unique biological properties [4]. Biological cell membranes per se act as effective barriers to the transmembrane flow of polar/charged solutes [5]. Membrane proteins facilitate selective transport of molecules across cell membranes. The selectivity of these proteins to transport only one or a subset of molecules, while preventing the passage of others, is so unique that functional replication using synthetic materials has proved very challenging [6,7]. Thus, harnessing this class of proteins in artificially made (biomimetic) membranes could, by virtue of their unique transport properties, provide means to create advanced materials with unprecedented properties and technological applications [8]. Despite considerable progress, accommodation of active membrane proteins in biomimetic membranes remains a challenge, which thus far has limited the commercial use of membrane proteins in technological applications [9].

The permeability barrier properties of biological membranes entail that membrane proteins are inserted into the lipid bilayer without compromising these properties and/or compromising protein function and stability. The function of any biological membrane depends on its lipid composition and the controlled presence of proteins selected from the thousands of possible membrane proteins, conferring stability and permeability to cellular membranes [10,11]. The most abundant membrane lipids are the phospholipids and sphingolipids. Amongst these, a few lipid types predominate in the plasma membrane of many mammalian cells and among those most frequent are phosphatidylcholine and sphingomyelin. Both are neutrally charged lipids under normal physiological conditions and provide stable bilayers [12] . The lipid bilayers of biological cell membranes are not singularly composed of phospholipids, and often also contain cholesterol and glycolipids. With its steroid structure, cholesterol differs from both phospholipids and sphingolipids and functions as a precursor for hormone production. Several studies show that the ring-based sterols, including cholesterol, greatly enhance the permeability barrier properties of

the lipid bilayer and therefore have an inhibiting effect on passive diffusion of ions across membranes [10,12,13]. Besides the amphiphilic molecules of the bilayer, membrane barrier properties may also be modulated by hydrocarbon-based solvents, which are naturally occurring in some biological membranes. Dolichol in its hydrophobic ester form is found in high concentrations in the liver organelle membrane and similar isoprenoids are found in bacterial membranes, α-tocopherol is concentrated in mitochondrial and lysosomal membranes (1:64 phospholipid molecules) and ubiquinone is present in most eukaryotic cells, mainly in the mitochondria [13]. The exact role of how these hydrocarbon-based solvents may influence the membrane barrier properties and membrane protein function is not well understood. However it is remarkable that mitochondrial membrane can retain transmembrane proton gradients in the inner compartment of the mitochondrion as high as 1 pH unit [5].

The micro environment surrounding membrane proteins has been reported to be modulated by lipid composition and hydrocarbon additives using aquaporins labelled with the polarity sensitive dye, Badan, as reporter system [14]. In the work presented here, we sought to investigate how different additives, i.e. solvents, cholesterol and polymeric molecules, may modulate the membrane barrier properties as well as membrane protein activity. As a reporter, we used the light-driven proton pump Bacteriorhodopsin (bR). We established a pH-response assay, to monitor how modulation of the membrane matrix composition affects the transport of protons towards the interior of the vesicle (influx) and the exterior of the vesicle (efflux). One of the key benefits of bR proton transporting dynamics is that bR only allows proton flux when activated [15] and, hence, it can be assumed that any other permeation of protons through the lipid membrane during the inactivation of bR is caused by either active transport by other transmembrane species or passive diffusion through the lipid membrane.

To alter the composition and hence the barrier properties of lipid membrane containing bR, hydrocarbon solvents such as, squalene, decane, dodecane and hexadecane were used. The solvents were tested in lipid environments primarily consisting of soybean asolectin. Furthermore, in order to examine membrane barrier properties, the permeability properties of 1,2-Dioleoyl-sn-glycero-3-phosphocholine (DOPC) vesicles containing different ratios of cholesterol were investigated, i.e. how the presence of sterols affects the proton flux. Lastly, lipid- mimicking polyethyleneoxide-polybutadiene (PEO_{10}-PB_{12}) di-block co-polymer (DBP) units were used as additives to investigate both their effect on the membrane barrier properties of proteoliposomes containing bR, and on the orientation and activity of bR. pH-measurements of the systems showed significant effects on both membrane permeability and bR-activity in response to the additives. Both influx and efflux kinetics changed significantly when solvents, such as decane and squalene, were added to the membrane. Thus addition of hydrocarbon solvents showed an inverse linear relationship between hydrocarbon chain length and the proton permeability for both active and passive transport. Similarly, addition of cholesterol resulted in the same linear tendency with a decrease of proton permeability with increasing amounts of cholesterol, showing how it is possible to increase and decrease membrane permeability simply by titrating with cholesterol. Furthermore, we found that bR-activity and directionality are strongly altered by the addition of DBP to the lipid membrane. Interestingly, the presence of DBP also showed a strong effect on membrane permeability, causing a tendency to retain the proton gradients and also to invert the bR-orientation at high polymer to lipid ratios. Our results show that bR reconstituted in mixed DBP/phospholipid systems results in a fast protein response with a large ΔpH upon illumination. This suggests that such mixed lipid-polymer systems may be advantageous in technological applications (e.g. light sensors) based on bR.

Generally, the results presented here addressing membrane barrier properties and their modulation may be relevant in biomimetic/biotechnological applications within drug delivery systems, separation technologies and chemical sensory techniques [3,4,16,17].

2. MATERIALS AND METHODS

2.1 Reagents. Lipids (1,2-dioleoyl-sn-glycero-3-phosphocholine (DOPC), 1,2-dioleoyl-sn-glycero-3-phosphatidylethanolamine (DOPE) and 1,2-dioleoyl-sn-glycero-3-phosphatidylserine (DOPS)) were purchased from Avanti Polar Lipids Inc. (Alabaster, AL, USA). Octyl–β–D–glucopyranoside (OG) was acquired from Anatrace, Inc. (Maumee, OH, USA). Asolectin from soybean, cholesterol, squalene, n–decane, n-dodecane, and n-hexadecane were obtained from Sigma Aldrich Denmark (Brøndby, Denmark). Polybutadiene-polyethyleneoxide (PEO_{10}-PB_{12}) polymers were provided by Aquaporin A/S (Denmark). All other chemicals used were of analytical grade and purchased from commercial sources.

2.2 Preparation of bR reconstituted large unilamellar liposomes and polymersomes. Lyophilized bR (~26kDa, extinction coefficient of 63000$M^{-1}cm^{-1}$ at A280nm) purple membranes were solubilized in a saline solution consisting of 0.15 M KCl with 1.3% OG. Large vesicles were created by dissolving soybean asolectin in 0.15 M KCl with 1.3% OG (8 mg/ml) and after extruded through a 400 nm polycarbonate filter. Lipid and protein was mixed in a lipid-to-protein ratio (LPR) of 300-600. The mixed protein–vesicles solution was dialyzed for 24 h in a dynamic microdialyzer dialysis device (Spectrum Laboratories Europe, Breda, The Netherlands) using a MWCO of 10,000 Daltons and a dialysate flow of 3 ml/min.

DBP was mixed with DOPE, DOPS and DOPC and diluted in chloroform, keeping a lipid-to-protein ratio (LPR) of 600. The polymer-lipid was dried under flowing nitrogen and the formed proteopolymersomes was then rehydrated in saline solution consisting of 0.15 M KCl with 1.3%

OG for 2 days. As the proteopolymersomes formed, lyophilized bR purple membranes were added and the bR polymer vesicles were finally dialysed with BioBeads® for 24 hrs. Measurements of light induced proton flux were carried out in the same way as asolectin based bR vesicles.

2.3 Bacteriorhodopsin photo induced pH-response assay. To assess the proton–pumping activity of bR, 2.5 ml of the vesicle suspension was transferred to a 3 ml UV–cuvette with magnetic stirring and placed in a dark cabinet. A glass micro pH electrode (Microelectrodes Inc., Bedford USA) was placed into the vesicle suspension. The glass microelectrode was connected with an ORION 3 STAR pH-meter (Fisher Scientific) operated through Star Plus navigator software (Fisher Scientific), which enabled automated sampling of pH measurements. Illumination was provided with a cold–light generator equipped with an incandescent halogen lamp of 200W with a light–guide (SCHOTT: model KL1500 LCD), with maximum emission spectrum at around 650 nm. The light produced was focused on the cuvette by means of a fibre optic cable. The resulting light intensity on the sample was about 80 × 103 Lux. Before illumination, the sample was equilibrated in the dark for 30 min to permit pH stabilization, and the pH baseline was subsequently recorded for 3 min. Illumination was carried out for 3 min followed by 7 min darkness, while the pH was continuously sampled throughout the experiment (3 sec recording intervals).

For solvent partitioning experiments, proteoliposomes were mixed with hydrocarbon solvent as specified (1:3 oil phase:vesicles ratio) using gentle rotation mixing over night at room temperature. Solvent equilibrated proteoliposomes were transferred to a UV–cuvette and the bR light–induced proton activity assay repeated as described for the bR reconstituted proteoliposomes.

2.4 Data analysis. All pH-data obtained in the experiments was measured in discrete intervals of 3 seconds, during a 13 minute time period, including influx and efflux periods. In order to quantify the proton flux rate across the membrane or through bR we obtained the influx and efflux time constants (τ) of each proteoliposome data by fitting normalized pH-values as a function of time to exponential decay functions (1) using Origin version 8 (OriginLab Corporation, Northampton, MA, US):

$$\Delta pH = A + B\, exp\left(\frac{-t}{\tau}\right) \qquad (1)$$

Where A is the final amplitude of the normalized curve, i.e. 1 for influx data and 0 for the efflux data, and B a negative constant value for influx data and a positive constant value for efflux. Thus, τ describes the time for the ΔpH value to reach 63% of the maximal value for influx, and decrease to 37% of the maximal value for efflux.

3. RESULTS AND DISCUSSION

3.1 Influence of hydrocarbons as additive to bR-reconstituted liposomes. Reconstitution of bR into asolectin lipid vesicles resulted in a preferential protein orientation where, upon illumination, protons were transported actively to the interior of the vesicles ($H^+_{out} \rightarrow H^+_{in}$) (Figure 1a). The net proton flux into the vesicles led to alkalization of the external bulk medium, which was measured by a pH micro-electrode. Inactivation of bR (by terminating illumination) inhibits the bR-proton pump effect, resulting in a passive proton diffusion across the membrane ($H^+_{in} \rightarrow H^+_{out}$) causing a pH decrease of n the extra-vesicular bulk medium.

To assess how hydrocarbons of different carbon chain lengths affect protein activity and membrane barrier properties, bR-reconstituted asolectin liposomes were incubated over night with n-decane ($C_{10}H_{22}$), n-dodecane ($C_{12}H_{26}$), n-hexadecane ($C_{16}H_{34}$) and squalene ($C_{30}H_{50}$). pH-response assays of all the tested hydrocarbon proteoliposomes showed an active transport of

protons through bR (Figure1b) and passive proton diffusion across the membrane (Figure 1c). Interestingly, in both cases the pH-response changed in a hydrocarbon chain length dependent manner. In order to examine their influx and efflux rates, the rate of alkalization of the medium (which starts after 180 seconds, when bR is activated) and the rate of the acidification of the medium (which starts after 360 seconds, when bR is inactive) were extracted from Figure 1a. Our data indicates a linear relationship between hydrocarbon chain length and the time constants (τ), where the decrease of the carbon length of the solvent leads to a concomitant increase in τ for both proton influx and efflux (Figure 1d). Modulation of the lipid membrane with hydrocarbon solvents clearly has an effect on bR protein function. Protein mediated proton influx notably slows down with a >2-fold increase in τ for liposomes containing n-decane, compared to liposomes containing squalene, of which the influx rate resembled that of the natural asolectin membrane. In addition, an inverse relation exists between hydrocarbon chain length and proton pumping activity: the smaller the hydrocarbon chain length, the larger effect on bR activity. Likewise, the proton efflux was diminished more than three-fold in n-decane containing liposomes, indicating that addition of n-decane, the shortest chain length tested, results in a tighter membrane that decreases passive proton diffusion. For the hydrocarbon additives tested an inverse relation between tail length and permeability of the membrane appears to exist, see Figure 1d. Compared to the size of a lipid, the smaller alkanes (decane, dodecane and hexadecane) have a low molecular weight and are likely to partition into the inner hydrophobic core of the bilayer resulting in a thicker inner hydrophobic membrane region [18].

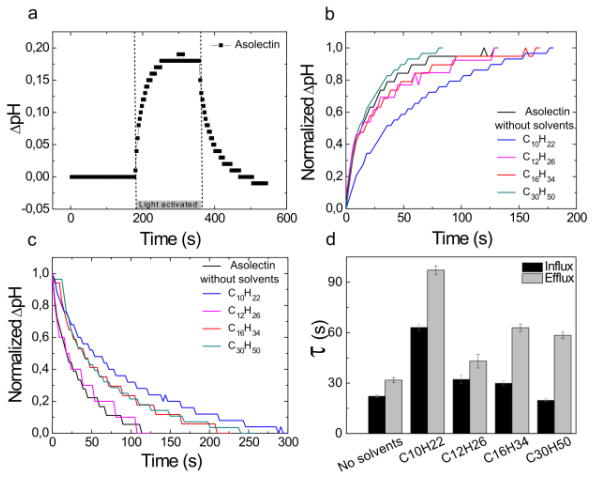

Figure 1. Hydrocarbon additives affect bR-membrane properties in a chain-length dependent manner (a) Variations of pH across bR-asolectin model membranes influenced by light/darkness vesicle environment conditions. Normalized proton-influx upon illumination (b) and proton-efflux upon darkness (c) of bR-asolectin model membranes containing different mono-chain carbohydrates. Black, blue, pink, red and green curves represent the proton transport through membranes made with pure asolectin, asolectin with n-decane, asolectin with n-dodecane, asolectin with n-hexadecane and asolectin with squalene respectively. (d) Comparison of time constants of the influx (black) and efflux (grey) rates based on an exponential decay function for each membrane model system. Standard deviations of τ from the curve fitting are in range of 1-4 seconds.

3.4 Influence of cholesterol on bR mediated proton transport in DOPC proteoliposomes. Similar to hydrocarbon solvents, the membrane barrier properties can also be modulated by cholesterol. In order to study cholesterol's effect on the membrane barrier properties as well as on the protein activity, bR reconstituted in DOPC liposomes were incubated with cholesterol at different concentrations, i.e. 10%, 20% and 40% cholesterol molar concentrations. Our results showed that the addition of cholesterol to pure DOPC liposomes greatly influences the proton

transport through both: the protein when bR is activated (Figure 2a) and the membrane due to their passive diffusion across the membrane (Figure 2b). Addition of a modest amount of cholesterol to DOPC proteoliposomes decreased the permeability of protons through the plasma membrane, causing an increase in τ values (Figure 3c); however, increasing the amount of cholesterol beyond 10% seems to have a negative effect on the proton barrier properties. Both influx and efflux showed a linear, inverse relationship between τ and the cholesterol content of DOPC membrane. With almost similar ΔpH values as for the hydrocarbon solvent system, we conclude that cholesterol exhibit the highest decrease in permeability at a concentration around, or less than, 10 wt%, resulting in a two- and three-fold slowing of proton flux when the proton pump is activated and deactivated respectively. It is also evident that the τ values for cholesterol containing liposomes are very close to that of hydrocarbon solvents in asolectin based membranes despite the rather large difference in chemical structure between cholesterol and solvent hydrocarbon chains.

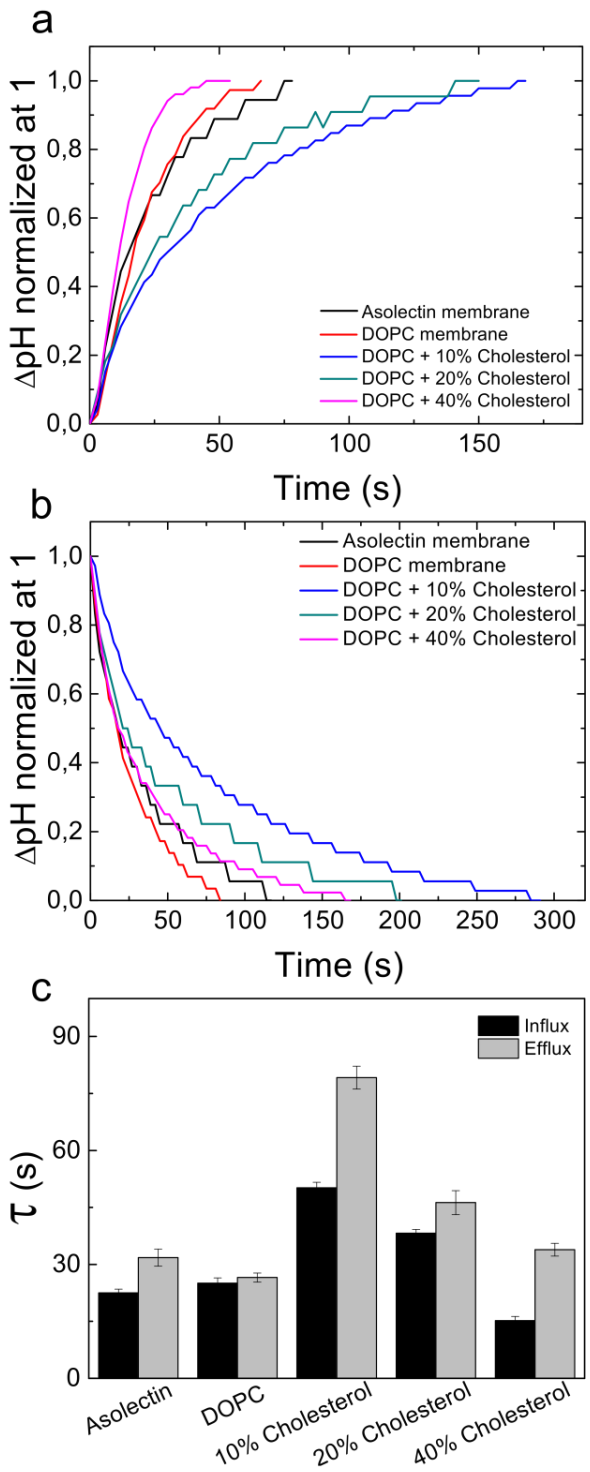

Figure 2. Cholesterol content efficiently alters bR-membrane properties. Normalized proton influx upon illumination (a) and efflux upon darkness (b) from phospholipids model membranes

with cholesterol. The black, red, blue, green and pink curves represent the proton transport through pure asolectin, pure DOPC, DOPC with 10% cholesterol, DOPC with 20% cholesterol and DOPC with 40% cholesterol membranes respectively. (c) Comparison of time constants of the influx (black) and efflux (grey) rates based on an exponential decay function for each membrane model system. Standard deviations of the inverse exponential curve fitting are in the range of 1-2 seconds.

3.5 Mixed amphiphilic di-block copolymer-lipid membranes. Recently, a promising synthetic biomimetic material has been introduced in the form of amphiphilic di-block copolymers (DBPs). Polymer based membranes have shown valuable properties in mimicking biological membranes as polymers generally have high stability when structured into vesicular forms [19,20]. Compared to lipid bilayers, the permeability of DBP bilayers is decreased and overall, polymeric membranes have been shown to be robust and highly stable membrane mimics [19]. However, currently there are only a small number of examples where membrane proteins have been incorporated successfully into amphiphilic DBP based membranes [21–24]. This is a reflection of the general challenge in protein reconstitution that the hydrophobic mismatch between the hydrophobic thickness of the membrane and the hydrophobic length of transmembrane proteins affect both insertion and function of proteins [25–27]. In order to investigate how DBP affects the membrane barrier properties as well as the bR-activity, bR was reconstituted into either pure DBP or into mixed DBP/phospholipid membranes (Figure 3). In contrast to pure lipid bilayers, the proton pumping activity of bR in pure DBP systems resulted in a net efflux of protons, inverse of what we observed for asolectin based proteoliposomes, causing acidification of the extra-vesicular medium when activated (Figure 3a). These results indicate

that the preferential orientation of bR is opposite to that of the proteoliposomes described in Figures. 1 and 2. However, for the period of bR-activation, the amplitude of the pH varies in absolute values of at max only 0.10 compared to the values of almost 0.20 in asolectin and 0.38 in DOPC liposomes (see Figure S1), which may indicate, that only a fraction of the bR is incorporated in a functional state. However, the persistence of the characteristic purple colour of the bR-polymersomes indicated that some bR protein was intact, and the results indicate a diminished preferential bR-orientation. Interestingly, the pH value does not return to the resting (dark) level, suggesting that the polymer membranes are able to maintain the proton gradient across the membrane. This is likely due to an increase of the stiffness and a concomitant decrease in the permeability of the polymer membrane[19].

The addition of DBP units into lipid membranes causes significant effects on the lipid membrane barrier properties and bR function. Figure 3b, 3c and 3d show the proton pumping activity of bR in mixed PEO_{10}-PB_{12}/DOPC, DOPS and DOPE membranes at different concentrations. For all three matrices, the addition of PEO_{10}-PB_{12} at high polymer to lipid molar concentrations (1 to 0.01) causes poor active transport of protons compared to non-DBP proteoliposomes. The activation of bR during illumination, results in low pH-amplitude signals, up to 0.07 pH values for DOPS membranes, 0.05 pH values for DOPE and less than 0.04 pH values for DOPC matrices (Figure 3b). As can be seen, the preferential orientation of bR is not only affected in pure polymer matrices but also with high polymer to lipid ratios. Moreover, the presence of DBP in this case still seems to play an important role in terms of the membrane permeability, maintaining the created pH gradient during darkness. When the polymer to lipid molar concentration is reduced 10-fold (1 to 0.1) (Figure 3c), the preferred natural bR-orientation is slowly restored in the DOPE membranes, similar to that of the proteoliposomes described in

Figure 1a, causing a positive amplitude signal of around 0.05 pH units. Still, the influence of PEO_{10}-PB_{12} in DOPS and DOPC liposomes, in terms of bR-orientation and permeability, is strong enough to produce acidification of the medium and to maintain the ion gradient. In all three systems, even lower polymer to lipid ratio (down to 1:1), results in a high proton translocation towards the vesicle interior (Figure 3d). In particular, DBP/DOPE membranes effectively re-establish a strong signal, nearly double in size of the signal of asolectin proteoliposomes (Figure 1a). Among the three bR-reconstituted mixed membranes, DBP/DOPE polymersomes show the largest pH responses, probably due to a better matching of the matrices with the membrane protein. The effect of higher bR-activity in DOPE systems indirectly supports the notion that non-lamellar lipids have an effect on the curvature of the membrane, thereby regulating its activity [28–30]. An interesting observation is that, DBP/DOPS vesicles show an almost constant pH value when bR is activated, suggesting an equal distribution between the bR- orientations towards both, the internal space and external phase. Remarkably, the permeability of the DOPS, DOPC, and DOPE systems, at low polymer to lipid ratios, is considerably increased in the presence of PEO_{10}-PB_{12}, resulting in a fast kinetics of the pH-signal during influx and efflux.

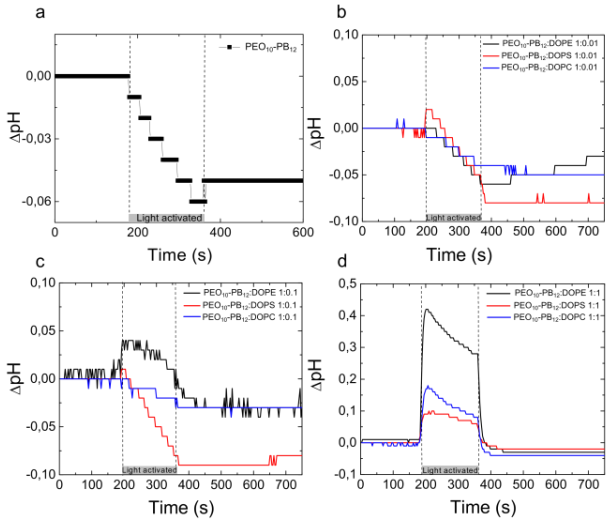

Figure 3. bR orientation is greatly affected in pure polymeric and polymer/lipid composite membranes. Variations of pH across (a) bR-pure PEO_{10}-PB_{12} based membranes and (b,c,d) bR-mixed PEO_{10}-PB_{12} / phospholipids model membranes influenced by light/darkness vesicle environment conditions. PEO_{10}-PB_{12} / DOPE (black curve), PEO_{10}-PB_{12} / DOPS (red curve) and PEO_{10}-PB_{12} / DOPC (blue curve) model membranes are fabricated at (b) 100 polymer to phospholipid molar ratio, (c) 10 polymer to phospholipid molar ratio and (d) 1 polymer to phospholipid molar ratio.

3.6 DBP vesicle size distribution. Protein activity is, to some extent, related to liposome sizes [31]. Therefore, in order to investigate how the long chains of DBP affect the bR-activity into these proteoliposomes, the size distribution of the three mixed DBP/lipid matrices were characterized by Dynamic Light Scattering (DLS). Figure 4 shows the relative size distribution of DBP/DOPE, DBP/DOPC and DBP/DOPS based vesicles at different concentrations as well as of pure DBP vesicles. The size distribution of pure DBP matrices results in a vesicle-population of around 350 nm (Figure. 4a). However, there is a clear reduction of the vesicle size, down to 50 nm, as the polymer to lipid ratio decreases, underlining the effect that DBP exhibits on the lipid membrane

(Figure 4b, 4c and 4d). Therefore, a decrease of the polymer/lipid ratio not only improves the bR-activity, but is also related with the vesicle-size distribution, supporting the idea that lower radii of curvature cause higher performance of the protein.

High polymer/lipid molar ratios, i.e. 1:0.01 and 1:0.1, notably affect the distribution of sizes of the DOPE, DOPS and DOPC vesicles (Figure 4b - 4d). Consequently, the vesicle-size-distribution shifts from 350 nm to lower diameter-values, as a general tendency in the three systems. This correlates with the results from Figure 3b and 3c, where proteoliposomes at these polymer/lipid ratios, showed a different behavior compared with pure polymer systems, in terms of bR-activity and membrane barrier properties. Furthermore, a decrease of the polymer/lipid ratios down to 1:1, caused the formation of monodisperse vesicles around 50 nm in diameter. In particular, DBP/DOPE membranes showed a strong tendency to form small (<50 nm) vesicles (Figure 4b). In this context, the capability of DOPE systems to reduce the size distribution (and increase the curvature) of the polymersome translates into systems with higher bR-activity (Figure 3d).

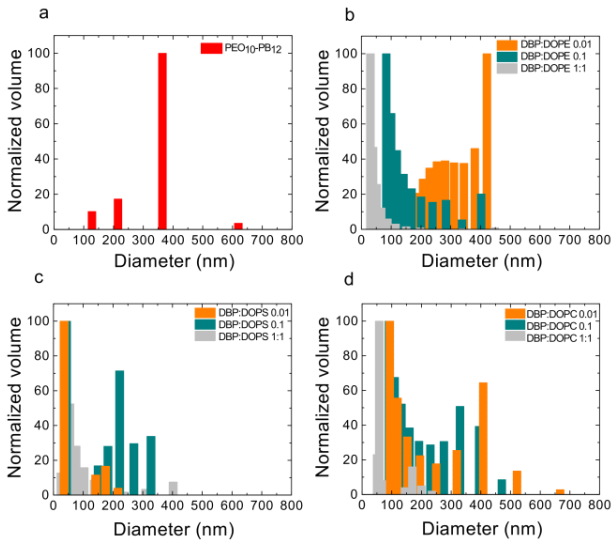

Figure 4. Vesicle size distribution of bR reconstituted in DOPE, DOPS and DOPC based membrane systems with and without additives. (a) Vesicle size distribution of pure bR- PEO_{10}-PBE_{12} based membrane systems. (b,c,d) Vesicle size distribution of bR in DOPE, DOPS and DOPC membrane systems respectively with PEO_{10}-PBE_{12} as additive at 100 (orange), 10 (green) and 1 (grey bars) polymer to phospholipid molar ratio.

3.7 Future biomimetic membrane design strategies. Depending on the desired membrane functionality, one may tune the membrane to either induce larger influx and efflux across the membranes or to sustain the pH gradients by producing less permeable membranes. Figure 5 shows an overview of the different possibilities presented as a correlation between influx and efflux properties of liposomes with and without cholesterol and solvents, pure lipids, pure polymersomes as well as mixed polymer/phospholipid vesicles. There are four apparent correlation tendencies indicated by the blue, black, green, and red circles which can be associated with specific membrane compositions.

The diffusion of protons through polymer/phospholipids mixed membranes (blue circle) slow down both the influx and efflux kinetics, causing influx time constants of 7-10 seconds and

efflux time constants of around 8-10 seconds (Table 5b). A low value of τ, for both influx and efflux, indicates a fast transport of protons through bR as well as a fast passive diffusion through the membrane respectively. Moreover, the rapid diffusion of protons through the membrane matrix, indicates its diminished capability to act as proton barrier. However, the active diffusion of protons through bR in pure lipid membranes (black circle) seems to be smaller, compared to the mixed systems, resulting in influx time constants of around 20-25 seconds. In the same context, the pH-gradient created in these systems is dissipated slower through the lipid membrane, compared to the mixed polymer/phospholipid vesicles where the efflux time constants are around 26-31 seconds. As expected [14], the addition of hydrocarbon solvents into phospholipid vesicles seems to alter not only hydrophobic protein-lipid interactions but also reduce the ability of the vesicle membrane to let protons through (red circle), causing less permeable membrane systems. For this group, time constants increase to values of 20-65 seconds during influx and 40-100 seconds during efflux, i.e. one order of magnitude higher than for the mixed lipid/polymer systems. As the hydrocarbon tail length increases (systems 2, 4, 5), there is a tendency towards lower time constants, suggesting a faster diffusion than in system 3. This supports the idea that the hydrophobic interactions depends strongly on the solvent partitioning[14]. For example, alkaline solvents such as n-decane, more easily partition into the lipid membrane compared to squalene [32], resulting in a thicker and thus less permeable membrane. The influx and efflux time constants of systems with hydrocarbons are generally higher than for both pure lipids and polymer/lipid mixed systems, resulting in lower permeability towards protons. Also the increased cholesterol concentration in phospholipid membranes slows down the passive diffusion of protons through the membrane, resulting in higher influx time constants of around 15-50 seconds and efflux time constants of around 33-80 seconds (green circle).

a

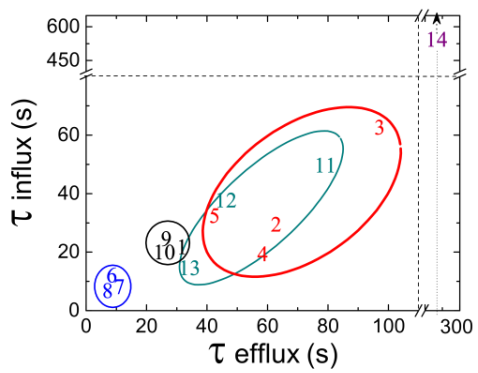

b

	Model system	Time constant influx (s)	Time constant efflux (s)
1	Asolectin	22.26 ± 0.98	31.80 ± 1.58
2	Asolectin & Hexadecane	29.99 ± 1.34	62.94 ± 2.20
3	Asolectin & Decane	63.17 ± 1.95	97.15 ± 2.62
4	Asolectin & Squalene	19.85 ± 0.92	58.46 ± 1.78
5	Asolectin & Dodecane	32.31 ± 2.55	43.08 ± 4.16
6	PEO_{10}-PB_{12}:DOPC	10.10 ± 1.65	9.17 ± 0.47
7	PEO_{10}-PB_{12}:DOPS	7.6 ± 1.01	10.64 ± 1.16
8	PEO_{10}-PB_{12}:DOPE	7.16 ± 0.87	8.25 ± 0.24
9	DOPC	25.03 ± 1.45	26.55 ± 0.82
10	DOPS	20.79 ± 1.21	27.09 ± 1.52
11	DOPC & 10% cholesterol	50.19 ± 1.45	79.17 ± 2.09
12	DOPC & 20% cholesterol	38.26 ± 0.97	46.27 ± 2.20
13	DOPC & 40% cholesterol	15.22 ± 1.08	33.89 ± 1.17
14	PEO_{10}-PB_{12}	Never recovers	200.38±18.70

Figure 5. Comparison of membrane properties with investigated additives. (a) Comparison of Influx and efflux rates of protons in bR-model membrane systems composed by pure lipids (number 1, 9, 10), asolectin membranes with mono-chain carbohydrates (2, 3, 4, 5), DOPC membranes with cholesterol (11, 12, 13) pure polymers (14) as well as mixed polymer/phospholipid membranes (6, 7, 8). (b) Influx and efflux values for each model membrane system with their parametric standard deviations of the inverse exponential curve fitting.

4. CONCLUSIONS

In this work, we have analyzed the bR-activity in membranes of various compositions as well as the membranes capability to retain a proton gradient created by activation of bR. We have shown how the barrier properties of pure phospholipid bilayers can be altered by additives including hydrocarbons, cholesterol and polymers. Hydrocarbon solvents as well as cholesterol tend to decrease membrane permeability towards protons. The dose-dependency of cholesterol as

well as the length-dependency of hydrocarbon solvents on membrane structure can be used to customize permeability properties in liposome models. Thus, when increasing the concentration of cholesterol we observe a linear decrease in proton permeability. Using DBP as additive to phospholipid based vesicles gave rise to faster efflux and influx by a factor of up to three compared to pure phospholipid systems (DOPC, DOPS or Asolectin proteoliposomes), diminishing the vesicles ability to retain protons in the intracellular compartment.

Polymeric materials as building blocks, in biotechnology, have recently gained a lot of interest. There are several applications based on synthetic biomimetic membranes where the influx/efflux kinetics play an important role, i.e. within medicine, energy production devices and fast responsive biosensors among others [3,33],[17]. The importance of delivering anticancer drugs, with a precise drug release, in treatments of cancer therapy is on example[3]. The ability to control efflux kinetics in respective treatments based on drug release is important in order to minimize adverse toxic effects. Also, polymer membranes that are able to retain ion gradients in a homogenous environment, could potentially be a key constituent as a green alternative for the production of energy storage devices such as micro-batteries or supercapacitors [16,33]. Mixed polymer/lipid membranes, on the other hand, could be good building blocks in designing systems where fast bR mediated transport responses is desired, such as biosensors. In summary, our result show how biomimetic membranes with a reconstituted proton pump can be tailored over a wide range of proton influx and efflux rates. This knowledge is useful in design of biomimetic membrane systems aimed at a broad spectrum of applications based on the use of reconstituted membrane proteins.

AUTHOR INFORMATION

Corresponding Author

*E-mail: clhe@env.dtu.dk

Author Contributions

The manuscript was written through contributions of all authors. All authors have given approval to the final version of the manuscript. ‡These authors contributed equally.

Funding Sources

CHN was supported by the IBISS - Industrial Biomimetic Sensing and separation platform (http://www.ibiss.dtu.dk) funded by the Danish Innovation Fund Grant no. 097-2012-4.

Notes

The authors declare no competing financial interest.

ABBREVIATIONS

bR, bacteriorhodopsin; DOPC, 1,2-Dioleoyl-sn-glycero-3-phosphocholine; PB_{12}-PEO_{10}, polybutadiene-polyethyleneoxide; DOPE, 1,2-Dioleoyl-sn-glycero-3-phosphatidylethanolamine; DOPS, 1,2-Dioleoyl-sn-glycero-3-phosphatidylserine; DBPs, amphiphilic di-block copolymers; LPR, lipid-to-protein ratio.

REFERENCES

(1) Elsabahy, M.; Wooley, K. L. Design of Polymeric Nanoparticles for Biomedical Delivery Applications. Chem. Soc. Rev. 2012, 41 (7), 2521–3012.

(2) Wang, J.; Yao, K.; Wang, C.; Tang, C.; Jiang, X. Synthesis and Drug Delivery of Novel Amphiphilic Block Copolymers Containing Hydrophobic Dehydroabietic Moiety. J. Mater. Chem. B 2013, 1 (17), 2324–2332.

(3) Fan, Y.; Zhang, Q. Development of Liposomal Formulations: From Concept to Clinical Investigations. Asian J. Pharm. Sci. 2013, 8 (2), 79–90.

(4) Nielsen, C. H. Biomimetic Membranes for Sensor and Separation Applications. Anal. Bioanal. Chem. 2009, 395 (3), 697–718.

(5) Bruce, A.; Johnson, A.; Lewis, J.; Raff, M.; Roberts, K.; Walter., P. Molecular Biology of the Cell, 4th ed.; Garland Science: New York, 2002.

(6) Kaucher, M. S.; Peterca, M.; Dulcey, A. E.; Kim, A. J.; Vinogradov, S. a.; Hammer, D. a.; Heiney, P. a.; Percec, V. Selective Transport of Water Mediated by Porous Dendritic Dipeptides. J. Am. Chem. Soc. 2007, 129, 11698–11699.

(7) Shen, Y.; Si, W.; Erbakan, M.; Decker, K.; De Zorzi, R.; Saboe, P. O.; Kang, Y. J.; Majd, S.; P., B.; Walz, T.; Aksimentiev, A.; Hou, J. L.; Kumar, M. Highly Permeable Artificial Water Channels That Can Self-Assemble into Two-Dimensional Arrays. Proc Natl Acad Sci 2015, 112, 1–6.

(8) Hirano-Iwata, A.; Niwano, M.; Sugawara, M. The Design of Molecular Sensing Interfaces with Lipid-Bilayer Assemblies. Trends Anal. Chem. 2008, 27 (6), 512–520.

(9) Perry, M.; Madsen, S. U.; Jørgensen, T.; Braekevelt, S.; Lauritzen, K.; Hélix-Nielsen, C. Challenges in Commercializing Biomimetic Membranes. Membranes (Basel). 2015, 5 (4), 685–701.

(10) Raffy, S.; Teissié, J. Control of Lipid Membrane Stability by Cholesterol Content. Biophys. J. 1999, 76 (4), 2072–2080.

(11) Trimble, W. S.; Grinstein, S. Barriers to the Free Diffusion of Proteins and Lipids in the Plasma Membrane. J. Cell Biol. 2015, 208 (3), 259–271.

(12) Ohvo-Rekilä, H.; Ramstedt, B.; Leppimäki, P.; Peter Slotte, J. Cholesterol Interactions with Phospholipids in Membranes. Prog. Lipid Res. 2002, 41 (1), 66–97.

(13) Haines, T. H. Do Sterols Reduce Proton and Sodium Leaks through Lipid Bilayers? Prog. Lipid Res. 2001, 40 (4), 299–324.

(14) Hansen, J. S.; Vararattanavech, A.; Vissing, T.; Torres, J.; Emnéus, J.; Hélix-Nielsen, C. Formation of Giant Protein Vesicles by a Lipid Cosolvent Method. ChemBioChem 2011, 12 (18), 2856–2862.

(15) Subramaniam, S.; Henderson, R. Molecular Mechanism of Vectorial Proton Translocation by Bacteriorhodopsin. Nature 2000, 406 (6796), 653–657.

(16) Xie, X. N.; Lee, K. K.; Wang, J.; Loh, K. P. Polarizable Energy-Storage Membrane Based on Ionic Condensation and Decondensation. Energy Environ. Sci. 2011, 4 (10), 3960–3965.

(17) Bradley J. Read. Oil Detection Sensor Module for Sensing Oil Leakage in Coolant System; United States, patent Application 20150268125, 2015.

(18) Elliott, J. R.; Needham, D.; Dilger, J. P.; Haydon, D. A. The Effects of Bilayer Thickness and Tension on Gramicidin Single-Channel Lifetime. BBA - Biomembr. 1983, 735 (1), 95–103.

(19) Discher, B. M.; Won, Y. Y.; Ege, D. S.; Lee, J. C.; Bates, F. S.; Discher, D. E.; Hammer, D. a. Polymersomes: Tough Vesicles Made from Diblock Copolymers. Science 1999, 284 (5417), 1143–1146.

(20) Morton, D.; Mortezaei, S.; Yemenicioglu, S.; Isaacman, M. J.; Nova, I. C.; Gundlach, J. H.; Theogarajan, L. Tailored Polymeric Membranes for Mycobacterium Smegmatis Porin A (MspA) Based Biosensors. J. Mater. Chem. B 2015, 3, 5080–5086.

(21) Muhammad, N.; Dworeck, T.; Fioroni, M.; Schwaneberg, U. Engineering of the E. Coli Outer Membrane Protein FhuA to Overcome the Hydrophobic Mismatch in Thick Polymeric Membranes. J. Nanobiotechnology 2011, 9 (1), 8.

(22) Cottenye, N.; Syga, M.-I.; Nosov, S.; Müller, A. H. E.; Ploux, L.; Vebert-Nardin, C. Biological-like Vesicular Structures Self-Assembled from DNA-Block Copolymers. Chem. Commun. 2012, 48 (20), 2615.

(23) Kumar, M.; Habel, J. E. O.; Shen, Y.; Meier, W. P.; Walz, T. High-Density Reconstitution of Functional Water Channels into Vesicular and Planar Block Copolymer Membranes. J. Am. Chem. Soc. 2012, 134 (45), 18631–18637.

(24) Habel, J.; Hansen, M.; Kynde, S.; Larsen, N.; Midtgaard, S. R.; Jensen, G. V.; Bomholt, J.; Ogbonna, A.; Almdal, K.; Schulz, A.; Hélix-Nielsen, C. Aquaporin-Based Biomimetic Polymeric Membranes: Approaches and Challenges. Membranes (Basel). 2015, 5 (3), 307–351.

(25) Mobashery, N.; Nielsen, C.; Andersen, O. S. The Conformational Preference of Gramicidin Channels Is a Function of Lipid Bilayer Thickness. FEBS Lett. 1997, 412 (1), 15–20.

(26) Nielsen, C.; Goulian, M.; Andersen, O. S. Energetics of Inclusion-Induced Bilayer Deformations. Biophys. J. 1998, 74 (4), 1966–1983.

(27) Andersen, O.; Nielsen, C.; Maer, A. Gramicidin Channels as Molecular Force Transducers. Biol. Skr. Vid. Sel. 1998, 49, 75–82.

(28) Brown, M. F. Modulation of Rhodopsin Function by Properties of the Membrane Bilayer. Chem. Phys. Lipids 1994, 73 (1-2), 159–180.

(29) Nielsen, C.; Andersen, O. S. Inclusion-Induced Bilayer Deformations: Effects of Monolayer Equilibrium Curvature. Biophys. J. 2000, 79 (5), 2583–2604.

(30) Ahn, T.; Chi, Y.-T.; Yun, C.-H. Effect of Nonlamellar-Prone Lipids on Protein Encapsulation in Liposomes. Macromol. Res. 2009, 17 (12), 956–962.

(31) Ahyayauch, H.; Villar, A. V.; Alonso, A.; Goñi, F. M. Modulation of PI-Specific Phospholipase C by Membrane Curvature and Molecular Order. Biochemistry 2005, 44 (34), 11592–11600.

(32) Dilger, J. P.; Benz, R. Optical and Electrical Properties of Thin Monoolein Lipid Bilayers. J. Membr. Biol. 1985, 85 (2), 181–189.

(33) Hou, J.; Cao, C.; Idrees, F.; Ma, X. Hierarchical Porous Nitrogen-Doped Carbon Nanosheets Derived from Silk for Ultrahigh-Capacity Battery Anodes and Supercapacitors. ACS Nano 2015, 9 (3), 2556–2564.

end of paper

Chapter 6

Optical manipulation

In the following section, a microfluidic lab-on-a-chip system is described. The setup used in the following experiments is explained in detail in Chapter 2.

6.1 Introduction

As mentioned earlier in Section 1.3, optical forces have been intensively used in applications in biophotonics, biology and biomedicine[149]. One of the most common optical manipulation systems are optical tweezers, where a single beam is utilized to trap and guide micro objects. The technique allows to study biochemical and biophysical processes, e.g. to investigate mechanical properties in cells and molecular interactions[150,151]. For example, optical tweezers have been used to study molecular motors, forces acting in single molecules, protein folding and protein elasticity and also single cells[152–154,161,163]. However, the technique has showed limitations related to heating of the sample which could potentially damage cells. This problem can be diminished by regulating the laser power, wavelength, and light exposure time for each sample[155,156,149].

During the past years, optical stretcher devices have also gained great attention. This technique uses a counter-propagating dual-beam which does not need to be focused in the samples, thus minimizing thermal damage. The possibility of stretching a dielectric micro object using two counter-propagating laser beams was demonstrated for the first time in works of J. Guck[34]. Since then, numerous biological studies using optical stretcher devices have been performed. Examples are studies of the viscoelasticity of blood during cell differentiation[157], studies of mechanical properties in lipid bilayers such as elasticity, as well as investigations of thermodynamic effects in the deformability of phospholipid membranes[158–160]. In addition, optical stretcher devices have also been used as a cell-marker, where the deformation of cancer cells was investigated[162].

Single-cell investigations require very low consumption of samples in the nanoliter to microliter range. In this sense, optofluidic systems have been widely used for performing studies of cells providing good handling and controlling of small samples. These systems give the possibility of transporting cells to specific regions or to exchange the liquid environment of cells as well as to improve the cell trapping efficiency[164,165]. Different optical stretcher devices merged with microfluidic systems have been presented in the literature. For example, devices composed by two optical fibers mounted opposite to each other in a SU-8 photoresist surface on a glass substrate, with a squared glass capillary to transport the samples[166]. Limitations of these devices, related to optical fiber alignment and low trapping efficiency, have been improved later on. For example, a device consisted of two glass substrates which have been asymmetrically etched to improve the alignment of the optical fibers and to increase the efficiency of the trapping[167]. In addition, femtosecond laser micromachining has been also used for the fabrication of optofluidic systems, where optical waveguides and microchannels are integrated in a silica glass substrate[168,169]. In previous works of M. Matteucci[69], a low-cost optofluidic device was fabricated via injection molding in a specific polymer. The microfluidic system was designed with a two-layer technology where the fiber grooves were positioned on a lower horizontal level with respect to the microchannels and perpendicular to the flow direction. The rectangular cross section and size of the fiber grooves were optimal for the fiber housing, providing a precise alignment of the optical fibers in the system.

In section 6.2, a new generation of the optical trapping device is described and compared with the former generation[69].

6.2 Optical two-beam trap in a polymer microfluidic chip

The following manuscript shows the advantages of a low-cost polymer microfluidic system able to efficiently trap, hold and to exchange the local environment of a trapped biological object. In this work, a three-layer microfluidic device was fabricated via polymer injection molding. The device consisted of a Y-shaped microchannel and had two optical fibers positioned perpendicular to the flow direction at the bottom part of the chip. The structure of the microchip provided horizontal hydrodynamic focusing of particles (cells flow in the center of the channel), and vertical focusing (cells flow in the focus line of the two optical fibers).

As mentioned in Chapter 2, this work was part of a collaborative expertise where Darmin Catak, Brian Bilenberg, Marco Matteucci, Anders Kristensen and Kirstine Berg-Sørensen designed and fabricated the device. UV lithography and injection molding were performed to fabricate the device, optical microscopy for its characterization, thermal pressure bond-

ing for sealing the microchip and an optical experimental trapping setup (described in section 2.2) for the performance of the trapping experiments. My contribution to this work was the thermal bonding of the chip and mounting the fibers together with Rodolphe Marie (associate professor, DTU Nanotech), the optical trapping experiments, data and image analysis and contributions writing the paper in sections 2.1.1, 2.1.3, 4, 5.1.

Previous attempts to bond the microchip as well as the performance of control experiments to analyze experimental problems, were also a key factor for the final designed protocol where the microchip was sealed via thermal bonding (former attempts for bonding the chip are described in section 2.2). Furthermore, prior approaches for performing the optical trapping experiments were also fundamental for the final optical trapping experiments, leading to a better control of the flow in the microchannels.

6.2.1 Espina Palanco, Marta; Catak, Darmin; Marie, Rodolphe; Matteucci, Marco; Bilenberg, Brian; Kristensen, Anders; Berg-Sørensen. Article submitted 2016.

beginning of paper

Optical two-beam trap in a polymer microfluidic chip

Marta Espina Palanco[a], Darmin Catak[b], Rodolphe Marie[b], Marco Matteucci[b], Brian Bilenberg[c], Anders Kristensen[b], Kirstine Berg-Sørensen[a,*]
[a]DTU Physics, Technical University of Denmark, 2800 Kgs Lyngby, Denmark
[b]DTU Nanotech, Technical University of Denmark, 2800 Kgs Lyngby, Denmark
[c]NIL Technology, Diplomvej 81, 2800 Kgs Lyngby, Denmark

Abstract. An optical two-beam trap, composed from two counter propagating laser beams, is an interesting setup due to the ability of the system to trap, hold, and stretch soft biological objects like vesicles or single cells. Because of this functionality, the system was also named "the optical stretcher" by Jochen Guck, Josep Käs and co-workers some 15 years ago. In a favorable setup, the two opposing laser beams meet with equal intensities in the middle of a fluidic channel in which cells may flow past, be trapped, stretched, and allowed to move on, giving the promise of a high throughput device. Yet, single beam optical traps, aka optical tweezers, by far outnumber the existing optical stretchers in research labs throughout the world. The ability to easily construct an optical stretcher setup in a low-cost material would possibly imply more frequent use of the optical stretching technique. Here, we will outline the design, the production procedures, and results obtained in a fiber-based experimental setup built within an injection molded microfluidic polymer chip. The microfluidic chip is constructed with a three layer technology in which we ensure both horizontal and vertical focusing of the cells we wish to trap, thereby preventing too many cells to flow below the line of focus of the two counter propagating laser beams that are positioned perpendicular to the direction of flow of the cells. Results will be compared to that from other designs from previous work in the group.

Keywords: optical trapping, fiber-based optical trap, polymer injection molding, hydrodynamic focusing.

*Kirstine Berg-Sørensen, kirstine.berg-sorensen@fysik.dtu.dk

1 Introduction

An optical stretcher setup, most successfully combined with microfluidics,[1–5] is a versatile tool for measurement of the elastic properties of a single cell, often expressed as the optical deformability of the cell in question. The optical deformability has been demonstrated as a signature of cancer and of metastatic potential,[6,7] and the optical stretcher has also been employed in investigations of mechanical properties of stem cells.[8] Different strategies for the actual design of an optical stretcher experiment have been presented in the literature, ranging from the very simple "open" setup in which optical fibers are aligned against e.g a glass capillary,[1] to microfluidic versions that are more apt for high throughput investigations. This includes systems using commercial optical fibers, for example a setup based on a commercial square capillary in glass as the microfluidic channel, positioned in SU-8 structures modified by standard photolithography that at the same time ensures fiber-alignment,[2] designs made in polymer materials[3] and also designs in which the optical field is complemented by a sound wave.[9] An alternative strategy is to couple laser light into waveguides that may be written in silica by femto-second laser pulses[4,10] or in polymethylmethacrylate (PMMA).[11] The silica device also has included the addition of a sound wave to preposition the cells to trap.[12,13] The benefit of a solution based on waveguides is an inbuilt alignment of the two counterpropagating light beams.

Yet, in the biophysics community, optical trapping in most cases involve the single beam optical trap obtained by a strongly focused Gaussian beam, aka optical tweezers, as first suggested by Arthur Ashkin.[14] With standardized

experimental setups for optical stretchers, based on low-cost polymer microfluidic systems, we believe, however, that optical stretchers may also be more widely used. This paper describes in detail our most recent attempt to design, injection mold and assemble such a system. We will discuss the capability of this latest optofluidic system to study mechanical properties of single cells subject to different environments through demonstrations of the ability of the system to allow for an exchange of the fluid surrounding a trapped particle.

2 Materials and methods

The optical trapping experiments were performed with a customized setup, centered around an inverted optical microscope (Leica DMI3000B) equipped with a CCD camera (Thorlabs DFC420M), and a microfluidic polymer system (Cyclic Olefin Copolymer TOPAS polymer 5013) to be described in detail below. The microfluidic chip has two single-mode fibers (AFM Technologies FOP-64-L-5-H64-22) connected via standard fiber connectors to two 1064 nm fiber-coupled diode lasers (Lumics LU1064M450-1006N10A), a four-channel Fluigent micropump (MFCS-EZ, 0-65 mbar) and custom-written LabVIEW software. The pressure driven pump was connected to the microfluidic system via silicone tubes of diameter 1.5 mm and around 50 cm of length (VWR ML94231A). All the experiments presented in this work were performed with 5 μm spherical polystyrene microparticles (Fluka; 79633; 10% solid wt content) mixed in water at 1:4 volume ratio.

2.1 Design considerations

2.1.1 Design of the chip

The microfluidic system is based on two parts: the top part (lid B) contains inlets/outlet ports with dimensions of standard LUER fittings, while the bottom part of the device (lid A) contains the microchannels (Figure 1). The top part is based on a standard configuration developed for polymer injection molding of microfluidic lab-on-chip systems,[15] whereas the outline of the channels and fiber grooves in the bottom part was based on our experiences from a previous design.[16]

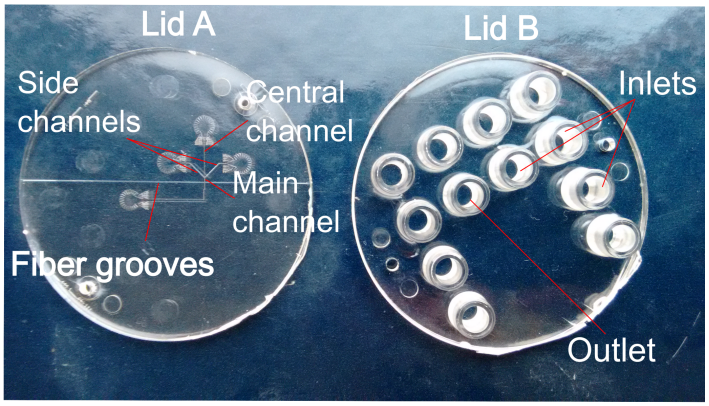

Fig 1 Microchip composed by two part: lid A and lid B. Lid A contains three inlets: Two side channels and a central channel that merge to form one main liquid channel. The fiber grooves are located perpendicular to this main channel. Lid B contains inlets/outlet ports. After mounting the fibers in lid A, the two parts are assembled to form a tightly sealed microfluidic system easily connected to a pumping system through the LUER connectors in lid B.

To ensure horisontal hydrodynamic focusing, a three inlets structure was chosen. This ensures that cells flow mainly in the center of a main liquid channel. In the vertical direction, a shallower inlet channel assists in vertical positioning of the particles at the focus line of the two laser beams (Figure 2a), oriented perpendicular to the direction of the flow of the particles. Thus, ideally, when the three inlet-streams are mixed, as long as the flow velocity field reaches a reasonable minimum flow speed, cells or particles will partially sediment to preferentially flow through this focus line, with equal distance from the two fiber ends (Figure 2b). At the flow speeds and viscosity similar to that of water applicable here, the contribution from lift forces is at max of order a few per cent,[17] and our estimate for the good flow speed is based on simple considerations of the force of bouyancy (see appendix for details). For 5μm diameter polystyrene particles, this velocity is estimated to be 4.2 μm/s, corresponding to 4.22 $10^{-5}\mu\ell$/s.

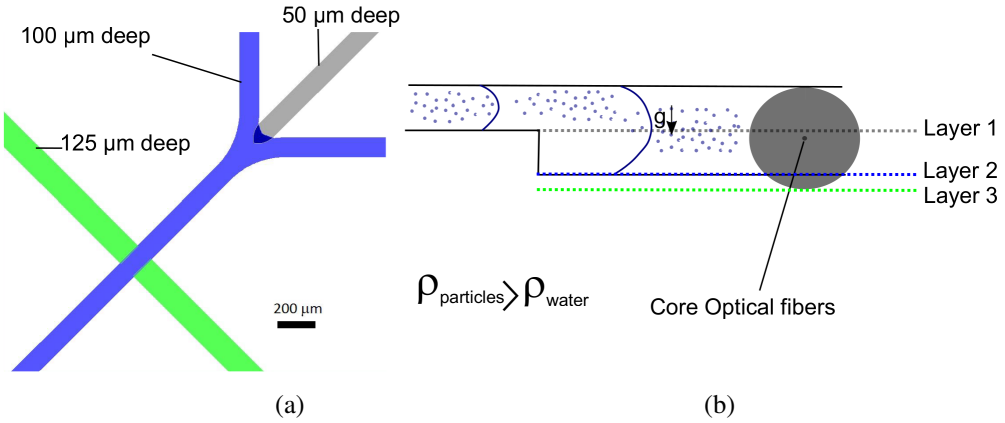

Fig 2 Hydrodynamic focusing in a three layer technology microchip (a) Top view of the layers channel. A central channel (grey) is located on a top layer with respect the two side and main channels (blue). Fiber grooves are located on a third layer (green) (b) Lateral view of the layers in the chip. Particles or cells flowing in the central channel located at the top, i.e., at and above layer 1, are directed by a combination of partial sedimentation by gravity and fluidic lift into the main channel, i.e., at and above layer 2, to the focus line of the two optical fibers positioned in the grooves perpendicular to the main channel; fibers grooves are at and above layer 3.

The inlet/outlet ports in lid B include the two side channels of a nominal cross-section of 100 μm x 100 μm with 3250 μm of length each before the merging point, and a central channel that is 100 μm wide and 50 μm deep, 4350 μm long before the point in which they merge. The three channels merge into a main channel with a nominal square cross-section of 100 μm $\times$ 100 μm, 1400 μm long (Figure 2a). In the middle of the main channel, at around 620 μm from the point where the three channels meet, two grooves of nominal cross-section of 125μm $\times$ 125 μm for housing the optical fibers cross the main channel. Thus, two optical fibers of 125 μm diameter may be positioned inside the grooves, preferably with an approximate distance between the end of the fibers of 100 μm. Near the outlet, the main liquid channel is wider, to reduce hydraulic resistance.

As argued in earlier work, the square geometry of the fiber grooves is well suited for alignment of fibers, reducing their later movement, reducing leaking and favouring fiber gluing.[16]

2.1.2 Injection molded chips

The injection molded chips were produced based on a multilayer stamp (shim) for injection molding, fabricated with standard cleanroom techniques.[18–20] The first step is to fabricate the Silicon master. The silicon master for lid A, Fig. 1, was produced by standard UV lithography and deep reactive ion etching of a 150 mm diameter silicon wafer. The lid A channel layout with three channel depths were made with three UV, 365 nm wavelength, lithography steps performed on a Sss MA/BA6 UV contact aligner followed by deep reactive ion etching with an STS Bosch process tool, Advanced

Silicon Etcher STS MESC Multiplex ICP. The channel layout and depths are shown in Fig. 2. The next step is the fabrication of the Nickel shim. The Nickel shim for injection molding of lid A was made by direct nickel plating on the silicon master. A 90 nm thick nickel vanadium, NiV, layer was sputtered onto the master surface with a Lesker sputtering tool. Subsequently, the nickel was plated on top of the seed layer in a Technotrans microform.200 nickel electroplating tool. The thickness of the final nickel shim was 330 μm. Finally, the nickel shim was trimmed into the right format for the injection molding tool by laser cutting while protecting the nickel shim surface with photoresist. The photoresist was cleaned off the nickel shim prior to injection molding. The final step is the injection molding step. Both lid A and lid B parts were injection molded in the biocompatible cycloolefin copolymer Topas 5013L-10 (Topas Advanced Polymers, US). Topas pellets were pre-dried in order to ensure optimal rheological performance during injection molding, which was done on a modified Engel Victory 80/45 Tech, that allows for applying variothermal processes. The maximum tool clamping force on the specific machine is 450 kN. To ensure an excellent pattern replication fidelity during injection molding, both a conventional isothermal and a variothermal process were applied: For Lid B, the nickel shim was kept at 120°C (i.e. slightly above the glass transition temperature, T_g, of the Topas) during the cavity filling injection step, whereas for Lid A, the variothermal process was used, starting at 145°C and rapidly cooling down to under 135°C. The variothermal process allows us to get the best possible filling without defects on the edges that would otherwise hamper the subsequent bonding. In both cases, the injection step lasts around one and a half minute. The polymer melt temperature at the nozzle was set to 250°C and a holding pressure of 1150 bar was applied during the subsequent cooling below T_g.

2.1.3 Mounting the fibers and bonding the chip

After the chip fabrication, two optical fibers were prepared and inserted into the grooves (lid A). Different procedures for bonding the chip has been investigated, simple tape-bonding by double-sticky tape and UV assisted thermal bonding, the latter is described here. In order to prevent misalignment during the bonding process, two small drops of Epoxy glue (Casco 2806) were adhered to the fiber grooves on top of the fiber, 2 mm from the main liquid channel. As a next step, lid B was chemically activated by placing it in UVI light for 2 minutes and then rapidly positioned on the top of lid A by carefully matching the inlets of lid A with the ports in lid B. UV assisted thermal bonding is performed in a hydraulic press (P/O/Weber, Germany) at 125 °C and 5 bar after both polymer parts are exposed to a 400W mercury lamp (Dymax). The glass transition of TOPAS 5013 is 130 °C.[21] The coefficient of linear thermal

expansion of TOPAS polymer is around 0.6 $10^{-4}K^{-1}$ whereby heating from room temperature to 125 °C theoretically results in fiber ends being displaced by up to 20 μm along the fiber grooves.

In order to reduce the polymer expansion and therefore the misplacement of the optical fibers, the microchip was placed in the pressure bonding machine while the pressure plates were still cold. After that, first 5 bar pressure was applied and secondly, the temperature was set to 125 °C. When the system reached 125 °C, the chip was left in the bonding press for approximately 10 minutes.

3 Characterization of Si master, shim and microfluidic chips

The Si-master, the shim and the final microfluidic chips are inspected by optical microscopy and channel depths in the Si-master are measured by mechanical profilometry. The latter provided depths of the three layers of 49.5 μm, 99.7 μm and 123.5 μm respectively. Microscopy images of the Si-master and the shim are shown in Fig. 3.

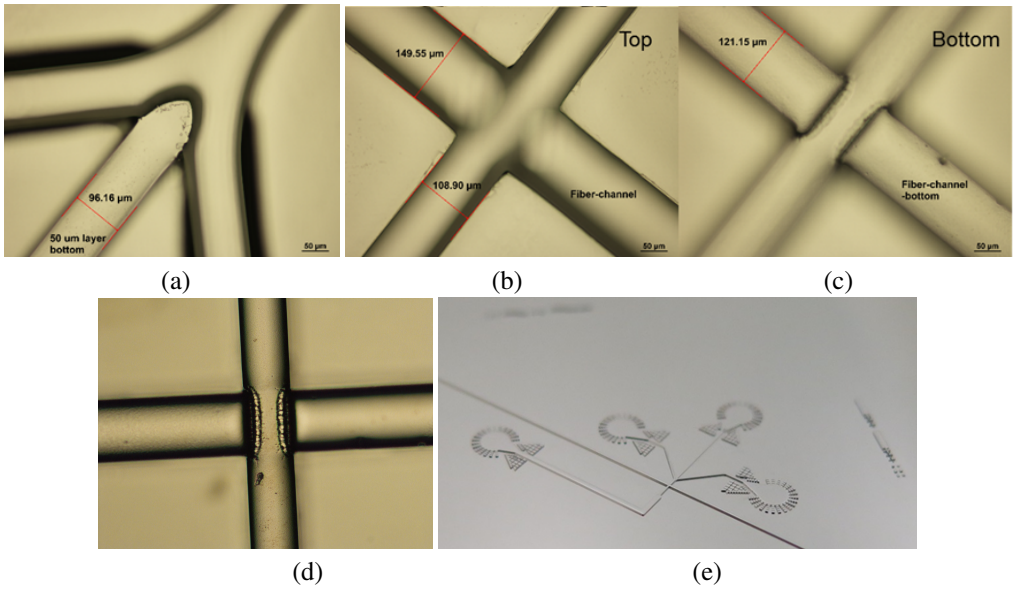

Fig 3 Optical microscopy images of the Si-master, and the shim. Part (a) shows the Si-master at the position where the three channels of the inlet structure meets, and at the top (b) and bottom (c) of the position where the main liquid channel crosses the fiber grooves. Part (d) is an image of the Ni-shim, focused at the bottom of the liquid channel, and illustrates that the etch-marks in the Si-master, visible in part (c), are carried over to the shim and will also be visible in the final injection molded chips. Panel (e) shows a close-up photograph of the Ni-shim.

4 Results: Optical trapping experiments

4.1 Improved trapping efficiency

Video 4 shows the trapping of several particles, each at different time, in the space between the two optical beams positioned perpendicular to the direction of the flow. As can be seen in the plane view, in several instants a high

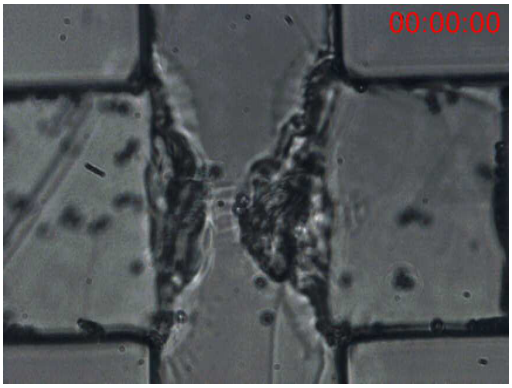

Video 4 Trapping of several particles in the main channel between two optical beams possitioned perpendicular to the direction of the flow. The debris in front of the fiber that blurs the image was unfortunately impossible to remove, yet we preferred to use this chip as fiber ends are positioned particularly close, as will be discussed further below. http://dx.doi.org/doi.number.goes.here

fraction of the particles flows in the focus plane of laser beam, i.e. 4 particles out of 5 at 00:00:02. The high fraction of focused particles above the laser beam line allowed to efficiently trap them at high rate, up to 15 particles in 25 seconds. Additionally, the precise alignment of the fibers resulted in a highly focused optical power, i.e. to the center of the main channel for an efficient trapping of particles.

4.2 Fluid exchange while a bead is trapped

Figure 5 displays a time series during the process of fluid exchange while a particle is trapped.

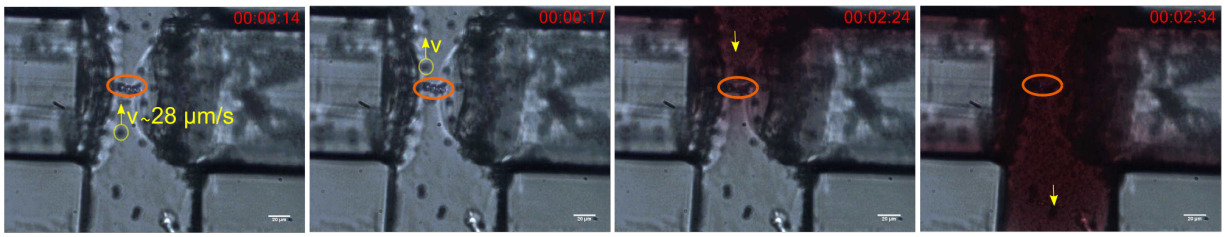

(a) (b) (c) (d)

Fig 5 Time series during the process of exchanging the fluid while three particle are trapped. In (a) and (b) three particles are trapped (orange) in the main channel, between the two optical fibers. In the background, a yellow arrow indicates the direction and velocity of unfocused particles flowing in a laminar flow with a velocity 28 μm/s (c) The direction of the fluid is changed (yellow arrow) visualizing the entrance of a red dye to the space where the particles are still trapped (orange). (d) The liquid in the environment of the trapped particles has been complety exchanged.

Figs. 5a and 5b show three trapped particles in a flow with an approximate velocity of 28 μm/s. Notice that in order to exchange the fluid around a trapped particle, the flow direction needs to be inverted (Fig 5c). Therefore, the pressure at the outlet was gradually decreased to zero followed by an increase of the pressure in the central inlet and a somewhat lower pressure in the two side channels. In order to better visualize changes of the direction of the fluid and

also the exchange of liquid around the trapped particles, a red dye was used. Fig. 5c visualizes the entrance of the red color dye in the place where the particles are still trapped and in Fig. 5d, the liquid in the environment of the trapped particles has been completely exchanged.

5 Discussion and conclusion

5.1 Comparison with other devices

The new design of a polymer optofluidic device shows clear advantages compared with the former generation.[16]

First, the short length of the main channel compared with the first generation chip implies that the pressure drop at the desired flow speed is lower. During the experiments we found that this fact facilitated a precise control of flow speed and flow direction in the channel. Thereby, experiments requiring exchange of the liquid surrounding a trapped cell become more feasible, opening new capabilities for this optical trapping setup for further applications to investigate cell responses.

Second, the three layer technology that assists hydrodynamic focusing ensures that a high fraction of particles flow in the focus plane of the counter propagating laser beams, thus allowing to trap 15 cells in 25 seconds. As comparison, in the first generation microfluidics-devices of reference 16, an experiment with fiber ends deliberately placed equally far apart for direct comparison, results in a fraction of around 5/60 flowing in the focus plane (video 6).

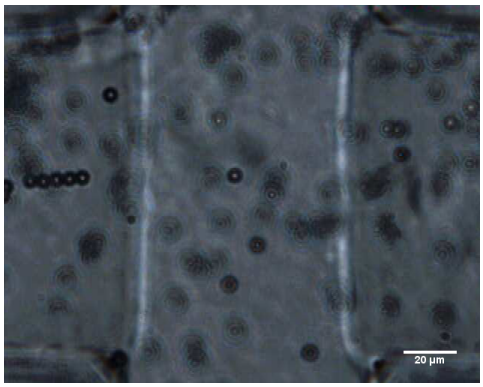

Video 6 First generation microfluidics-devices from previous work.[16] Trapping of several particles in the main channel between two optical beams possitioned perpendicular to the direction of the flow. In the background, a high fraction of particles flowing out of the focus line of the two laser beams are visible. http://dx.doi.org/doi.number.goes.here

Due to the mechanical traction applied during the sealing of the chip, we observed, however, the final distance between the ends of the two optical fibers as large as 300 μm. This deformation could be explained by a possible surface modification of lid A during the bonding procedure. When sealing the chip, lid A expands thermally, and through the combined action of thermal expansion and applied pressure, lid A may sink into the luer cavities of lid B causing also a deformation of the fiber grooves. In the previous generation device, the injection molded part of the chip contained both liquid channels, fiber grooves and LUER ports, and the chip was sealed either thermally with a thin disk or, even simpler, by pressure bonding a foil prepared with pressure assisted glue. In spite of this undesired movement of the fibers, the preliminary results presented here with polystyrene beads indicate the capability of the chip to trap a higher fraction of cells, compared with the device discussed in reference 16.

Compared to devices in which alignment of the laser beams is ensured by either direct laser writing of waveguides in an all glass device,[4,10,12] or by DUV writing in a polymer device,[9] delivery of light by optical fibers enables a high laser intensity for trapping and stretching even with, say, a fiber-coupled diode laser of relatively low power (200-500 mW). Laser written or DUV written waveguides have, compared to the optical fiber, a high loss, both from propagation losses – the reported values are 0.66 dB/mm in the polymer and 0.9 dB/cm in the glass chips – and from coupling losses.

In earlier work, we have also investigated the applicability of sound waves to ensure that cells and beads to trap flow at the height of the focus line between the two trapping laser beams,[9,12,13] so-called acoustophoretic prefocusing. With acoustophoretic prefocusing, one can thus avoid the situation often encountered with optical stretcher devices that each new cell type requires a different position of the counter propagating light beams with respect to the floor of

the liquid channel.[2] The ability to prefocus the cells is therefore a clear advantage. Unfortunately, material parameters of polymers that may be injection molded are not well suited for acoustophoresis,[22] and therefore hydrodynamic focusing, both in the horisontal and the vertical direction, was explored in the chip design discussed here.

5.2 Conclusion and outlook

As demonstrated by the microfluidic chip discussed in this manuscript, as well as the microfluidic system we presented earlier, in reference 16, microfluidic chips of polymer materials, and produced by production ready methods, are readily available for assembly of optical stretcher devices. The assembly still relies on post-processing steps, and there is still work to do to optimize the procedures that ensure a tight sealing and thereby ensures chips that work similarly for each device prepared.

Nevertheless, the preliminary results presented in the manuscript illustrates that the microfluidic system is available for trapping and stretching experiments in which liquid exchange may change the local environment of the trapped cell. Thereby the stretching response of the same cell, subject to different liquids, may be investigated. We imagine for example experiments that investigate membrane-curvature dependence of membrane-proteins in a trapped cell.

Appendix: Sedimentation-assisted vertical positioning

The sedimentation-assisted positioning may be estimated based on standard equations for Stokes drag. For particles of density ρ_{bead} and radius r, a simple estimate of the required flow speed v_x along the flow channel for hydrodynamic focusing to the position of the fiber cores, is based on the sedimentation time over the distance h in the vertical z-direction.

$$v_x = \frac{s_x}{t},\ t = \frac{h}{v_z},\ \text{and}\ v_z = \frac{4\pi r^3}{3}(\rho_{\mathrm{bead}} - \rho_{\mathrm{fluid}})g\frac{1}{6\pi\eta r} \equiv \frac{F_{\mathrm{sed}}}{6\pi\eta r}. \tag{1}$$

Here, ρ_{fluid} and η are the density and viscosity of the fluid and g is the acceleration of gravity. For s_x we use the distance between the merging point of the three inlet channels and the fiber grooves, $s_x \simeq 620\mu$m, and for h the distance from the top of the microfluidic channel to the position of the fiber cores, $h \simeq 62\mu$m. We also introduced the notation F_{sed} for the sedimentation force.

In order to estimate the corresponding lift force, we apply the result derived by Saffman,[17] F_{lift},

$$F_{\mathrm{lift}} \simeq 6.46\sqrt{\eta\rho_{\mathrm{fluid}}}v_0 r^2\sqrt{\left|\frac{\partial v_x}{\partial z}\right|}, \tag{2}$$

where v_0 is the relative velocity between particle center and surrounding fluid. The derivative $\partial v_x/\partial z$ may be estimated from the standard expression for Poisseuille flow in a circular tube of radius R and length ℓ,

$$v_x(y,z) = \frac{\Delta p}{4\eta\ell}(R^2 - y^2 - z^2); \quad \frac{\partial v_x}{\partial z} = -\frac{\Delta p}{2\eta\ell}z$$

giving an overestimate for the order of magnitude for the derivative of $|\partial v_x/\partial z| \sim \Delta p R/(2\eta\ell)$. Similarly, for an order of magnitude estimate, we use a typical pressure-drop of order 0.2 mbar, ℓ of order 4000 μm, R of 50 μm, r of 2.5 μm, and the density and viscosity of water. For v_0, the value of v_x in Eq. (1) provides an overestimate. This allows us to evaluate the ratio of lift force to sedimentation force

$$\frac{F_{\mathrm{lift}}}{F_{\mathrm{sed}}} \simeq \frac{6.46}{6\pi}\frac{r s_x}{\eta h}\sqrt{\frac{\Delta p \rho_{\mathrm{fluid}} R}{2\ell}} \tag{3}$$

which provides an overestimate of the ratio between lift and sedimentation of 9.6 per cent.

Acknowledgments

We are grateful to the support provided by the PolyNano network, allowing for the development and production of the microfluidic chip.

References

1 J. Guck, R. Ananthakrishnan, H. Mahmood, *et al.*, "The optical stretcher: A novel laser tool to micromanipulate cells," *Biophys. J.* **81**(2), 767 – 784 (2001).

2 B. Lincoln, S. Schinkinger, K. Travis, *et al.*, "Reconfigurable microfluidic integration of a dual-beam laser trap with biomedical applications," *Biomed. Microdevices* (2007).

3 F. Lautenschlaeger and J. R. Guck, "Microfluidic integration of high power dual-beam laser traps for cell mechan-

ical measurements," in *IEEE ISOT: 2009 International Symposium on Optomechatronic Technologies*, 419–422 (2009).

4 N. Bellini, K. Vishnubhatla, F. Bragheri, *et al.*, "Femtosecond laser fabricated monolithic chip for optical trapping and stretching of single cells," *Opt. Express* **18**(5), 4679–4688 (2010).

5 T. Yang, F. Bragheri, and P. Minzioni, "Review: A comprehensive review of optical stretcher for cell mechanical characterization at single-cell level," *Micromachines* **7**, 90 (2016).

6 J. Guck, S. Schinkinger, B. Lincoln, *et al.*, "Optical deformability as an inherent cell marker for testing malignant transformation and metastatic competence," *Biophys. J.* **88**, 3689–3698 (2005).

7 T. W. Remmerbach, F. Wottawah, J. Dietrich, *et al.*, "Oral cancer diagnosis by mechanical phenotyping," *Cancer. Res.* **69**, 1728–1732 (2009).

8 A. E. Ekpenyong, G. Whyte, K. Chalut, *et al.*, "Viscoelastic properties of differentiating blood cells are fate- and function-dependent," *PLOS ONE* **7** (2012).

9 M. Khoury, R. Barnkob, L. L. Busk, *et al.*, "Optical stretching on chip with acoustophoretic prefocusing," *Proc. SPIE* **8458**, 84581E (2012).

10 N. Bellini, F. Bragheri, I. Cristiani, *et al.*, "Validation and perspectives of a femtosecond laser fabricated monolithic optical stretcher," *Biomed. Opt. Express* **3**(10), 2658–2668 (2012).

11 M. Khoury, C. Vannahme, K. T. Sørensen, *et al.*, "Monolithic integration of DUV-induced waveguides into plastic microfluidic chip for optical manipulation," *Microelectron. Eng.* **121**, 5–9 (2014).

12 G. Nava, F. Bragheri, T. Yang, *et al.*, "All-silica microfluidic optical stretcher with acoustophoretic prefocusing," *Microfluid. Nanofluid.* **19**, 837–844 (2015).

13 T. Yang, F. Bragheri, G. Nava, *et al.*, "A comprehensive strategy for the analysis of acoustic compressibility and optical deformability on single cells," *Scientific Reports* **6**, 23946 (2016).

14 A. Ashkin and J. Dziedzic, "Optical trapping and manipulation of viruses and bacteria," *Science* **235**, 1517–1520 (1987).

15 "PolyNano - strategic research center in precision and nano-scale polymer mass replication of biocchips; www.polynano.org."

16 M. Matteucci, M. Triches, G. Nava, *et al.*, "Fiber-based, injection-molded optofluidic systems: Improvements in assembly and applications," *Micromachines* **6**, 1971–1983 (2015).

17 P. G. Saffman, "The lift on a small sphere in a slow shear flow," *J. Fluid Mech.* **22**, 385–400 (1965).

18 P. Utko, F. Persson, A. Kristensen, *et al.*, "Injection molded nanofluidic chips: Fabrication method and functional tests using single-molecule dna experiments," *Lab on Chip* **11**, 303–308 (2011).

19 S. Tanzi, P. F. Østergaard, M. Matteucci, *et al.*, "Fabrication of combined-scale nano- and microfluidic polymer systems using a multilevel dry etching, electroplating and molding process," *J. Micromech. Microeng.* **22**, 115008 (2012).

20 M. Matteucci, T. L. Christiansen, S. Tanzi, *et al.*, "Fabrication and characterization of injection molded multi level nano and microfluidic systems," *Microelec. Eng.* **111**, 294–298 (2013).

21 "Topas advanced polymers, cyclic olefin copolymer (coc); http://www.topas.com/company/news/topas-advanced-polymers-cyclic-olefin-copolymer-coc-elastomer-earns-fda-food-contact."

22 H. Bruus, *Theoretical Microfluidics*, Oxford University Press, New York (2008).

Marta Espina Palanco is a Ph.D. student at the Technical University of Denmark. She has authored three published journal papers. Her current research interests include Surface Enhanced Raman Spectroscopy, biosensor and optical trapping.

Darmin Catak is a research assistant at the Technical University of Denmark. His current research interests include tools and techniques for producing injection molded polymer chips.

Rodolphe Marie is Associate Professor at the Technical University of Denmark. He has authored 32 journal papers and 24 conference papers. His current research interests include micro- and nanofluidics for manipulation of single cells and single DNA molecules, and providing stable microfluidic systems for these investigations based on injection molded polymer chips.

Marco Matteucci is Associate Professor at the Technical University of Denmark. He has authored 8 journal papers and 8 conference papers. His current research interests include tools and techniques for producing injection molded polymer chips.

Brian Bilenberg is CTO at NIL Technology. His expertise include tools and techniques for Nano-Imprint Lithography.

Anders Kristensen is full Professor at the Technical University of Denmark. He has authored above 250 journal papers and several book chapters. He is heading the optofluidics research group at DTU Nanotech with current research interests in plasmonics, precise polymer injection molding with nanometer scale structures.

Kirstine Berg-Sørensen is Associate Professor and Head of Studies at the Technical University of Denmark. She has authored 43 journal papers and written three book chapters. Her current research interests include optical trapping, simple microfluidic systems, optical methods for investigations of fluidic flow and the application of such methods in connection with medical questions.

List of Figures

3 Optical microscopy images of the Si-master, and the shim. Part (a) shows the Si-master at the position where the three channels of the inlet structure meets, and at the top (b) and bottom (c) of the position where the main liquid channel crosses the fiber grooves. Part (d) is an image of the Ni-shim, focused at the bottom of the liquid channel, and illustrates that the etch-marks in the Si-master, visible in part (c), are carried over to the shim and will also be visible in the final injection molded chips. Panel (e) shows a close-up photograph of the Ni-shim.

4 Trapping of several particles in the main channel between two optical beams possitioned perpendicular to the direction of the flow. The debris in front of the fiber that blurs the image was unfortunately impossible to remove, yet we preferred to use this chip as fiber ends are positioned particularly close, as will be discussed further below. http://dx.doi.org/doi.number.goes.here

5 Time series during the process of exchanging the fluid while three particle are trapped. In (a) and (b) three particles are trapped (orange) in the main channel, between the two optical fibers. In the background, a yellow arrow indicates the direction and velocity of unfocused particles flowing in a laminar flow with a velocity 28 μm/s (c) The direction of the fluid is changed (yellow arrow) visualizing the entrance of a red dye to the space where the particles are still trapped (orange). (d) The liquid in the environment of the trapped particles has been complety exchanged.

6 First generation microfluidics-devices from previous work.[16] Trapping of several particles in the main channel between two optical beams possitioned perpendicular to the direction of the flow. In the background, a high fraction of particles flowing out of the focus line of the two laser beams are visible. http://dx.doi.org/doi.number.goes.here

List of Tables

end of paper

Chapter 7

Concluding remarks and perspectives

This PhD project covers different optical techniques: the single molecular spectroscopic techniques of Raman Spectroscopy and Surface Enhanced Raman Spectroscopy, and the single cellular manipulation technique of optical trapping.

Resonances between optical fields and surface plasmons allow to concentrate fields in nanometer scaled volumes and, at the same time, provide extremely high field intensities, having a great potential for improving the performance of Raman spectroscopy. Silver and gold exhibit plasmon resonances in the visible-NIR range, thus being very appropriate for performing SERS with NIR excitations while the plasmon resonance of Aluminum often occurs in the UV range. However, in this thesis, we have shown the possibility of enhancing Raman signals with NIR excitation using aluminum island films as SERS substrates. It seems that the enhanced confined local fields are not only influenced by the dielectric constant properties of the metal, but also strongly influenced by the geometry of the plasmonic nanostructures. Thus, control of the geometry of plasmonic structures, as well as their tendency to aggregate, is of key importance in further development of plasmon supported methods.

An eco-friendly, simple, fast, low-cost and sensitive method for the development of plasmonic metal nanostructures is the use of natural molecules as reducing agents of silver salts. In this PhD project, we explored the formation of synthesized silver nanoparticles, of around 10-300 nm, using pineapples and oranges. The use of oranges resulted in the formation of spherical isolated particles and small aggregations with large inter-particle distance, while the use of pineapples resulted in the formation of nanoparticles with sharp edges. Different sizes and morphologies of the formed nanoparticles showed a high dependency on the extract used. In contrast, the amount

of the extract used and the exposure to light did not influence the geometry. The performance of SERS with near infrared excitation light resulted in modest enhanced Raman signals, probably due to a poor aggregation behavior.

Surface enhanced Raman studies of biologically relevant molecules in their complex environment, such as in plants, require the delivery of plasmonic nanostructures into the samples. In this project, we have demonstrated the possibility of incorporating plasmonic nanostructures in an intact fresh plant, i.e., *in-situ* preparation, via the delivery of both metal salts and colloidal metal nanoparticles. On one hand, silver and gold nanoparticles were green synthesized in the extracellular space of onion layers, without fragmentation of the biological sample. The delivery of plasmonic nanostrucutres on the extracellular space of intact onion layers was possible via the uptake of silver salt solution in the plant. The plant cell provided an adequate chemical medium for the reduction of silver salts, a template for the growth of the nanoparticles in its cell wall and an optimal SERS template for performing Raman.

On the other hand, a new approach was the delivery of plasmonic nanosensors, i.e., silver nanoparticles, into intact plant tissues.The incubation of silver nanoparticles in an onion cell layer resulted in nanosensors settling down at the extracellular space of the tissue. The chemical affinity of sulfur molecules present in some plants, e.g. onion, towards silver nanoparticles provided enhanced Raman signals collected from the intrinsic molecules of the tissue. A pH-sensitive reporter molecule solution was added to the nanosensors in a way that when performing SERS on the tissue, Raman signals also provided pH values of the extracellular space of the plant. As an alternative for performing *in-vivo* Raman studies of plant leaves, we showed the possibility of using silver island films as SERS- substrates.

The second part of this PhD project involved the optimization of an optofluidic Lab-on-Chip system. A polymer injection molded microchannel was the key element of this setup. It consisted of a Y-shaped microchannel in a 3-layer design, with two optical fibers positioned perpendicular to the flow direction and at the bottom part of the chip. The particular structure of the microfluidic device was important for horizontal and vertical focusing of the particles at the focus line between the optical fibers. Moreover, the squared geometry and sizes of the fiber grooves provided optimal fiber housing, and thereby enabled aligned optical fibers in the system to deliver focused light in the middle of the microchannel. The design of the device efficiently increased its capability to trap numerous cells in short time, opening new possibilities for performing as an efficient sensor for studying mechanical properties of cells. In addition, the system showed the capability of exchanging the liquid environment of a trapped cell within 2.5 minutes, thus showing the potential of

this device for performing cellular studies. The low cost for the fabrication of the chips and fast production of the devices is beneficial for future studies of mechanical properties of single cells.

Overall, this project provided new insight into the chemical composition and physical parameters of plant cells as well as into building efficient optofluidic based-sensors from new materials and methods that have not been used before. The results from this PhD project can contribute to the development and design of new ideas and protocols for performing both Raman studies in intact plant leaves and optical manipulation techniques for investigating physiological and mechanical properties of soft cells, e.g. mammalian cells.

If given the opportunity to continue working with Raman and SERS spectroscopy for studying plant cells, I would consider next options:

- Raman spectroscopy can provide direct access to molecular structures and physiologically relevant chemical and physical parameters, such as pH-level, molecular- and ion-concentrations inside channels. As a next step, it would be very interesting to apply plasmonic nanosensors for measurements in small artificial and biological channels and pores to support our understanding of plant physiology.
- Performance of SERS for exploring the cytoplasmic space of intact plant cells. For that, the development of new ideas for how to bring the required nanostructures into the intracellular space are needed.
- A very helpful tool to assign Raman signatures would be creating a library where the Raman spectra of all the typical constituents present in a plant (or the most expected ones) are collected, thus, the identification of such signatures would be more efficient, simple and fast.
- It is very important to investigate the toxicity of silver nanoparticles. So far in our experiments, leaves did not show apparent destruction or necrosis, however Raman signatures suggested that the tissue was subjected to stress.
- A complementary technique of Raman spectroscopy is infrared spectroscopy. This technique could be applied in combination with Raman studies in plants in order to get a more holistic understanding, by providing molecular frequencies that Raman active molecules do not provide.

In the second part of the PhD project, we have shown a low-cost and efficient optical manipulation device. The device could be used for studying physiological properties

of cells subject to different local environments and different mechanical stress. As mentioned during this thesis, a key motivation for carrying out this part of the project was to investigate how the membrane-protein activity and membrane barrier properties are influenced by the membrane composition and the curvature of the membrane. In Chapter 6, we have explored how the activity of bR depends on the constituents of the membrane, e.g. when incorporating bR in a mixed matrix constituted by phospholipids and a polymer, the system pumps protons much more efficiently than a vesicle constituted by the pure polymer. In addition, the shifted vesicle size distribution for the mixed systems to lower diameters, suggested that the membrane curvature of the vesicle could affect the function of bR. In this way, it would be very interesting to trap a biomimetic cell with embedded bR, optically deform it, e.g. alter its curvature by stretching it, and thus, investigate how this affects the pumping of ions through the membrane. In order to perform these studies, it would be necessary to use a pH-reader, able to detect pH changes across the membrane. A problem that would need to be addressed is to make sure that bR is well incorporated in the membrane whereby, changes in proton pumping activity are due to curvature and not due to a non optimum incorporation of bR. Similarly, since bR only pumps protons actively in one direction, it would be necessary to ensure that the orientation of bR in the membrane is equal for each cell, to properly do comparisons. Thus several control experiments need to be addressed a priori.

Yeast Aquaporins were one of our alternative suggestions as the membrane protein, for analyzing mechanical properties of cells. It has been reported that the activity of the protein is increased in absence of the N terminal[20]. A way to explore these systems and thus, the role of the N terminal in the function of aquaporins would be to trap different yeast cells lines, i.e. with and without the relevant N terminus in the reporter molecule (the Aquaporin), and compare the protein activity in each case. Since larger transport of water will be reflected on higher cell volumes (if the osmolarity in the intracellular space is larger compared to the extracellular medium of the cells), the cell membrane could be the reader of the system. One of the problems that need to be addressed is that the membranes need to be soft enough to be able to change the volume and/or the deformability of the vesicles. Spheroplast of yeast cells are a good option.

In addition, the presented biomimetic systems could also be adapted to accomplish different goals. We have shown that the alteration of the kinetic motion of transported molecules, in this case the proton flux across the membrane, depends on the vesicle composition. This gives the possibility of creating a very fast and/or a very slow response, depending on the desired sensor function. If we aim for a fast

responsive biosensor which simultaneously provides a high response and a highly stable system, our results indicate that a mixed-compound membrane system based on lipids and polymer materials is to be preferred. Instead, if we aim for a bio-system able to retain the information and make use of it in this form, our results suggest that a polymeric membrane model system is the best choice. Moreover, if what we are looking for is a biosensor where the whole system can be tuned for different purposes (e.g. the release of a drug with a well-defined profile in time into a biological system), our results suggest adjusting the biosensor by all the different additives presented in our study until the requested time-dependency is achieved.

Yet, there are some limitations in the current setup which need to be addressed:

- The design of the chip was optimum for trapping 5 μm diameter polystyrene (density 1.05 g/cm^3) particles. The distance that the particles take before sedimentation, at certain velocity, was calculated according to these values. It may be convenient to create a device able to assist any kind of samples.
- In terms of bonding the chip, the flatness of both lids of the chip needs to be optimized, in order to ensuring a tight sealing. This would probably also improve the alignment of the optical fibers when thermally bonding the chip. Another way to avoid the misalignment of the optical fibers could be via modifying the design of the microfluidic system, were the inlet and outlet ports are far from the optical fiber grooves.
- Even if injection molding is a fast and low-cost procedure to fabricate chips, the final microchips always differed between them (at the microscale). Thus, an improvement of the procedure needs to be done to be able to reproduce exactly the same devices and thereby not alter their performance.
- Debris between the two optical fibers is often encountered. When mounting the fibers and bonding the chip a pressure is made on the step between the channel that may cause the rupture of the step if the latter is already weak. This is something that needs to be improved since even though it does not affect the trapping experiments, it does affect the quality of the images.

Bibliography

[1] H. Robert, J. Martyn, J. Allestry (**1665**). Micrographia, or, Some Physiological Descriptions of Minute Bodies Made by Magnifying Glasses: with Observations and Inquiries Thereupon. London: Printed by Jo. Martyn and Ja. Allestry, printers to the Royal Society.

[2] M. Pines (**1993**). Inside the Cell. United States: Diane Books Publishing Company.

[3] M. Luckner, B. Diettrich, (**1985**). Formation of cardenolides in cell and organ cultures of Digitalis lanata. In K. Neumann, W. Barz, E. Reinhard (Eds.), Primary and Secondary Metabolism of Plant Cell Cultures. Berlin: Springer.

[4] E. Reich, A. Schibli (**2008**). High-Performance Thin-Layer Chromatography for the Analysis of Medicinal Plants, New York: Thieme.

[5] Ch. Zidorn (**2008**). Plant chemosystematics. In: M. Waksmundzka-Hajnos, J. Sherma, T. Kowalska (Eds.), Thin layer chromatography in phytochemistry. Boca Raton;London New York: CRC Press.

[6] E. W. Tegelaar, J. W. DeLeeuw, C. Largeau, S. Derenne, H. R. Schulten, R. Müller, J. J. Boon, M. Nip, J. C. M. Sprenkels *J. Anal. Applies Pyrolisis*, **1989**, 15, 29–54.

[7] J. T. Alander, V. Bochko, B. Martinkauppi, S. Saranwong, T. Mantere. *Int J Spectrosc* **2013**, 1–36.

[8] R. Sozzani, W. Busch, E. P. Spalding, P. N. Benfey. *Trends Plant Sci* **2014**, 19, 304–310.

[9] N. K. Ravichandran, R. E. Wijesinghe, M. F. Shirazi, K. Park, S. Y. Lee, H. Yo. Jung, M. Jeon, J. Kim. *Journal of Spectroscopy* **2016**, 1–6.

[10] N. Gierlinger, M. Schwanninger. *Journal of Spectroscopy* **2007**, 21, 69–89.

[11] K. Kneipp. *Phys. Today* **2007**, 60, 40–46.

[12] S. Ahmed, M. Ahmad, B. L. Swami, S. Ikram. *Journal of Advanced Research* **2016**, 7, 17–28.

[13] R. Foldbjerg, H. Autrup. *Arch. Bas. App. Med.* **2013**, 1, 5–15.

[14] K. Kulthong, R. Maniratanachote, Y. Kobayashi, T. Fukami, T. Yokoi. *Xenobiotica* **2012**, 42, 854–62.

[15] J. H. Sung, J. H. Ji, K. S. Song, J. H. Lee, K. H. Choi, S. H. Lee, I. J. Yu. *Toxicology and Industrial Health* **2011**, 27, 149–154.

[16] X. F. Zhang, S. Gurunathan, J. H. Kim. *International Journal of nanomedicine* **2015**, 10, 6243–6256.

[17] P. L. Drake, K. J. Hazelwood. *Ann Occup Hyg* **2005**, 49, 575–585.

[18] H. Lodish, A. Berk, S. L. Zipurksky, P. Matsudaira, D. Baltimore, J. Darnell. (**2000**). Molecular Cell Biology. New York: W. H. Freeman.

[19] C. V. Kulkarni, A. M. Seddon, O. Cesa et al. *Soft Matter*, **2010**, 6, 4339–4341.

[20] G. Fischer, U. Kosinska-Eriksson, C. Aponte-Santamaria et al. *PLoS Biology* **2009**, 7.

[21] A. Mashaghi, S. Mashaghi, I. Reviakine, R. M. A. Heeren, V. Sondoghdor, M. Boon. *Chem. Soc. Rev.* **2014**, 43, 887–900.

[22] K. Kneipp, H. Kneipp, I. Itzkan, R. R. Dasari, M. S. Feld. *J. Phys.: Condens. Matter* **2002**, 14, R597–R624.

[23] J. H. Yoo, H. S. Han , C. Lee, K. P. Yoo, T. Kang. *J Nanosci Nanotechnol* **2013**, 13, 7239–44.

[24] J. R. Matthews, C. M. Payne, J. H. Hafner. *Langmuir* **2015**, 31, 9893–9900.

[25] C. Mangeney, V. Dupres, Y. Roche, N. Felidj, G. Levi, J. Aubard, S. Bernard. *Biopolymers* **2004**, 74, 136–40.

[26] J. Castillo−Leon, W. E. Svendsen, M. Dimaki (**2012**). Optical Manipulation Techniques. In K. Berg−Srensen. Micro and Nanotechniques for the Handling of Biological Samples. Boca Raton: CRC Press.

[27] J. W. Robinson, E. M. Skelly Frame, G. M. (**2014**). Undergraduate Instrumental Analysis. New York: CRC Press.

[28] J. R. Ferraro, K. Nakamoto (**1994**). Introductory Raman Spectroscopy. San Diego: Academic Press.

[29] E. V. Anslyn, D. A Dougherty (**2006**). Modern physical organic chemistry. Part I, Molecular Structure and Thermodynamics. California: University Science Books.

[30] P. Atkins, R. Friedman (**2005**). Molecular Quantum Mechanics. New York: Oxford University Press Inc.

[31] A. Ashkin. *Physical Review Letters***1970**, 24, 156–159.

[32] A. Ashkin, J.M. Dziedzic, J.E. Bjorkholm J E, S. Chu. *Optics letters* **1986**, 11, 288–290.

[33] S. C. Kuo. *Traffic* **2001**, 2, 757–763.

[34] J. Guck, R. Ananthakrishnan, T. J. Moon, C. C. Cunningham, J. Käs. *Phy Rev Lett.* **2000**, 84, 5451–5454.

[35] H. Schulz, M. Baranska. *Vibrational Spectroscopy* **2007**, 43, 13–25.

[36] C. V. Raman. *Indian J. Phys.* **1928**, 2, 387.

[37] Pasquale Maddaloni, Marco Bellini, Paolo De Natale (**2013**). Laser-Based Measurements for Time and Frequency Domain Applications: A Handbook. Boca Raton: Taylor & Francis.

[38] Toptica photonics.*http://www.toptica.com/products/research_grade_diode_lasers/tunable_diode_lasers/tunable_diode_lasers_370_nm_1770_nm_dl_100.html*. Acceded on the 1st July 2016.

[39] Horiba Scientific.*http://www.horiba.com/scientific/products/raman-spectroscopy/raman-academy/raman-faqs/*. Acceded on the 1st July 2016.

[40] B. Moomaw. Hamamatsu Photonic Systems, Division of Hamamatsu Corporation, Bridgewater. New Jersey *http://www.photonics.com/EDU/Handbook.aspx?AID=25141*. Acceded on the 1st July 2016.

[41] J. K. Wilmshurst, H. J. Bernstein. *Canadian Journal of Chemistry* **1957**, 35, 911–925.

[42] X. Huang, M. A. El Sayed. *Journal of Advance Research* **2010**, 1, 13–28.

[43] P. R. West, S. Ishii, G. V. Naik, N. K. Emani, V. M. Shalaev, A. Boltasseva. *Laser Photonics Rev.* **2010**, 4, 795–808.

[44] J. Martin, J. Proust, D. Gerard, J. Plain. *Opt Mater Express* **2013**, 3, 954–959.

[45] M. Moskovits. *J. Chern. Phys.* 1978, 69, 4159–4161.

[46] Z. B. Wang, B. S. Luk yanchuk, W. Guo, S. P. Edwardson, D. J. Whitehead, L. Li, Z. Liu, K. G. Watkins. *J. Chem. Phys.* **2008**, 128, 094705.

[47] K. Kneipp, M. Moskovits, H. Kneipp (**2006**). Surface Enhanced Raman Scattering. Physics and Applications. Topics in applied physics. Berlin: Springer.

[48] S. Siddhanta, C. Narayana. *Nanomater. and Nanotechnol.* **2012**, 2, 1–12.

[49] M. Moskovits, *Rev. Mod. Phys.* **1985**, 57, 783.

[50] B. Nikoobakht, J. Wang, Mo. A. El Sayed. *Chemical Physics Letters* **2002**, 366 , 17–23.

[51] K. Kneipp. *J. Phys. Chem. C* **2016** (DOI : 10.1021/*acs.jpcc*.6*b*03785).

[52] J. S. Kim, E. Kuk, K. N. Yu, J. H. Kim, S. J. Park, Y. H. Park, C. Y. Hwang, Y. K. Kim, Y. S. Lee, D. H. Jeong, M. H. Cho.*Nanomedicine: Nanotechnology, Biology, and Medicine* **2007**, 3, 95–101.

[53] J. Kneipp, H. Kneipp, B. Wittig, K. Kneipp. *Nanomed:Nanotechnol. Biol. Med.* **2010**, 6, 214–226.

[54] A. Majdalawieh, M. C. Kanan, O. El-Kadri, S. M. Kanan. *J. Nanosci. Nanotechnol.* **2014,** 14, 4757–4780.

[55] K. S. Lokesh, A. Shambhulinga, N. Manjunatha, M. Imadadulla, M. Hojamberdiev. *Dyes and Pigments* **2015**, 120, 155–160.

[56] J. N. Anker, W. P. Hall, O. Lyandres, N. C. Shah, J. Zhao, R. P. V. Duyne. *Nat Mater* **2008**, 7, 442–453.

[57] S. Iravani, H. Korbekandi, S. V. Mirmohammaoli, B. Zolfaghari. *Res Pharm Sci* **2014**, 9, 385–406.

[58] P. C. Lee, D. J. Meisel, *Phys. Chem.* **1982**, 86, 3391–3395.

[59] A. Avalos, A. I. Haza, D. Mateo, P. Morales. *Int Wound J.* **2016**, 13, 101–109.

[60] T. Dörfer, M. Schmitt, J. Popp. *J. Raman Spectrosc.* **2007**, 38, 1379–1382.

[61] B. Sharma, R. R. Frontiera, A. I. Henry, E. Ringe, R. P. V. Duyne. *Materialstoday* **2012**, 15, 16–25.

[62] M. Gomez, M. Lazzari. *Materials Today* **2014**, 17, 358–359.

[63] M Espina Palanco, K. Bo Mogensen, M. Gählke, Z. Heiner, J. Kneipp, K. Kneipp. *Beilstein J. Nanotechnology* **2016**, 7, 834–840.

[64] V. V. Makarov, A. J. Love, O. V. Sinitsyna, S. S. Makarova, I. V. Yaminsky, M. E. Taliansky, N. O. Kalinina. *Acta naturae* **2014**, 6, 35–44.

[65] K. D Arunachalam, S. K. Annamalai, S. Hari. *Int J Nanomedicine.* **2013**, 8, 1307–1315.

[66] K. M. Kumar, B. Mandal, H. A. K. Kumar, S. B. Maddineni. *Spectrochimica Acta Part A: Molecular and Biomolecular Spectroscopy* **2013**, 116, 539–545.

[67] V.K. Vidhu, D. Philip. *Micron* **2014**, 156, 54–62.

[68] K. D. Arunachalam, S. K. Annamalai. *Int J Nanomedicine.* **2013**,8, 2375–2384.

[69] M. Matteucci, M. Triches, G. Nava, A. Kristensen, M. A. Pollard, K. Berg−Sørensen and R. J. Taboryski. *Micromachines* **2015**, 6, 1971–1983.

[70] A . Mozumder, Y . Hatano (**2003**). Charged Particle and Photon Interactions with Matter Chemical, Physicochemical, and Biological Consequences with Applications. Boca raton: CRC Press.

[71] K. Venkateswarlu. *Proceedings of the Indian Academy of Sciences Section A* **1941**, 13, 64–67.

[72] M. Fleischman, P. J. Hendra, A. J. McQuillan. *Chemical Physics letters* **1974**, 26, 163–166.

[73] E. Le Ru and P. Etchegoin (**2008**). Principles of Surface-Enhanced Raman Spectroscopy. Amsterdam: Elsevier Science.

[74] A. Stalmashonak, G. Seifert, A. Abdolvand (**2013**). Ultra-short Pulsed Laser Engineered. Metal-glass nanocomposites. New York: Springer.

[75] J. A. Creighton, C. G. Blatchford, M. G. Albrecht. *Journal of the Chemical Society, Faraday Transactions 2: Molecular and Chemical Physics* **1979**, 75, 790–798.

[76] E. T. Castellana, P. S. Cremer. *Surface Science Reports* **2006**, 61, 429–444.

[77] K.B. Mogensen, M. Gählke, J. Kneipp, S. Kadkhodazadeh, J.B. Wagner, M. Espina Palanco, H. Kneipp and K. Kneipp. *Royal Society of Chemistry* **2014**, 50, 3744–3746.

[78] J. Hyllested, M. E. Palanco, N. Hagen, K. B. Mogensen, K. Katrin. *Beilstein J. Nanotechnol.* **2015**, 6, 293–299.

[79] L. Lin, S. Lu, J. M. Harnly. *J. Agri. Food Chem.* **2007**, 55, 1321–1326.

[80] A. Ebadollahi, J. J. Sendi, A. Aliakbar, J. Razmjou. *Psyche* **2014**, 1–6.

[81] B. Schrader, H. Schulz, M. Baranska, G. N. Andreev, C. Lehner, J. Sawatzki. *Spectrochimica Acta Part A* **2005**, 61, 1395–1401.

[82] B. P. Mateu, B. Stefke, M. T. Hauser, N. Gierlinger. *Spectrosc. Eur.* **2014**, 26, 11–14.

[83] M. Roman, R. Baranski, M. Baranska. *J. Agric. Food Chem.* **2011**, 59, 7647–7653.

[84] H. Schulz, B. Schrader, R. Quilitzsch, S. Pfeffer, H. Kruger. *J. Agric. Food Chem* **2003**, 51, 2475–2481.

[85] N. Gierlinger. *Front Plant Sci* **2014**, 5, 306.

[86] H. Schulz, A. Krähmer, A. Naumann and G. Gudi (**2014**). Infrared and Raman Spectroscopic Mapping and Imaging of Plant Materials. In R. Salzer and H. W. Siesler (Eds.), Infrared and Raman Spectroscopic Imaging: Wiley VCH Verlag GmbH & Co. KGaA.

[87] U. P. Agarwal *Front Plant Sci* **2014**, 5, 490,1–12.

[88] Daniel P. Killeen, J. W. van Klink, B. M. Smallfield, K. C. Gordon, N. B. Perry. *New Phytologist* **2015**, 205, 339–349.

[89] H. J. Butler, L. Ashton, B. Bird, G. Cinque, K. Curtis, K. Esmonde−white, N. J. Fullwood, B. Gardner, P. L. Martin, M. J. Walsh, M. R. Mcainsh, N. Stone, F. L. Martin, H. J. Butler and P. L. Martin-hirsch. *Nat. Protoc.*, **2016**, 11, 1–47.

[90] R. H. Atalla, U. P. Agarwal. *Science* **1985**, 227, 636–638.

[91] U. P. Agarwal, R. H. Atalla. *Planta* **1986**, 169, 325–332.

[92] M. M. L. Yu, H. G. Schulze, R. Jetter, M. W. Blades, R. F. B. Turner. *Applied Spectroscopy* **2007**, 61,32–37.

[93] J. A. H. Guerrero, J. J. Benitez, E. Dominguez, I. S. Bayer, R. Cingolani, A. Athanassiou, A. Heredia. *Front Plant Sci* **2014**, 5, 1–14.

[94] T. Vo-dinh, *Sensors Actuators B*, **1995**, 29, 183–189.

[95] S. Nie and S. R. Emory, *Science*, **1997**, 275, 1102–1106.

[96] K. Kneipp, Y. Wang, H. Kneipp, L. T. Perelman, I. Itzkan, R. R. Dasari, M. S. Feld, *Phys. Rev. Lett.* **1997**, 78, 1667–1670.

[97] P. Rösch, J. Popp and W. Kiefer, *J. Mol. Struct.*, **1999**, 480–481, 121–124.

[98] L. G. Thygesen, K. Jrgensen, B. L. Mller and S. B. Engelsen, *Appl. Spectrosc.*, **2004**, 58, 212–217.

[99] A. Shen, J. Guo, W. Xie, M. Sun, R. Richards, J. Hu, *J. Raman Spectrosc.*, **2011**, 42, 879–884.

[100] C. M. Muntean, N. Leopold, A. Halmagyi, S. Valimareanu, *J. Raman Spectrosc.*, **2011**, 42, 844–850.

[101] D. C. Rambaldi, F. Pozzi, N. Shibayama, M. Leona, F. D. Preusser, *J. Raman Spectrosc.*, **2015**, 46, 1073–1081.

[102] C. Zaffino, S. Bruni, B. Russo, R. Pilu, C. Lago, G. M. Colonna, *J. Raman Spectrosc.*, **2016**, 47, 269–276.

[103] M. Espina Palanco, K. B. Mogensen, K. Kneipp, *J. Raman Spectrosc.*, **2016**, 47, 156–161.

[104] C. M. Muntean, I. Bratu, N. Leopold, C. Morari, L. Buimaga-Iarinca, M. A. P. Purcaru, *Phys. Chem. Chem. Phys.*, **2015**, 17, 21323–21330.

[105] C. M. Muntean, N. Leopold, C. Tripon, A. Coste, A. Halmagyi, Spectrochim. *Acta Part A Mol. Biomol. Spectrosc.*, **2015**, 144, 107–114.

[106] R. Hou, S. Pang, L. He, *Anal. Methods*, **2015**, 7, 6325–6330.

[107] Z. Chen, L. Yongyu, P. Yankun, X. Tianfeng, *Int. J. Agric. Biol. Eng.* **2015**, 8, 113–120.

[108] J. Chen, Y. Huang, P. Kannan, L. Zhang, Z. Lin, J. Zhang, T. Chen, L. Guo, *Anal. Chem.* **2016**, 88, 2149–2155.

[109] S. Moghaddasi, S. K. Verma. *Int. J. Biol. Med.* **2011**, 2, 466–471.

[110] E. Dagne, D. Bisrat, A. Viljoen, B. E. Van Wyk. *Curr. Org Chem.* **2000**, 4, 1055–1078.

[111] Health Benefits of Basil Essential Oil. Unbiased info on nutrition, benefits of food home remedies. *https://www.organicfacts.net/health-benefits/basil-essential-oil.html*. Acceded on the 1st July 2016.

[112] S. Medda, A. Hajra, U. Dey, P. Bose and N. K. Mondal. *Appl. Nanosci.*, **2015**, 5, 875–880.

[113] S. Ibrahim, A. M. A. Fadhil and N. K. Al-Ani. *J. Al-Nahrain Univ. Sci.*, **2014**, 17, 165–171.

[114] L. Z. Lin, S. Lu, J. M. Harnly. *J. Agric. Food Chem.* **2007**, 55, 1321–1326.

[115] K. E. Heim, A. R. Tagliaferro, D. J. Bobilya. *Journal of Nutritional Biochemistry* **2002**, 13, 572–584.

[116] L. F. Maia, V. E. Oliveira, M. E. R. Oliveira, B. G. Fleury, L. F. C. Oliveira. *J. Raman Spectrosc.* **2012**, 43, 161–164.

[117] L. M. Maia, R. F. Fernandes, M. R. Almeida, L. F. C. Oliveira. *Revista Brasileira de Farmacognosia* **2015**, 25, 619–626.

[118] H. Silva, S. Sagardia, M. Ortiz, N. Franck, M. Opazo, M. Quiroz, C. Baginsky, C. Tapia. *Rev. Chil. Hist. Nat.* **2014**, 87, 13.

[119] H. Qian, X. Peng, X. Han, J. Ren, L. Sun, Z. Fu. *J. Environ. Sci.*, **2013**, 25, 1947–1955.

[120] D. Bao, Z. G. Oh, Z. Chen. *Front. Plant Sci.*, **2016**, 7, 1–8.

[121] R. V. M. Jovine, G. Johnsen, B. B. Prezelin. *Photosynthesis Research* **1995**, 44, 127–138.

[122] A. Michota, J. Bukowska. *J. Raman Spectroscopy* **2003**, 34, 21–25.

[123] J. Kneipp, H. Kneipp, B. Wittig, K. Kneipp. *Nano Lett.* **2007**, 7, 2819–2823.

[124] D. Grieshaber, R. MacKenzie, J. Vörös, E. Reimhult. *Sensors* **2008**, 8, 1400–1458.

[125] C. Hélix-Nielsen. **2012**. Biomimetic Membranes for Sensor and Separation Applications. New York: Springer.

[126] Y. R. Kim, S. Jung, H. Ryu, Y. E. Yoo, S. M. Kim, T. J. Jeon. *Sensors* **2012**, 12, 9530–9550.

[127] R. Molinaro, C. Corbo, J. O. Martinez, F. Taraballi, M. Evangelopoulos, S. Minardi, I. K. Yazdi, P. Zhao, E. De Rosa, M. B. Sherman, A. De Vita, N. E. Toledano Furman , X. Wang, A. Parodi, E. Tasciotti. *Nature Materials* **2016**, DOI: 10.1038.

[128] A. Lee, J. W. Elam, S. B. Darling. *Environ. Sci.: Water Res. Technol.*, **2016**, 2, 17–42.

[129] K. Oka, S. Hara. *J. American Chemical Society* **1977**, 99, 3859-3860.

[130] J. H. Lee, H. E. Jin, M. S. Desai, S. Ren, S. Kim, S. W. Lee. *Nanoscale* **2015**, 7, 18379–18391.

[131] A. Mateescu, Y. Wang, J. Dostalek, U. Jonas. *Membranes* **2012**, 2, 40–69.

[132] A. Mech-Dorosz, A. Heiskanen, S. Bäckström, M. Perry, H. B. Muhammad, C. Hélix-Nielsen, J. Emnéus. *Biomed Microdevices.* **2015** 17, 21.

[133] B. M. Discher, Y. Y. Won, D. S. Ege, J. C. Lee, F. S. Bates, D. E. Discher, D. Hammer. *Polymersomes: Tough Vesicles Made from Diblock Copolymers. Science* **1999**, 284, 1143–1146.

[134] Sol M. Gruner. *Proc. Nail. Acad. Sci.* **1985**, 82, 3665–3669.

[135] D. Marsh. *Biophysical Journal* **1996**, 70, 2248–2255.

[136] Z. Chen, R. P. Rand. *Biophys J.* **1998**, 74, 944–952.

[137] C. Nielsen, O. S. Andersen. *Biophysical Journal* 2000, 79, 2583–2604.

[138] H. T. McMahon, E. Boucrot. *J Cell Sci* **2015**, 128, 1065–1070.

[139] D. Koller, K. Lohner. *Biochimica et Biophysica Acta (BBA)-Biomembranes* **2014**, 1838, 2250–2259.

[140] P. R. Cullis, B. De Kruijff. *Biochimica et Biophysica Acta* **1979**, 559, 399–420.

[141] S. Raffy, J. Teissie. *Biophys J.* **1999**, 76, 2072–2080.

[142] H. Ohvo-Rekila, B. Ramstedt, P. Leppimaki, J. P. Slotte. *Prog Lipid Res.* **2002**, 41, 66–97.

[143] O. S. Andersen, C. Nielsen, A. M. Maer, J. A. Lundbaek, M. Goulian, R. E. koeppe. *Methods Enzymol* **1999**, 294, 208–224.

[144] M. F. Brown. *Chemistry and Physics of Lipids* **1994**, 73, 159–180.

[145] L. Iversen, S. Mathiasen, J. B. Larsen, D. Stamou. *Nature Chemical Biology* **2015**, 11, 822–825.

[146] J. A. Lundbaek, S. A. Collingwood, H. I. Ingolfsson, R. Kapoor, O. S. Andersen. *J. R. Soc. Interface* **2010**, 7, 373–395

[147] R. M. Epand , K. Souza,B. Berno, M. Schlame. *Biochimica et Biophysica Acta* **2015**, 1848, 220–228.

[148] N. Mobashery, C. Nielsen, O. S. Andersen. *FEBS Lett.* **1997**, 412, 15–20.

[149] D. J. Stevenson, F. G. Moore, K. Dholakia. *J. Biomed. Opt.* **2010**, 15, 0415031–04150321.

[150] A. Ashkin, J. M. Dziedzic, T. Yamane. *Nature* **1987**, 330, 769–771.

[151] J. R. Moffitt, Y. R. Chemla, S. B. Smith, C. Bustamante. *Annu. Rev. Biochem.* **2008**, 77, 205–28.

[152] C. Bustamante, Z. Bryant, S. B. Smith. *Nature* **2003**, 421, 423–427.

[153] D. B Ritchie, M. T Woodside. *Current Opinion in Structural Biology* **2015**, 34, 43–51.

[154] J. O. L. Andresson, S. Shastry, W. O. Hancock, S. M. *Curr Biol.* **2015**, 25, 1166–1175,

[155] Y. Liu, D. K. Cheng, G. J. Sonek, M. W. Berns, C. F. Chapman, B. J. Tromberg. *Biophys J.* **1995**, 68, 2137–2144.

[156] S. C. Kuo. *Methods Cell Biol.* **1998**, 55, 43–45.

[157] A. E. Ekpenyong, G. Whyte, K. Chalut, S. Pagliara, F. Lautenschläger, C. Fiddler, S. Paschke, U. F. Keyser, E. R. Chilvers, J. Guck. *PLoS ONE* **2012**, 7(9): e45237.

[158] M. E. Solmaz, S. Sankhagowit, R. Biswas, C. A. Mejia, M. L. Povinelli, N. Malmstadt. *RSC adv.* **2013**, 3, 16632–16638.

[159] M. E. Solmaz, R. Biswas, S. Sankhagowit, J. R. Thompson, C. A. Mejia, N. Malmastadt, M. L. Povinelli. *Biomedical Optics express* **2012**, 3, 2419–2427.

[160] U. Delabre, K. Feld, E. Crespo, G. Whyte, C. Sykes, U. Seifer, J. Guck. *Soft Matter* **2015**, 11, 6075–6088.

[161] L. Tskhovrebova, J. Trinick, J. Sleep, R. M. Simmons. *Nature* **1997**, 387, 308–312.

[162] T. W. Remmerbach, F. Wottawah, J. Dietrich, B. Lincoln, C. Wittekind, J. Guck. *Cancer Res.* **2009**, 69, 1728–1732.

[163] M. Pradhan, S. Pathak, D. Mathur, U. Ladiwala. *Biomedical Optics Express* **2016**, 7, 943–948.

[164] T. Yang, F. Bragheri, P. Minzioni. *Micromachines* **2016**, 7, 90.

[165] E. Eriksson, J. Scrimgeour, A. Graneli, K. Ramser, R. Wellander, J. Enger, D. Hanstorp, M. Goksör. *J. Opt. A: Pure Appl. Opt.* **2007**, 9, S113–S121.

[166] B. Lincoln, S. Schinkinger, K. Travis, F. Wottawah, S. Ebert, F. Sauer, J. Guck. *Biomed Microdevices* **2007**, 9, 703–710.

[167] C. Faigle, F. Lautenschlager, G. Whyte, P. Homewood, E. Martin Badosa, J. Guck. *Lab Chip*, **2015**, 15, 1267–1275.

[168] N. Bellini, K. C. Vishnubhatla, F. Bragheri, L. Ferrara, P. Minzioni, R. Ramponi, I. Cristiani, R. Osellame. *OPTICS EXPRESS* **2010**, 18, 4679–4688.

[169] N. Bellini, F. Bragheri, I. Cristiani, J. Guck, R. Osellame, G. Whyte. *Biomedical Optics Express* **2012**, 3, 2658–2668.

Appendices

.1 Appendix A: standard chemical procedure for synthesizing of silver nanoparticles.

- **Protocol 1: synthesis of silver nanoparticles.**

  1. Fill 500 ml shake flasks with 45 mg of NaCl in 245 ml of deionized H_2O and cover the sample to keep it in darkness.

  2. Boil it up to 95 Celsius degrees while stirring with a magnetic bar at 400 rpm.

  3. Add 5 ml of 50 mg sodium citrate aqueous solution and keep stirring the sample until it reaches 95 Celsius degree.

  4. Switch off the heater and leave the solution cold down, keep stirring for 1 hour.

.2 Appendix B: preparation of blood cells for optical trapping.

- **Protocol 2: blood cells**

  1. Fill 1.5ml Micro Plastic Test Tube Centrifuge Vial Snap Cap Container with 200 μl of blood cell solution procured from the hospital.

  2. Add 800μl of physiological salt water (NaCl 9mg/mL).

  3. Samples are ready for Optical manipulation measurements.

.3 Appendix C: preparation of yeast cells for optical trapping.

Spheroplast from Yeast cells were prepared by following a protocol procured by Karen Lindkvist, department of Experimental Medical Sciences, Lund University, Sweden.

- **Protocol 3: express yeast Aquaporin Aqy1 in Pichia pastoris and prepare protoplasts**. At least three days before starting cell culture:

  1. Re$-$streak cells from $-80°C$ freezer on fresh YPD$-$agar plate from glycerol stock.

2. Incubate at 30°C for three days.

3. Keep the plate at 4°C up to one month.

- Day 1:

1. Inoculate colonies from the YPD-agar plate into 25 ml of BMGY in a 250 ml culturing flasks.

2. Incubate at 30řC, 225 RPM over night.

- Day 2:

1. Measure $OD600$ of the pre−cultures. Blank spectrophotometer with BMGY. If OD is higher than 1, dilute with BMGY.

2. Calculate the volume of cell cultures needed to get OD 1 in 50 ml BMMY.

3. Transfer these volume to 15 ml Falcon tubes and centrifuge at 3000 x g, 5 min, RT and pour off supernatant (media containing glycerol).

4. Wash the cells in BMMY: resuspend cells in 25 ml BMMY, centrifuge at 3000 x g, 5 min, RT, pour off supernatant.

5. Resuspend cells in 50 ml BMMY and transfer to 500 ml culturing flasks.

6. Measure $OD600$ of to confirm right OD

7. Incubate at 30°C, 225 RPM, $16 - 22$ h

8. Add 0.25 ml of 100% methanol (0.5 % of total volume) after 6−7 hours of incubation to ensure that the cells are not starving.

- Day 3:

1. Measure $OD600$ of the 50 ml cultures.

2. Harvest cells by centrifugation at 3000 x g, 5 min, RT.

3. Wash the cells in 10 ml TE−buffer (3000 x g, 5 min, RT).

4. Weigh the cells.

5. Incubate with 5 ml TE−buffer and 0.5% mercaptoethanol for 1.5 h to destabilize the cell wall at 30řC, 120 rpm.

6. Check the cells in microscope.

7. Harvest protoplasts at 3000 x g, 5 min, RT.

8. Wash protoplasts three times with 1.2 M Sorbitol and 20 mM MES (pH 6.5) (3000 x g, 5 min, RT).

9. Resuspend cells in 1.2 M Sorbitol and 20 mM MES (pH 6.5) to final OD of 5.

BMGY (Buffered Glycerol-complex Medium) or BMMY (Buffered Methanol-complex Medium):
1 % yeast extract
2 % peptone
100 mM potassium phosphate, pH 6.0
1.34 % YNB
$4x10_{-5}$% biotin
1 % glycerol or 0.5% methanol

BMXY (media base) (1 % yeast extract, 2 % peptone):
2 g yeast extract
4 g peptone
Adjust volume to 140 ml with mH_2O.
Sterilize in autoclave, store at RT.
NB: Concentrations based on a final volume of 200 ml.

10x (1 M) Potassium phosphate, pH 6.0**:**
11.8 g of KH_2PO_4
2.3 g of K_2HPO_4
Dissolve in 70 ml mH_2O, adjust pH to 6.0 with KOH pellets.

Adjust volume to 100 ml with mH_2O.
Sterilize by filtration (0.2μm), store at RT

10x **YNB (Yeast Nitrogen Base w/ ammonium sulfate w/o amino acids):**
10 g ammonium sulfate $(NH_4)_2SO_4$
3.4 g YNB w/o ammonium sulfate and amino acids
Adjust volume to 100 ml with mH_2O
Sterilize by filtration (0.2μm), store at 4řC

500x(0.02%) **Biotin:**
3 mg biotin
Adjust volume to 15 ml with mH_2O
Sterilize by filtration (0.2μm filter), store at 4řC

10x(10%) **Glycerol:**
11.8 ml 85 % glycerol
Adjust volume to 100 ml with mH_2O
Sterilize by filtration (0.2μm), store at RT.

10x(5%) **Methanol:**
5 ml 100% methanol
Adjust volume to 100 ml with mH_2O
Sterilize solution by filtration (0.2μm filter), store at RT.

TE-buffer:
100 mM Tris, pH 8.0
1 mM EDTA

Sorbitol buffer:
1.2 M sorbitol
20 mM MES, pH 6.5

.4 Appendix D: thermal bonding of the microfluidic-chip

- Remove around 15 cm length of the outer coating of two optical fibers with a scalpel.

- Peel, cleave and clean both ends of the optical fibers with ethanol.

- Place lid A on a petridish of diameter around 20 cm, and place it under the microscope. Use a strong tape (transparent tape) to fix the chip to the glass.

- Mount both ends of the optical fibers into the fibers groove in lid A (Figure 2.8, Chapter 2). The tips of the optical fibers must be touching each other to start with.

- Use blue tape on the top of the fiber grooves to make sure that the optical fibers do not move. Use semi-transparent tape to fix the optical fibers to the glass. DO NOT use semi-transparent tape on the top of the chip.

- Add two small drops (as small as possible) of epoxy glue on the top of the fiber grooves, at around 1.5 cm from where the tips of the fibers are touching. Use a needle for adding the glue. Let it dry for at least 30 min. Make sure that the glue is dry before step 9.

- Introduce lid B in the UV-wave for 3 minutes.

- Place lid B in a multiple holder. It is convenient to place it in the middle of the holder.

- Remove all tapes from lid A very carefully. After removing the tapes, the sides of the fibers will probably move. That is not a problem if the ends of the fibers are still touching. Check under the microscope that the fibers did not move.

- Flip lid A and place it on the top of lid B (do not move lid B from the multiple holder), matching the inlet and outlet ports and making sure that the fibers are in the grooves.

- Place a transparent polymer slide on the top of the chip to avoid damages of the chip during the thermal bonding. Polymer slides are available next to the pressure-bonding machine.

- Take the multiple holder (which contains the chip with the polymer slide), and place it on the plates of the bonding machine while it is still cold. Lower the plate of the bonding machine until it is lightly touching the chip.

- Set parameters in the bonding-pressure machine: temperature 125 degrees Celsius, force 1 kN.

- Apply force up to 1 kN with the lever.

- Switch on the temperature.

- During the next 10 minutes the force that the plates are applying to the chip will increase until the plates reach 125 degrees Celsius. Make sure to adjust the force up to maximum 1 kN. Once the plates reach 125 degrees Celsius, keep the chip in the bonding machine for another 10 minutes.

- The chip should be bonded now. Release the pressure with the lever and separate the plates from the chip.

- Check the chip under the microscope.